Theoretical Study on the Excited States of Peralkylated Oligosilanes and the Resonance States of DNA and RNA Bases

January 2020

Yuki Kanazawa

The Graduate University for Advanced Studies, SOKENDAI

School of Physical Sciences

Department of Structural Molecular Science

Table of Contents

Chapter 1.

General Introduction

Electronic and geometric structures of molecules are relevant for their functions or photophysical properties. For example, thermochromism of linear peralkylated polysilanes is originated in the delocalization of σ-electrons and indirect radiation damage to DNA or RNA is caused by the resonance states generated by the low-energy electron attachment. Exploring the intrinsic origins of these electronic phenomena is valuable to develop fundamental physical chemistry or biological chemistry. However, to reveal these electronic states, we need to describe complex electronic states; that is, electronic excited or resonance states, using accurate electronic structure theories. While various experimental methodologies have been developed to measure the detailed electronic structures, theoretical studies which provide accurate understanding and interpretation are indispensable. In this thesis, the author has worked on two subjects regarding complex electronic structures; that is σ-delocalization of peralkylated oligosilanes and electronic resonance states of DNA/RNA bases.

In chapter 2, the author studied the electronic transitions in conformationally controlled peralkylated hexaslianes. Electronic properties of σ-electron delocalization have received much attention in the context of understanding the electronic properties. Polysilane, which has silicon single bond in main chain and mainly has organic group in side chain, shows unique photophysical properties due to σ-electron delocalization for its conformational dependence. The σ-electrons that comprise silicon single bonds behave like carbon double bonds of its π-electrons, because Si atom belongs to 14th group and 3rd period in the periodic table, and it shows electron positivity and ambiguous restriction. Around the silicon principal chain, silicon σ-electron is delocalized. The σ-delocalized systems generally show high conformational flexibility, so that they can in principle be used to control their various optical properties by molecular design. In a previous study, *n*-tetrasilanes, the shortest oligosilanes which have stereoisomers, were studied. The most favorable conformation represented in SiSiSiSi dihedral angles, ω, was found to be 165°(transoid). To clarify the characteristic photophysical and electronic properties of polysilanes and oligosilanes, representative models of σ-delocalized systems with a singly bonded chain carrying lateral substituents, have been extensively studied by UV absorption, luminescence, non-linear polarizability, and photoconductivity and so on. In this work, the author studied the σ-electron delocalization of peralkylated hexasilanes chain whose dihedral angles show *syn*, *anti*, or *eclipsed* conformation. The collaborator investigated these conformations by using UV absorption, magnetic circular dichroism (MCD), and liner dichroism (LD) spectroscopy, and simulated by consistent deconvolution with Gaussian for comparing their wavenumbers $\tilde{\nu}$, oscillator strengths f, and MCD B terms in all three compounds.

The author adopted the symmetry-adapted-cluster configuration interaction (SAC-CI) method and time-dependent density functional theory (TD-DFT) with the PBE0 functional in the theoretical analysis and provided the semi-quantitative assignments and interpretations.

In chapter 3, the author studied the excited states of the peralkylated oligosilanes. n-Peralkylated oligosilanes show unique emission spectra depending on the Si chain length. In the case the Si chain length is short (n=4–6), the emission occurs in low energy region where Stokes shift is very large and the emission peak is broad. On the other hand, in the case of longer Si chain (n≥7), the Stokes shift is small. This feature should be related to the structure relaxation in the excited state. In this regard, the relationship between the excited-state structure relaxation and the Si chain length is of interest. In this work, the author investigated the excited state geometries of peralkylated oligosilanes $Me_3(SiMe_2)_nMe_3$ (n=4-8) by using DFT and TD-DFT calculations and tried to clarifies the origin of the changes in Stokes shift with respect to the Si chain length.

In chapter 4, the author investigated the low-lying π^* resonance states of DNA and RNA bases using the recently developed projected complex absorbing potential (CAP)/symmetry-adapted cluster-configuration interaction (SAC-CI) method. If low energy (<3eV) electron which is released from radiated matter attaches to DNA, its nucleobases temporarily become metastable anion as the electronic resonance state, and decompose. Since DNA and RNA play a crucial role in various biological processes, this process provides damages to biological systems. Although direct damage, in which energy deposition and subsequent reactions occur directly in DNA, has been observed in ultrafast electron transfer experiments in DNA, in low-energy electron-induced processes, also referred to as the resonance states, are initial key intermediates in the damage of DNA strands. Low energy electron attachment causes the indirect radiation damage via the vacant π^* molecular orbitals (MOs) of DNA bases. From ionizing radiation, damage to nucleic acids can be generated through a mechanism involving low-energy electron attachment to the nucleic acid and subsequent bond breaking due to energy transfer to a vibrational mode of the temporary anion formed in the electron-capture step. In this work, the author studied the resonance states of DNA and RNA bases by the CAP/SAC-CI method using a smooth Voronoi potential as CAP. In spite of the challenging CAP applications to higher resonance states of molecules of this size, the present calculations reproduced resonance positions observed by electron transmission spectra (ETS) provided that the anticipated deviations due to vibronic

effects and limited basis sets are taken into account. Moreover, for the standard nucleobases, the calculated positions and widths qualitatively agree with those obtained in previous electron scattering calculations. For guanine, both keto and enol forms were examined, and the calculated values of the keto form agree clearly better with the experimental findings. In addition to these standard bases, three modified forms of cytosine, which serve as epigenetic or biomarkers, were investigated: formylcytosine, methylcytosine, and chlorocytosine. Last, a strong correlation between the computed positions and the observed ETS values is demonstrated, clearly suggesting that the present computational protocol should be useful for predicting the π^* resonances of congeners of DNA and RNA bases.

In chapter 5, the author studied the electronic resonance states of the molecules with cyano or isocyano groups. Cyano and isocyano groups have an electron-withdrawing character and stabilize the electron-attached states when molecules have these substituents. Indeed, these molecules have low-lying π^* resonance states. Also when the molecules have two or more cyano or isocyano groups, the electronic resonance states interact to each other and generate new resonance states. The author also systematically performed the benchmark calculations with respect to the accuracy depending on the energy threshold in the perturbation selection of operators, variation/non-variational approaches of SAC-CI, and basis sets etc. The new physical insights were obtained for the interaction between the resonance states. In particular, the through-bond interactions via in-plane and out-of-plane orbital orbitals were analyzed with the splitting of the calculated energy levels.

In chapter 6, the author summarized the present theoretical works with respect to two research subjects in this thesis; namely, the electronic states and geometries of peralkylated oligosilanes as well as their unique photopysical properties and the electronic resonance states of DNA and RNA nucleobases.

Chapter 2.

Electronic Transitions in Conformationally Controlled Peralkylated Hexasilanes

Photophysical properties of oligosilanes show unique conformational dependence due to σ-electron delocalization. Experimental group investigated the excited states of *SAS*, *AAS*, and *AEA* conformations of peralkylated *n*-hexasilanes, in which SiSiSiSi dihedral angles are controlled into either *syn* (*S*), *anti* (*A*), or *eclipsed* (*E*) conformation by using UV absorption, magnetic circular dichroism (MCD), and linear dichroism (LD) spectroscopy. Simultaneous Gaussian fit of all three spectra identifies a minimal set of transitions and their wavenumbers $\tilde{v}$, oscillator strengths *f*, and MCD *B* terms in all three compounds. The author investigated the excited states of these molecules using the symmetry-adapted-cluster configuration interaction (SAC-CI) method and time-dependent density functional theory (TD-DFT) with the PBE0 functional. The theoretical results agreed well with the experimental observations and provided the quantitative assignments. The conformational dependence of transition energies and other properties of free-chain permethylated *n*-hexasilane $n\text{-Si}_6\text{Me}_{14}$ is also examined as a function of dihedral angles and the striking effects found are attributed to avoided crossings between configurations of σσ* and σπ* character.

Keywords: peralkylated *n*-hexasilane; UV, MCD, LD spectra; SAC-CI; TD-DFT

2.1. Introduction

Photophysical properties that reflect the delocalization of σ electrons, more complicated and less well understood than delocalization of π electrons, have received much attention in the context of understanding the electronic properties of catenates of heavier main group elements, such as silicon and phosphorus. σ-Delocalized systems generally show high conformational flexibility, and this could in principle be used to control their various optical properties by molecular design. However, this feature has not been fully understood or utilized so far.

The characteristic photophysical and electronic properties of polysilanes and oligosilanes, representative models of σ-delocalized systems with a singly bonded chain carrying lateral substituents, have been extensively studied (e.g., UV absorption,[1-9] luminescence,[5-8,10] non-linear polarizability,[11,12] and photoconductivity[13]) and reviewed.[14-21] A complete understanding of σ-delocalization in simple terms is still far away, due to its strong conformational dependence, exemplified by the thermochromism [22-26] of oligosilanes.[27] Flexible unconstrained permethylated polysilane chains favor three SiSiSiSi dihedral angles, *transoid* (165°), *gauche* (55°), and *ortho* (90°).[21,28-30] Among these conformations, the thermodynamically most stable transoid form predominates at low temperatures[31] and typically shows an intense long-wavelength absorption band.[32,33]

Extensive efforts have been made to clarify the conformational effects on oligosilane photophysical properties for various Si-Si chain lengths. The theoretical understanding of *n*-tetrasilanes, the shortest chains that exhibit conformational isomerism, is now well advanced. Computational studies have been published for the ladder C and H models,[33-37] conformational analysis,[28,29,38-42] and excited states of the *n*-tetrasilanes Si_4H_{10}[43-45] and *n*-Si_4Me_{10},[9,34,46-48] and for longer chains.[33] Experimental studies dealt with matrix isolation of *n*-Si_4Me_{10} conformers,[46,49] conformational control by cyclic carbosilanes,[6,8,49-52] bicyclic disilanes,[32,52-56] bicyclic trisilanes,[57,58] and bulky lateral substituents,[59] hypervalent silicons,[60-63] helicity introduction by chiral terminal[64-66] or lateral[67,68] substituents, and inclusion into cyclodextrin and other hosts.[69-74]

Joint theoretical and experimental studies of model tetrasilanes of C_2 symmetry have assigned their excited states to either A or B irreducible representation. Transitions from the ground to A states are usually weak, while transitions to at least the lowest and sometimes several B states are often strong. At highly twisted conformations (cisoid, small SiSiSiSi dihedral angle) the first transition is to a state with mostly σπ* character and the lowest σσ* transition is much higher. At dihedral angles approaching 180º (anti), the strong σσ* transition

6

lies below the weak first σπ* transition, and this results in an avoided crossing at intermediate dihedral angles. At all dihedral angles, the lowest σσ* component endows a transition with a significant oscillator strength, whereas the σπ* components hardly contributes to the intensity at all. These general trends were observed both in the UV, MCD (magnetic circular dichroism), and LD (linear dichroism) spectra and in the calculated properties of conformationally controlled peralkylated tetrasilanes.[9,35]

Presently, the collaborators of the author turn to Si backbone conformational effects in longer Si chains, which have only been studied in detail theoretically for some model systems[33] and experimentally in the case of peralkylated *n*-hexasilanes.[10,21,53,59] So far, conformationally controlled *n*-hexasilanes with lateral bulky substituents shown in Scheme 1 where three SiSiSiSi dihedral angles are present have been synthesized and their UV spectra have been reported in short communications.[21,53] However, a detailed analysis of these spectra has not been carried out. In particular, the longer chain should reveal richer effects of σ delocalization on electronic excitation, since the combination of three variable dihedral angles may provide many opportunities to affect σ delocalization in different ways.
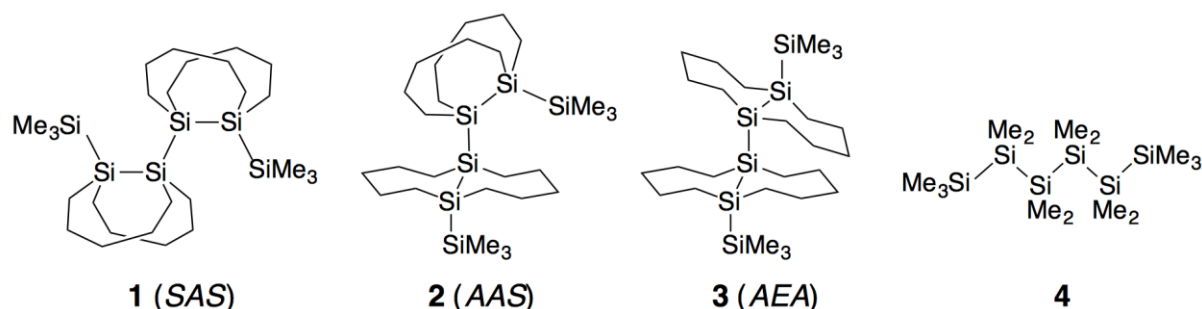
Scheme 1. Structures of conformationally controlled peralkylated *n*-hexasilanes **1-3** and the free permethylated *n*-hexasilane **4**.

The collaborators of the author worked on the UV, MCD, and LD$_r$ (reduced linear dichroism) spectra of the conformationally controlled peralkylated hexasilanes **1-3** (Scheme 1). These three compounds contain *syn* (*S*), *anti* (*A*), and *eclipsed* (*E*) SiSiSiSi dihedral angles and shall be referred to as *SAS*, *AAS* and *AEA* conformations. As is common for saturated chains, the spectra consist of broad fairly featureless bands, making the recognition of individual electronic transitions difficult. However, the collaborators of the author find that simultaneous Gaussian fitting of the three types of spectra is very helpful and permits a detailed analysis.

The author interpreted the observed transitions in terms of calculations using the symmetry-adapted configuration interaction (SAC-CI) method[75,76] and time-dependent

density functional theory (TD-DFT) with PBE0 functional.[77] The spectral changes in free-chain permethylated hexasilane n-Si$_6$Me$_{14}$ (**4**) are also computed as a function of backbone dihedral angles. The results represent the first detailed theoretical interpretation of the excited states of hexasilanes as a function of dihedral angles.

2.2. Calculations and Information of Experimental Spectra

The experimental measurement of the hexasilanes studied here was performed by the collaborators of the author. Here, only the information of experimental measurement which is important for the theoretical analysis and discussion is described. All the other information is referred to the original articles.[53,78,79]

Materials. All hexasilanes were prepared by methods described previously[53] and were purified thoroughly by recrystallization. 3-Methylpentane was purified by passing through a column of silver nitrate on alumina.[78]

(a) UV Absorption. UV absorption spectra were measured at room temperature and 77K. *D* terms were calculated according to the following equation in units of D^2, where D stands for Debye.[79]

$$D_i = 9.188 \times 10^{-3} \int_i d\tilde{v} \varepsilon / \tilde{v} \tag{1}$$

and oscillator strengths *f* were calculated from

$$f_i = 4.319 \times 10^{-9} \int_i \varepsilon(\tilde{v}) d\tilde{v} . \tag{2}$$

(b) Magnetic Circular Dichroism Spectra. MCD *B* terms were calculated in units of D$^2\beta_e$/cm^{-1} according to the following equation, where β_e stands for the Bohr magneton. Since the molecular symmetry is low and excludes state degeneracies, *A* and *C* terms are zero for all hexasilanes used.

$$B_i + C_i / kT = -33.53^{-1} \int_i d\tilde{v} [\Theta]_M / \tilde{v} \tag{3}$$

(c) Linear Dichroism Spectra.[81] To obtain the shape of reduced linear dichroism, $LD_r = \Delta OD/OD$ (on an indeterminate vertical scale) the isotropic optical density OD was approximated by OD measured at an arbitrary concentration in 3-MP. The LD_r values at the onset of absorption are distorted by the small difference between the OD measured in 3-MP and in polyethylene and were ignored.

(d) Simultaneous Fitting of Room-Temperature Absorption, MCD, and LD$_r$ Spectra. The

8

fitting to a set of Gaussian shaped peaks to obtain $\tilde{v}$, B, D, and f values was performed using the Origin program. This fitting was performed by the collaborator of the author (Dr. D.L. Casher). The results are given in Table 2.1 and displayed in Figures 2.S1 – 2.S3. The position (wavenumber $\tilde{v}$), height, and width (FWHM) of each Gaussian were adjustable parameters. The starting point for the fitting were preliminary values obtained by guessing the start and the end of the bands due to individual transitions from spectral shapes. The number of Gaussians used was the minimum needed for a visually satisfactory fit to all three types of spectra (Figures 2.S1 – 2.S3). Although it can be only approximately correct, it was assumed that band positions $\tilde{v}$ and widths FWHM were the same in UV absorption, MCD, and LD. It was further assumed that each absorption band i is purely polarized along some unknown direction in the molecular frame, whose average orientation in the polyethylene film is characterized by an average value $<\cos^2 \theta_i> = K_i$, where θ_i is the angle between the transition moment and the uniaxial stretching direction Z. Each band would therefore in itself have a constant LD_r value given by $G_i = (3K_i - 1)/2$ (shown on an arbitrary vertical scale by horizontal double lines in Figures 2.S1b – 2.S3b). The observed LD_r curve is a superposition of contributions from all bands, given by

$$LD_r = \left[\sum_i A_i (3K_i - 1) \right] \Big/ 2 \sum_i A_i \tag{4}$$

where A_i is the absorbance due to the i-th transition.

The bands associated with individual transitions are not necessarily Gaussian-shaped, and more than one Gaussian could correspond to a single transition in the fit. It was assumed that in such a case the ratios of the relative heights and the ratios of the relative widths within the set of Gaussians would be roughly similar in UV absorption and MCD spectra (similar spectral shapes), and the G_i values associated with the Gaussians would be similar as well (the same polarization).

(e) Fitting of Low-Temperature Absorption Spectra. Guided by the results of the simultaneous fitting of three room-temperature spectra, The collaborator of the author (Dr. D.L. Casher) finally also fitted the somewhat better resolved UV absorption spectra taken at 77 K and the results are shown in Figure 2.S4.
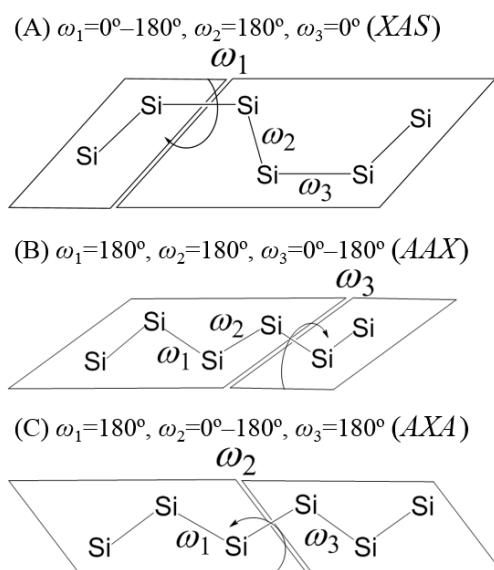
Computational Details

The author examined the conformational effects of linear hexasilane backbone chain on the absorption energy for peralkylated n-hexasilanes **1-3** and permethylated n-hexasilane **4**,

n-Si$_6$Me$_{14}$ (Scheme 1). Ground-state geometry optimizations were performed by the B3LYP[82]/6-311G(d)[83] method. Initial geometries for optimization were taken from X-ray crystal structures published previously (Figure 2.S5).[53] The X-ray crystal structure of **1** contains two distinct conformations with terminal dihedral angles ω = 13 and 30°. For **3**, the positions of carbon atoms are unclear and geometry optimization resulted in four different stable conformations. Thus, two C$_i$ conformations were obtained for **1** (*SAS*), one C$_1$ configuration for **2** (*AAS*), and two C$_i$ and two C$_1$ configurations for **3** (*AEA*). All the coordinates were optimized without constraints and the structures were confirmed to be local minima by vibrational analysis. In **4**, two dihedral angles were fixed in *syn* ($\omega = 0°$) or *anti* ($\omega = 180°$) conformation and one dihedral angle was varied from 0 to 180° in steps of 30° as shown in Scheme 2: (A) *XAS* ($\omega_1 = 0°–180°$, $\omega_2 = 180°$, $\omega_3 = 0°$), (B) *AAX* ($\omega_1 = 180°$, $\omega_2 = 180°$, $\omega_3 = 0°–180°$), and (C) *AXA* ($\omega_1 = 180°$, $\omega_2 = 0°–180°$, $\omega_3 = 180°$). All other coordinates were optimized.

Electronic transitions in **1-3** were obtained from SAC-CI and TD-PBE0 calculations. These calculations were done for all the above-mentioned conformations of the local minima. It has been well recognized that TD-PBE0 provides satisfactory results for valence excited states of π-conjugated system.[84-87] Therefore, in this work, TD-PBE0 was adopted for the excited states of the σ-delocalized systems **1-4**, using the 6-311G(d) basis set. SAC-CI calculations[88,89] were performed for vertical transitions of peralkylated n-hexasilanes **1-3**. The perturbation selection of linear operators was employed with LevelThree accuracy; the energy thresholds are $\lambda_g = 1\times10^{-6}$ and $\lambda_e = 1\times10^{-7}$.[90] The direct algorithm,[91] computing all nonlinear terms, was adopted. The basis sets were McLean and Chandler valence triple zeta [6s5p][92] with double polarization functions ($\zeta_d = 0.424$, 0.118)[93] for Si atoms and Huzinaga-Dunning D95v [3s2p/2s][93] for C and H atoms. The SAC-CI dimensions were 600,000 – 800,000 after the perturbation selection. Recently, benchmark SAC-CI and TD-PBE0 calculations were carried out, not only for energy,[86,87,94] but also charge transfer properties.[95,96] All calculations were performed with the developmental version of the Gaussian09 suite of programs[97] that includes a parallelized code for SAC-CI.

The σ and π character of the frontier MOs of compounds **1-3** relevant to the electronic transitions were determined from natural hybrid orbitals (NHOs) using a previously described method,[33] slightly modified to treat the terminal Si atoms in the same fashion as the internal ones. The sets of orthogonal NHOs were calculated using the Gaussian NBO version 3.1.[98]

(A) $\omega_1=0°–180°$, $\omega_2=180°$, $\omega_3=0°$ (XAS)

(B) $\omega_1=180°$, $\omega_2=180°$, $\omega_3=0°–180°$ (AAX)

(C) $\omega_1=180°$, $\omega_2=0°–180°$, $\omega_3=180°$ (AXA)

Scheme 2. Conformational changes examined for $n\text{-}Si_6Me_{14}$.

2.3. Results

UV, MCD, LD, and LD$_r$ Spectra of Conformationally Controlled Peralkylated n-Hexasilanes 1-3

UV absorption, MCD, LD, and LD$_r$ spectra of conformationally controlled peralkylated n-hexasilanes **1-3** are displayed in Figure 2.1. For hexasilane **1** (*SAS*, red line), the overall Gaussian fits and the individual Gaussian contributions are also shown (for full detail, see Figures 2.S1 – 2.S4). The numerical data for transition wave numbers $\tilde{v}$, oscillator strengths f, and MCD B terms that resulted from the simultaneous fitting of UV, MCD, and LD$_r$ spectra with five (**1** and **2**) or six (**3**) Gaussian functions are compiled in Table 2.1 along with the theoretical results for the *SAS*-2, *AAS*, and *AEA*-3 conformations; results for the other conformations are provided in the Supporting Information (Tables 2.S5 – 2.S8).
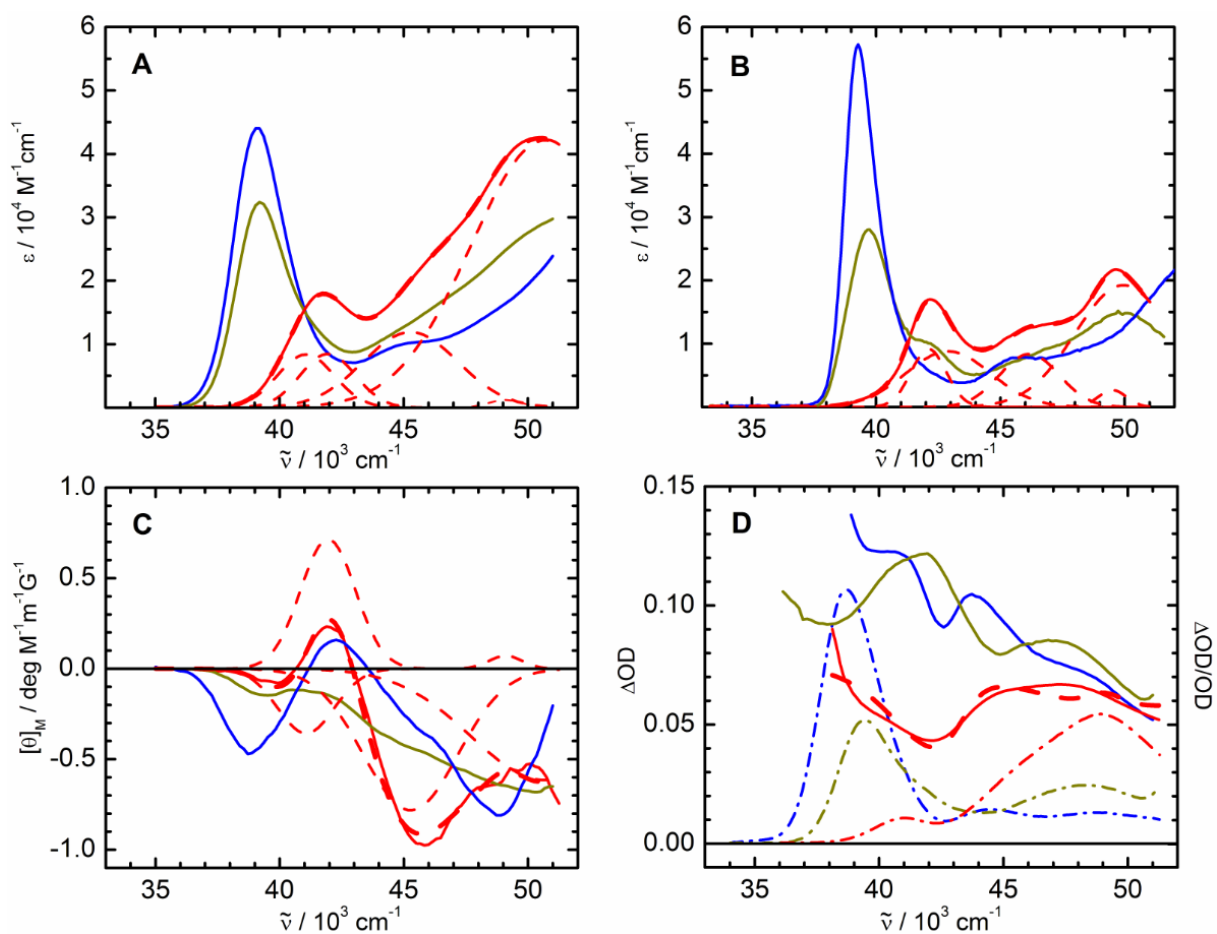
Room-temperature UV absorption spectra of **1-3** in 3-MP are shown in Figure 2.1A. The UV spectra observed at 77 K are shown in Figure 2.1B. Their absorption bands are sharper and make otherwise hidden transition more evident. For instance, the faint shoulder at ~42000 cm^{-1} in the room-temperature spectrum of *AAS*-hexasilane **2** becomes quite distinct at low temperature.

MCD spectra of **1-3** are shown in Figure 2.1C. They were very helpful for the initial detection of transitions hidden in UV absorption. Thus, in the low-energy region, the *SAS* hexasilane **1** shows two clear signals instead of a single one in absorption: a weak negative

peak at ~41100 cm^{-1} that is not detectable in absorption and a positive one at 41900 cm^{-1} that fits the first UV absorption peak. In the *AAS* hexasilane **2**, the strong UV absorption peak at ~39000 cm^{-1} appears only relatively weakly in the MCD spectrum, underscoring the importance of additional transitions at higher energies. Similarly as in *SAS*, the negative-positive-negative MCD pattern observed in the *AEA* hexasilane **3** at ~39000, ~42000, and ~48000 cm^{-1} reveals transitions that would be at best only suspected in absorption.

The LD (ΔOD) and reduced LD (LD$_r$, ΔOD/OD) spectra of **1-3** are shown in Figure 2.1D. The LD$_r$ spectra, too, point out the presence of transitions hidden in the ordinary absorption spectra.   For example, the presence of a transition at energies lower than the first absorption peak of **1**, the distinct nature of the faint absorption shoulder in **2** near 42000 cm^{-1}, and the presence of a transition just above 41000 cm^{-1} in **3** are clearly indicated.

Although one might attempt to identify the individual transitions in **1 – 3** on the basis of such qualitative observations, the simultaneous fitting with Gaussians that the collaborators of the author finally used (Table 2.1) is clearly less subjective and more reliable.

Figure 2.1. Spectra of **1** (*SAS*; red), **2** (*AAS*; dark yellow), and **3** (*AEA*; blue) in 3-MP: UV absorption at (A) room temperature and (B) at 77 K (corrected for solvent contraction by a factor of 0.784), (C) MCD, and (D) LD (dotted dashed line) and LD_r (full line). The red lines show the Gaussian fit for **1** (long dashes) and the individual Gaussian contributions (short dashes).

Table 2.1. Observed[a] and calculated electronic transitions in hexasilanes **1** (*SAS*-2, C_i), **2** (*AAS*, C_1), and **3** (*AEA*-3, C_2).

	Expt.				SAC-CI					TD-PBE0				
	$\tilde\nu$ (10^3 cm^{-1})	f	D (Debye^2)	B (Debye^2 β_e 10^4 cm^{-1})	sym.	$\tilde\nu$ (10^3 cm^{-1})	f	assignment[b]		sym.	$\tilde\nu$ (10^3 cm^{-1})	f	assignment[b]	
1	41.1	0.10	5.4	7.0	A_u	41.5	0.18	H − L	$\sigma_1\sigma^*$	A_u	43.4	0.05	H−L+1	$\sigma_1\pi^*$
	41.9	0.10	5.1	-13	A_u	42.1	0.20	H − L+1	$\sigma_1\pi^*$	A_u	43.9	0.22	H−L	$\sigma_1\sigma^*$
	45.3	0.25	12	23	A_u	44.8	0.15	H-2 − L	$\sigma_3\sigma^*$	A_u	45.4	0.14	H-1−L	$\sigma_2\sigma^*$
					A_g	45.6	0.00	H − L+2	$\sigma_1\pi_2^*$	A_g	45.8	0.00	H-2−L	$\sigma_3\sigma^*$
	49.1	0.0085	0.37	-0.68	A_u	46.6	0.01	H-2−L+1	$\sigma_3\pi^*$	A_g	46.3	0.00	H-2−L	$\sigma_3\sigma^*$
					A_g	46.7	0.00	H-1 − L	$\sigma_2\pi^*$	A_u	46.6	0.01	H-1−L+1	$\sigma_2\pi^*$
					A_g	48.3	0.00	H − L+2	$\sigma_1\pi_2^*$	A_g	47.6	0.00	H−L+2	$\sigma_1\pi_2^*$
	[50.7^d	1.36	57	26]										
2	39.0	0.24	13	1.6	A	37.4	0.61	H − L	$\sigma_1\sigma^*$	A	40.9	0.58	H − L	$\sigma_1\sigma^*$
	40.6	0.13	6.8	0.15	A	41.5	0.03	H − L+1	$\sigma_1\pi^*$	A	43.5	0.03	H − L+1	$\sigma_1\pi^*$
	44.3	0.20	9.7	8.2	A	44.2	0.02	H-2 − L	$\sigma_2\sigma^*$	A	44.5	0.02	H-1 − L	$\sigma_2\sigma^*$
					A	45.7	0.02	H-1 − L	$\sigma_3\sigma^*$	A	46.1	0.001	H-2 − L	$\sigma_3\sigma^*$
	45.8	0.028	1.3	3.9	A	47.4	0.03	H-1 − L+1	$\sigma_2\pi^*$	A	47.3	0.004	H-1 − L+1	$\sigma_2\pi^*$
					A	47.7	0.004	H-3 − L	$\sigma_4\sigma^*$	A	47.9	0.005	H-3 − L	$\sigma_4\sigma^*$
					A	48.9	0.007	H − L+3	$\sigma_1\pi^*$	A	48.0	0.004	H − L+2	$\sigma_1\pi^*$
	[51.7^d	1.16	48	36]										
3	38.9	0.15	8.2	4.3	B	36.9	0.79	H − L	$\sigma_1\sigma^*$	B	39.6	0.75	H − L	$\sigma_1\sigma^*$
	39.5	0.38	20	4.3										
	42.2	0.014	0.72	-3.1	A	41.7	0.01	H − L+1	$\sigma_1\pi^{*c}$	A	43.4	0.002	H − L+1	$\sigma_1\pi^*$
					A	43.6	0.01	H-1 − L	$\sigma_2\sigma^*$	A	44.4	0.02	H-1 − L	$\sigma_2\sigma^*$
					B	44.0	0.01	H-2 − L	$\sigma_3\sigma^*$	B	45.6	0.01	H-2 − L	$\sigma_3\sigma^*$
					A	47.0	0.01	H-3 − L	$\sigma_4\sigma^*$	A	46.3	0.00	H-3 − L	$\sigma_4\sigma^*$
	44.7	0.15	7.2	3.4	B	48.5	0.22	H-1−L+1	$\sigma_2\pi^{*c}$	B	47.1	0.18	H − L+3	$\sigma_1\sigma^*$
	48.1	0.055	2.4	13	A	49.2	0.03	H-2−L+1	$\sigma_3\pi^*$	A	47.6	0.00	H − L+2	$\sigma_1\sigma^*$
	[54.9^d	1.62	63	27]										

[a] Absorption and MCD in 3-MP, LD in stretched polyethylene. [b] H and L represent HOMO and LUMO, respectively. H-1 and H-2 are interchanged in HF and DFT. [c] The terminating MO of this transition is of strongly mixed σ and π character (Table 2.S1). [d] Probably due to solvent.

Calculated Ground-State Geometries of Peralkylated *n*-Hexasilanes 1-3

The calculated ground state geometrical parameters of peralkylated *n*-hexasilanes **1-3**, *SAS*, *AAS* and *AEA*, optimized by B3LYP/6-311G(d), are summarized in Table 2.S2-2.S4. As noted above, starting an unconstrained optimization at the two distinct conformations present in the crystal of **1** (*SAS*) in a 1:1 ratio yielded two stable C_i structures for the molecule of **1**, close in energy. The three calculated SiSiSiSi dihedral angles were $\omega = 21°$, $180°$, and $-21°$ and $\omega = 13°$, $180°$, and $-13°$ (Table 2.S2). Another local minimum structure of C_2 symmetry was also obtained. The two C_i conformations are close in energy with relative energy 1.1 kcal/mol, while the C_2 conformation is located at 2.6 kcal/mol above. The valence angles cover the range $\theta = 116° - 122°$ and the five Si-Si bond lengths are in the range $r(\text{Si-Si}) = 2.377 - 2.407$ Å with a weak bond alternation (less than 0.02Å). This shows that the geometrical strain due to lateral carbon bridges is relatively small and the *n*-hexasilane backbone is close to that in the free $n\text{-Si}_6\text{Me}_{14}$ with the same dihedral angles. Geometrical parameters of **2** (*AAS*) and **3** (*AEA*) also exhibit a similar trend. Starting from the crystal structure, the dihedral angles in **2** were calculated as $\omega = 180°$, $178°$, and $14°$. There are four possible conformations in the X-ray crystal structure of **3**. Geometry optimizations gave two conformations of C_1 and two of C_2 symmetry with relative energies within 1.0 kcal/mol. The terminal dihedral angles, ω_1 and ω_3, range from 167 to 174°, while ω_2 ranges from 108 to 130°. The valence angles are in the range $\theta = 114 - 120°$.

Calculated Electronic Transitions in Peralkylated *n*-Hexasilanes 1-3

Vertical transitions were calculated at all ground-state optimized structures. The calculated transition energy, oscillator strength, and description of the nature of the excitation are summarized in Table 2.1. The SAC-CI and TD-PBE0 calculations gave similar spectral shapes and structures, with SAC-CI transition wave numbers being mostly slightly lower and TD-PBE0 values higher than observed. The absorption spectra of **1-3** computed by SAC-CI and TD-PBE0 are compared in Figure 2.2, where the transitions are convoluted with a Gaussian of FWHM of 1500 cm^{-1}. MOs related to the transitions are displayed in Figure 2.S6. Based on a comparison of experimental with theoretical spectra, the author summarizes the results for C_i (*SAS*-2, $\omega_1 = 13°$) and C_2 (*AEA*-3) structures for compounds **1** and **3**, respectively, in Table 2.1. Computational results for the excited states for all the other conformations are compiled in the Supporting Information (Tables 2.S5-2.S8). The reasons for the selection of

the *SAS*-2 conformer for **1** are discussed below. The calculated absorption spectra of four nearly degenerate conformations of **3** are similar and, *AEA*-3 was selected because of its higher symmetry, useful for spectral assignments. All MOs that serve as starting orbitals of low-energy excitations are of essentially pure σ character, whereas the terminating orbitals can be predominantly σ* or π* in nature, or in a few cases, strongly mixed (Table 2.S1).
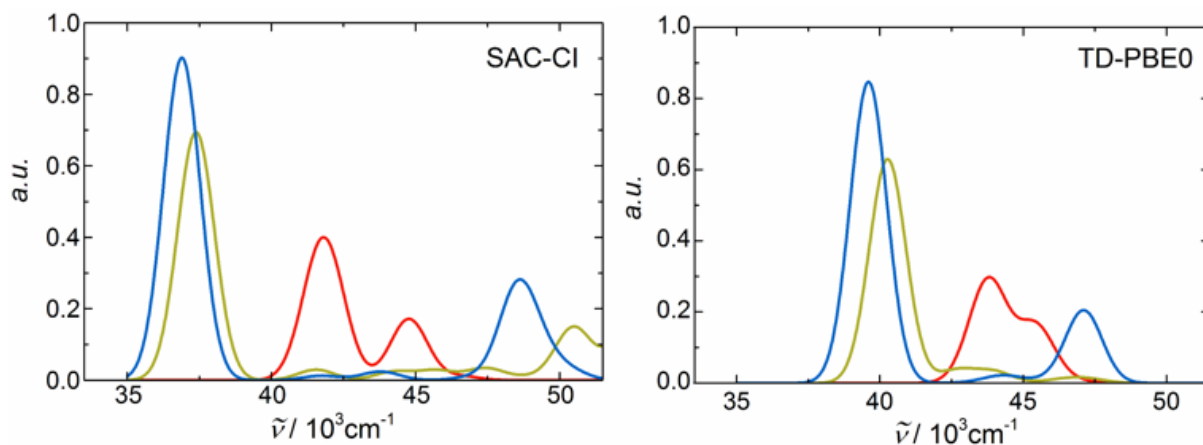

Figure 2.2. Calculated absorption spectra for **1** (*SAS*; red), **2** (*AAS*; dark yellow), and **3** (*AEA*; blue) with Gaussian convolution (FWHM of 1500 cm^{-1}). Left, SAC-CI and right, TD-DFT/PBE0.

The σ_1 and π* orbitals of *SAS* are schematically depicted in Scheme 3, where the molecular plane is defined by the six Si atoms (see Ref. 33 for a definition of σ and π character and treatment of chains that do not have a plane of symmetry).
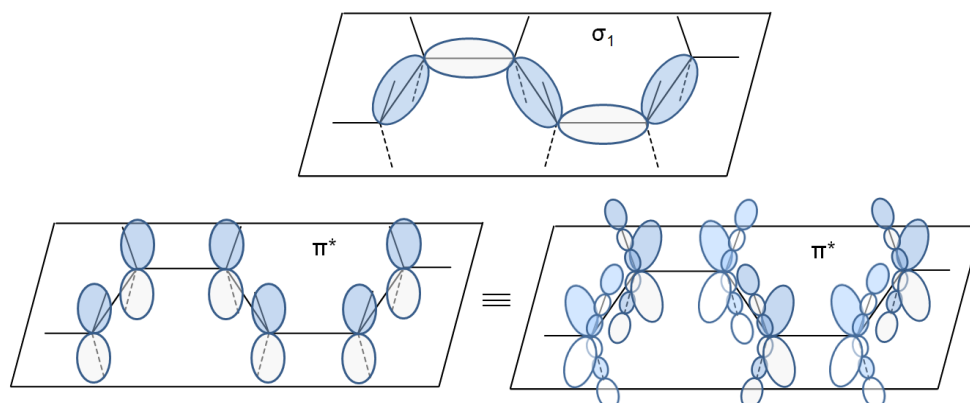
Scheme 3. Schematic representations of orbitals of *SAS*: σ_1 and π*, excluding and including contributions from the lateral substituents

Calculated Transitions in Free-Chain Permethylated *n*-Hexasilane 4

The effects of a variation of the three SiSiSiSi dihedral angles in *n*-hexasilanes on the excited states were analyzed using *n*-Si_6Me_{14} in the conformation given in Scheme 2. In these structures, one dihedral angle was varied from $\omega = 0°$ to $180°$ while the other two were restricted at *syn* ($\omega = 0°$) or *anti* ($\omega = 180°$). Thus, these conformational changes represent the structural changes of (A) *SAS* to *AAS* (ω_1), (B) *AAS* to *AAA* (ω_3), and (C) *ASA* to *AAA* (ω_2). The variation of the excitation energy and oscillator strength of *n*-Si_6Me_{14} as a function of the angles ω_1, ω_3, and ω_2 is displayed in Figures 2.3, 2.4, and 2.5, respectively. The ground state potential energy curves along these conformational changes are shown in Figure 2.S7. The energy variation along these dihedral angles relative to the most stable ground state conformation is less than 1.0 kcal/mol in the range $\omega = 30°–180°$.
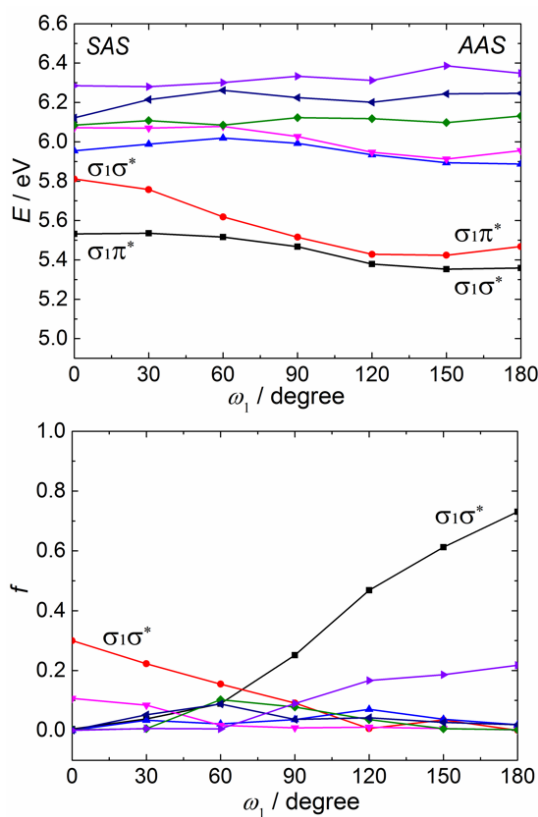
Figure 2.3. TD-PBE0 transition energy and oscillator strength of *n*-Si_6Me_{14} with $\omega_1 = 0° – 180°$, $\omega_2 = 180°$, $\omega_3 = 0°$.
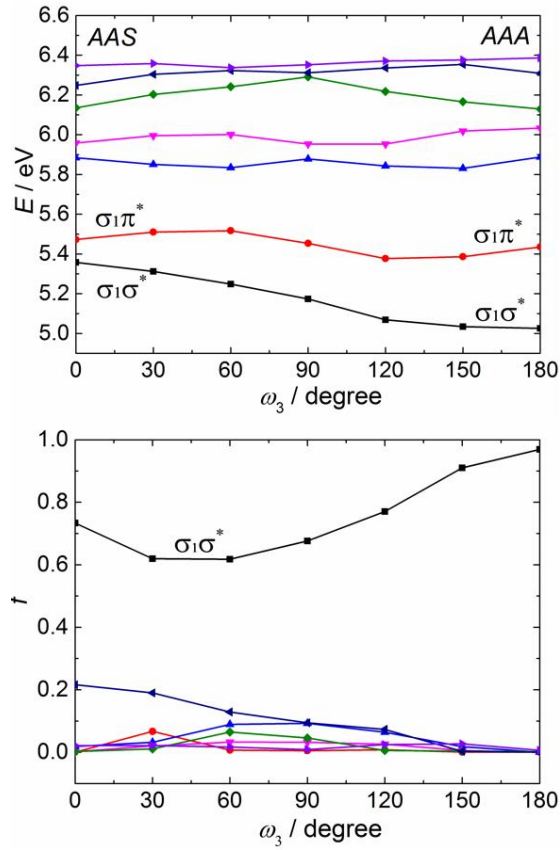
**Figure 2.4.** TD-PBE0 transition energy and oscillator strength of n-Si_6Me_{14} with $\omega_1 = 180º$, $\omega_2 = 180º$, $\omega_3 = 0º - 180º$.
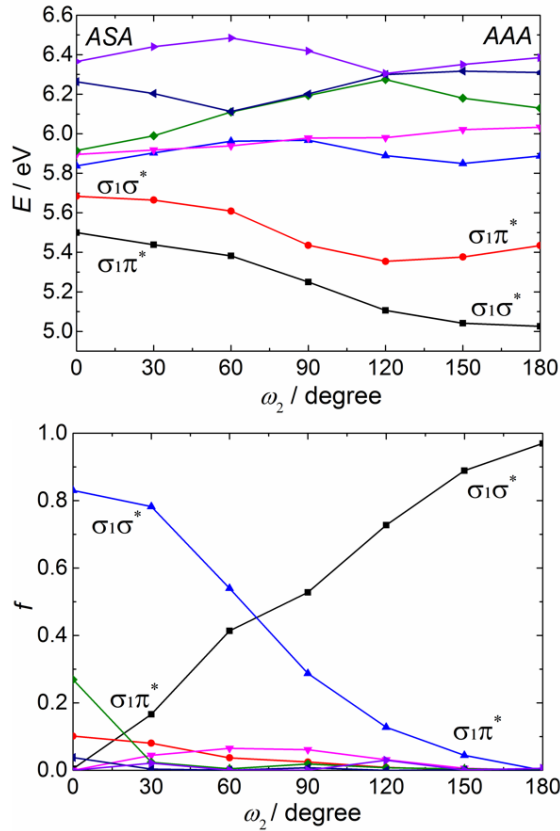
Figure 2.5. TD-PBE0 transition energy and oscillator strength of $n\text{-}Si_6Me_{14}$ with $\omega_1 = 180°$, $\omega_2 = 0° - 180°$, $\omega_3 = 180°$.

To understand the behavior of the low-lying $\sigma\pi^*$ and $\pi\pi^*$ transitions as the dihedral angle changes, the variation of the orbital energy levels of HOMO–1 to LUMO+1 was examined. The orbital energy changes for the ω_1, ω_3, and ω_2 variations are plotted in Figure 2.6A–6C together with schematic orbital shapes. Orbital back lobes are shown only when relevant to the understanding of orbital interactions. More complete views of the MOs for dihedral angles $\omega= 0°$, $90°$ and $180°$ are collected in Figures 2.S8–S10.
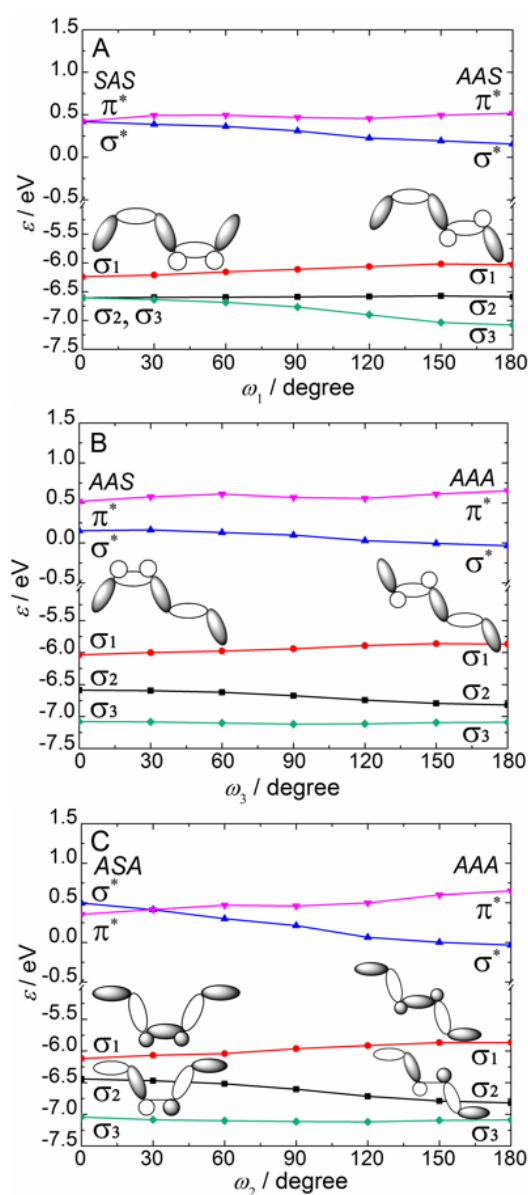
Figure 2.6. PBE0 orbital energy levels and schematic orbitals for HOMO–1 to LUMO+1 in

18

$n\text{-}Si_6Me_{14}$ with (A) $\omega_1 = 0° − 180°$, $\omega_2 = 180°$, $\omega_3 = 0°$, (B) $\omega_1 = 180°$, $\omega_2 = 180°$, $\omega_3 = 0° − 180°$, and (C) $\omega_1 = 180°$, $\omega_2 = 0° − 180°$, $\omega_3 = 180°$. The back lobes are depicted only when relevant to understanding orbital interactions.

2.4. Discussion

Although the spectra of the hexasilanes **1-3** are poorly resolved, the simultaneous fitting of UV, MCD, and LD_r spectra allows their decomposition into a series of four electronic transitions with a fair degree of confidence, although additional weak transitions could of course be present. The existence of the fifth very intense transition that is present in all three hexasilanes at ~50000 is questionable, since it lies at the very edge of the spectral window dictated by the solvents used, 3-MP and polyethylene, and it could well be an artifact due to an incompletely subtracted onset of solvent signals. The author lists this possible fifth transition since it is required for the fitting of the observed spectral curves, but shall deemphasize it in the following. Since diffuse basis set functions were not included in our calculations, the computed results are unreliable in this region, too.

The assignments of electronic transitions in the spectra are facilitated by the generally good agreement between calculations and experiment, but some uncertainties remain, mostly due to the congestion in both the observed and the calculated spectra. The author shall rely primarily on the results of the SAC-CI computations, but similar transitions, albeit at somewhat higher energies, were also obtained by the TD-PBE0 method.

The Spectra of 1 – 3. Ignoring the strong absorption at the edge of the observed region as noted above, the simultaneous fits of the room-temperature UV, MCD, and LD_r spectra of **1** – **3** suggest the presence of four transitions in the reliably observed region up to nearly 50000 cm^{-1} (Table 2.1), and additional weak ones may be present as well. The assignment of these transitions to the calculated ones is complicated by the existence of several low-energy conformations predicted for **1** and **3**. Their presence does not pose a substantial problem in the case of **3**, even though the ground-state energies of its four conformers are calculated to lie within 1 kcal/mol of each other (Table 2.S4), since the spectra calculated for all four by the SAC-CI or TD-DFT methods are very similar (Tables 2.S7 and 2.S8), with virtually all the absorption intensity located in the first transition. It is immaterial which conformer one chooses for the comparison of calculated and observed spectra, and in Table 2.1 the author chose *AEA*-3 in C_2 structure.

19

Spectrum of **1**. In this case, according to the SAC-CI method the optimized geometries lie in a region of an avoided crossing of the lowest two excited states, both of A_u symmetry. The configurations involved in the mixing are $\sigma_1\sigma^*$ and $\sigma_1\pi^*$, with only the former contributing significant oscillator strength. The computed intensities of transitions into the two states depend strongly on the choice of conformation. The observed intensities of these transitions are similar (Table 2.1), $f = 0.1$ both at 41100 and 41900 cm^{-1}. The B terms in the MCD spectrum of **1** have opposite signs, confirming that both fitted Gaussians indeed belong to distinct electronic transitions. The similar intensities of the two first bands agree with the SAC-CI results for the conformation *SAS*-2, which was chosen for Table 2.1. They do not agree with SAC-CI results for conformation *SAS*-1, computed to be 1.1 kcal/mol more stable than *SAS*-2, which predict the second transition to be much more intense than the lowest one, nor for conformation *SAS*-3, computed to be 1.5 kcal/mol less stable than *SAS*-2, and predicted to have a intense second transition and virtually no intensity in the first (Table 2.S5). To complicate matters further, TD-DFT calculations (Table 2.S6) position the region of the avoided crossing somewhat differently and place by far most of the intensity into the second transition for conformers *SAS*-1 and *SAS*-2, and into the first transition for conformer *SAS*-3.

The author does not believe that the relative ground state energies of the conformers are computed sufficiently reliably to decide which one or ones are being observed. The comparable observed intensities leave little doubt that the computations are right in that the dominant conformer or conformers have a geometry that lies in the region of an avoided crossing of the first two excited states, both of which have a mixed $\sigma_1\sigma^*$ and $\sigma_1\pi^*$ character. The computed transition moment directions, although not very different (Table 2.S9) are sufficiently far from parallel that magnetic mixing of the two states can credibly give rise to the opposite B terms observed. The negative B term of the second excited state apparently gains further strength from magnetic mixing with the state at 45300 cm^{-1}, which carries considerable intensity.

The broad and intense ($f = 0.25$) third observed peak centered at 45300 cm^{-1} is assigned to the next transition into a A_u symmetry $\sigma_3\sigma^*$ state calculated at 44800 cm^{-1}. Three additional forbidden transitions into states of A_g symmetry are calculated to be present in this general region but are not observed. Finally, a weak fourth transition with a negative *B* term is observed at 49100 cm^{-1} and is assigned to a $\sigma_3\pi^*$ transition into a state of A_u symmetry, calculated at 46600 cm^{-1}.

Spectrum of **2**. Due to the lower symmetry of **2** the author loses the useful classification

of the computed excited states into two distinct symmetry classes, and only the distinction of partial σ and π character using the definitions[33] based on NHOs obtained from NBO analysis remains (Table 2.S1). The first peak of **2** observed at 39000 cm^{-1} ($f = 0.24$) is readily assigned to the $\sigma_1\sigma^*$ transition calculated at 37400 cm^{-1} ($f = 0.61$). Beyond this point, the observations do not agree with the results of calculations. In absorption, two strong bands are observed at 40600 and 44300 cm^{-1} with $f = 0.13$ and 0.20, respectively, and a weak one at 45800 cm^{-1} with $f = 0.03$. The calculations suggest the presence of four transitions of comparable f values of 0.02 - 0.03, followed by a pair of much weaker transitions unlikely to be observed. It is not obvious how to reconcile the two sets of results and assign observed to calculated transitions.

It is improbable that the second observed band is merely a reflection of a non-Gaussian shape of the first transition and that it should be added to the first band, even though such an assignment would improve the agreement of observed and computed oscillator strengths. The two bands have distinctly different linear dichroism and, even more important, the intensities of their MCD signals differ by a factor of ten. In all probability, these are indeed two different transitions. It is noted that unlike the second B terms of **1** and **3**, the second B term in **2** has a positive sign.

The disagreement is puzzling, since the computational methods used seem to perform well for **1** and **3** and even the first transition in **2**. An obvious possible explanation is an inadequacy of the method used for geometry optimization, especially for the central dihedral angle. If the real geometry lies in an area of an avoided crossing similarly as in **1**, the resulting configuration mixing could spread oscillator strength from one transition to others. Conceivably, more than one conformer could also be present. In summary, although the experimental results for **2** dependable are considered, the present computational results for this hexasilane are not useful.

Spectrum of **3**. This hexasilane is calculated to have four conformations of nearly equal ground state energy. As pointed out above, the computed spectra are all alike and for Table 2.1 the author chose one of the C$_2$ symmetry conformations (*AEA*-3, Table 2.S4). For the first excitation, the author proposes that both Gaussian components at 38900 and 39500 cm^{-1} (total oscillator strength $f = 0.53$) should be attributed to a single $\sigma_1\sigma^*$ transition, calculated at 36900 cm^{-1} with $f = 0.79$. This assignment fits the LD$_r$ data, but an argument against it is that MCD intensity is similar for the two components, whereas the absorption intensity is different by a factor of 2.5. This would imply a somewhat different shape in absorption and MCD, and this is apparent in Figure 2.S3. The discrepancy is small and appears acceptable.

The next peak observed at 42200 cm^{-1} (f = 0.01) is assigned to a $\sigma_1\pi^*$ transition calculated at 41700 cm^{-1} (f = 0.01). This is considerable intensity for a $\sigma_1\pi^*$ transition to a state of A symmetry in C$_2$ point group, but the terminating π^* orbital has a strong σ^* admixture (Table 2.S1). The following peak, observed at 44700 cm^{-1} (f = 0.15), is assigned to a B symmetry state of $\sigma_2\pi^*$ nature (the π^* MO contains a large admixture of σ character, cf. Table 2.S1), calculated at 48500 cm^{-1} (f = 0.22). This attribution is somewhat uncertain, since three additional weak transitions with f values of 0.01 − 0.02 are predicted by SAC-CI at slightly lower energies and are presumably buried under the more intense transition. Finally, a weak (f = 0.06) fourth transition is observed at 48100 cm^{-1} and is tentatively assigned as a $\sigma_3\pi^*$ transition to a state of A symmetry calculated at 49200 cm^{-1} (f = 0.03).

Comparing now all three spectra, in both **2** (*AAS*) and **3** (*AEA*), the most easily identified lowest energy intense absorption band is red-shifted by about 2000 cm^{-1} relative to **1** (*SAS*) and intensified by a factor of 2.5 and 5, respectively (Figure 2.1). This behavior is qualitatively reproduced by the SAC-CI method; the first peaks are calculated at 37400 and 36900 cm^{-1} with an oscillator strength f = 0.61 and 0.79 for **2** and **3**, respectively, compared to the 41500 and 42100 cm^{-1} and f = 0.18 and 0.20 calculated for **1**. The same trend with respect to the variation of the absorption energy is also calculated for *n*-Si$_6$Me$_{14}$ (**4**); *SAS-AAS* (Figure 2.3) and *AAS-AAA* (Figure 2.4). The origin of the red shift is the destabilization of σ_1 orbital and stabilization of σ^* orbital as the dihedral angle increases (Figure 2.6). Frontier MOs of **1**, **2** and **3** are similar to those of the corresponding MOs of *n*-Si$_6$Me$_{14}$ in *SAS, AAS* and *AEA* conformations, respectively. Figure 2.2 shows that the TD-DFT method performs less well in that it exaggerates the differences between the first peaks of the three compounds and fails to account for the nearly identical first excitation energies of **2** and **3**.

In summary, the computed spectra of **1** − **3** appear to be characterized by a nearly degenerate pair of excitations from the HOMO, σ_1, to the lowest unoccupied MOs of σ and π symmetry (σ^* and π^*) at about 40000 cm^{-1}, with the former strong and the latter weak, followed by another nearly degenerate pair of similar but weaker transitions from the HOMO-1 (σ_2) roughly 5000 cm^{-1} higher, plus additional weak transitions. These results are nicely compatible with the experimental observations for **1** and **3**, and in the case of the first transition, also for **2**, but many of the expected very weak transitions remain unobserved. The detailed arrangement of the computed transition energies and intensities is determined by the conformation of the silicon backbone, and this will be systematically investigated next.

The Spectra of 4. The three types of variation of dihedral angles (ω_1-ω_3) in *n*-Si$_6$Me$_{14}$ (**4**)

that were examined are instructive for seeing how conformation control affects the optical properties of *n*-hexasilanes (Figures 2.3-2.5).

The author first focuses on the variation of angle ω_1 (Figure 2.3). At $\omega_1 = 0$ (*SAS*), the S_1 state is reached by a $\sigma\pi^*$ excitation and the nearby S_2 state by a $\sigma\sigma^*$ excitation. When ω_1 is increased, symmetry is lowered. The S_1 and S_2 states are still represented by these two configurations, which now mix. The $\sigma\sigma^*$ component carries a large oscillator strength and the $\sigma\pi^*$ only a small one, and the oscillator strength of transitions into the two states depends on their ratio. They undergo an avoided crossing at around $\omega_1 = 60°$, as seen in the variation of the oscillator strength. At the *AAS* ($\omega_1 = 180°$) conformation symmetry is reestablished, and the S_1 state is reached by a $\sigma\sigma^*$ excitation with a strong oscillator strength of $f = 0.7$. The response of the low-energy part of the spectrum to the variation of the dihedral angle ω_1 is thus dictated by the interchange of the order of the $\sigma\pi^*$ and $\sigma\sigma^*$ excitation and in that sense is strongly reminiscent of the conformational response of the spectrum of *n*-tetrasilane.[9,35]

The energy of both transitions drops as the conformation changes from *SAS* to *AAS*. The energy of the $\sigma\sigma^*$ transition is lowered by 0.45 eV, from 5.81 to 5.36 eV, and that of the $\sigma\pi^*$ transition by 0.07 eV, from 5.54 to 5.47 eV, which agrees well with the trend found in peralkylated hexasilanes **1** (*SAS*) and **2** (*AAS*). This trend can be qualitatively understood as due to σ and σ^* orbital energy change (Figure 2.6A).

Among the higher states, in *SAS* ($\omega_1 = 0$), which is close to the conformation of **1** with absorptions at ~45300 and 49100 cm^{-1}, transition to the S_4 state characterized as $\sigma_3\sigma^*$ has considerable oscillator strength. In *AAS* ($\omega_1 = 180°$), which corresponds to **2** with the absorption peak in the higher energy region, transition to the S_6 state has a large oscillator strength. Other transitions do not have notable intensity.

Next, the author considers the conformational change from *AAS* to *AAA* by a variation of the dihedral angle ω_3 while the other angles are fixed at $\omega_1 = \omega_2 = 180°$ (Figure 2.4). Now, the energy of the $\sigma_1\sigma^*$ configuration lies below that of the $\sigma_1\pi^*$ configuration at *AAS*, *AAA*, and all intermediate geometries. The energies of the S_1 and S_2 states are well separated and the mixing of the dominant $\sigma\sigma^*$ and $\sigma\pi^*$ configurations is small at all geometries. There is no avoided crossing and the transition to the S_1 state is always intense. At the *AAA* conformation ($\omega_1 = 180°$), only the S_1 state has a large oscillator strength ($f = ~1.0$) and those of all other transitions are nearly zero, showing that the $\sigma_1\sigma^*$ configuration is significant in the S_1 state. Transitions to the S_2 and S_3 states have weak intensity ($f < 0.1$) all along this ω_3 variation. In

brief, the variation of the dihedral angle ω_3 is expected to produce no dramatic spectral changes other than a significant drop of the energy of the first transition as one proceeds from *AAS* to *AAA* and in that regard is very different from the variation of ω_1.

Finally, during the conformational change from *ASA* to *AAA* by variation of the angle ω_2 (Figure 2.5), the $S_1(1B)$ and $S_2(2B)$ states undergo an avoided crossing and interchange their character ($\sigma\sigma^*$, $\sigma\pi^*$), even though they are separated by about 0.3 ($\omega_2 = 0°$) and 0.4 ($\omega_2 = 180°$) eV. Their oscillator strengths change drastically as their content of the $\sigma\sigma^*$ component changes during the process. The situation is thus very similar to that encountered with the variation of the angle ω_1. At $\omega_2 = 120°$, the conformation and the expected spectra correspond to **3** (*AEA*). The *ASA* conformation shows strong absorption only in the high energy region, above 5.8 eV.

A rationalization of the effects of conformational changes on the low-energy part of the spectra thus follows from the knowledge of the relative energies of the lowest $\sigma_1\sigma^*$ and $\sigma_1\pi^*$ configurations. Since the energy of the $\sigma_1\pi^*$ configuration is almost independent of conformation (Figures 2.3 – 2.5), the conformational behavior of the spectra is primarily determined by the effect of dihedral angles on the energy of the lowest $\sigma_1\sigma^*$ configuration. This can be understood in terms of the energies of the σ_1 and the lowest σ^* MOs, and thus ultimately in terms of the extremely simple Ladder C model.[37,49] In this model, relative energies of conformations are dictated solely by the vicinal (1,4) resonance integrals between NHOs located at the Si atoms of the bond that is being twisted. At a dihedral angle of 0° (syn), this resonance integral is negative, near a dihedral angle of 90° it goes through zero, and at a dihedral angle of 180° it is positive. Combined with the knowledge of signs of the coefficients of NHOs in the MOs σ and σ^*, this permits first-order perturbation theory estimates of the effect of dihedral angle changes on the energies of these orbitals. Note that the change in the sign of the resonance integral is due to the π component of the overlap of the vicinal NHOs and in that sense the conformational isomerization of a saturated chain is clearly related to the geometrical cis-trans isomerization of a double bond.

These arguments show that as the angle ω_1 increases (Figure 2.6A), the orbital σ_1 (HOMO) should be destabilized and the σ^* orbital stabilized, and this rationalizes the strong drop of the $\sigma\sigma^*$ transition energy from *SAS* to *AAS* and the change in the order of energies of the lowest $\sigma_1\sigma^*$ and $\sigma_1\pi^*$ configurations. In contrast, as the angle ω_3 is increased (Figure 2.6B), the further destabilization of the σ and stabilization of the σ^* MO merely lowers the energy of the already lowest $\sigma_1\sigma^*$ configuration. It causes no changes in the order of the $\sigma\sigma^*$

24

and σπ* configurations and the transition to the S_1 state drops in energy but keeps its strong oscillator strength throughout. Finally, when ω_2 is increased (Figure 2.6C), the changes in the σ_1 and σ* energies are very similar to those seen in Figure 2.6A and are rationalized in the same way. They once again lead to an interchange of the σσ* and σπ* nature of the lowest two transitions, to an avoided crossing, and to dramatic effects on transition intensities, in addition to a change in the energy of the first transition.

2.5. Summary

The electronic excited states of three conformationally controlled peralkylated *n*-hexasilanes **1** - **3** (*SAS*, *AAS*, and *AEA*) have been investigated using UV absorption, MCD, and LD spectroscopy. A simultaneous decomposition of the three types of spectra into Gaussian contributions has played a key role in the assignment of individual electronic transitions and determination of their wave numbers, oscillator strength *f* and MCD *B* terms. SAC-CI and TD-PBE0 calculations have been used to analyze the nature of the observed excitations. They provided useful results for the hexasilanes **1** and **3**, but not for **2**. The striking dependence of the energy and intensity of the first intense transition, located near 40000 cm^{-1}, on silicon backbone conformation results from changes in the energies of the σ_1 and σ* orbitals, which can be understood in very simple terms. The conformational dependence of the excitation energies and transition properties is examined more generally on the free chain *n*-Si_6Me_{14} in various combinations of dihedral angles. An avoided crossing between σσ* and σπ* states occurs in the *SAS-AAS* and *ASA-AAA* conformational transformations and causes dramatic differences in transition intensities.

References

[1]   H. Gilman, W. H. Atwell, G. L. Schwebke, *Chem. Ind.* **1964**, 1063.

[2]   H. Gilman, W. H. Atwell, G. L. Shwebke, *J. Organomet. Chem.* **1964**, *2*, 369-371.

[3]   H. Sakurai, M. Kumada, *Bull. Chem. Soc. Jpn.* **1964**, *37*, 1894.

[4]   D. N. Hague, R. H. Prince, *Chem. Age.* **1964**, 1492.

[5]   K. Obata, M. Kira, *Organometallics* **1999**, *18*, 2216-2222.

[6]   H. A. Fogarty, R. Imhof, J. Michl, *Proc. Natl. Acad. Sci. USA* **2004**, *101*, 10517-10522.

[7]   M. K. Raymond, *Ph.D. Dissertation, University of Colorado, Boulder* **1997**.

[8]   H. A. Fogarty, *Ph.D. Dissertation, University of Colorado, Boulder* **2005**.

[9]   H. Tsuji, H. A. Fogarty, M. Ehara, R. Fukuda, D. L. Casher, K. Tamao, H. Nakatsuji, J. Michl, *Chem. Eur. J.* **2014**, *20*, 9431-9441.

[10] S. Mazières, M. K. Raymond, G. Raabe, A. Prodi, J. Michl, *J. Am. Chem. Soc.* **1997**, *119*, 6682-6683.

[11] D. J. Williams, *Angew. Chem.* **1984**, *96*, 637-651.

[12] H. Kishida, T. Hasegawa, Y. Iwasa, T. Koda, Y. Tokura, *Phys. Rev. Lett.* **1993**, *70*, 3724-3727.

[13] R. G. Kepler, Z. G. Soos, In Primary Photoexcitations in Conjugated Polymers; N. S. Sariciftci, Ed.; World Scientific: Singapore, **1997**, p 363-383.

[14] M. Kumada, K. Tamao, *Adv. Organomet. Chem.* **1968**, *6*, 19-117.

[15] R. D. Miller, J. Michl, *Chem. Rev.* **1989**, *89*, 1359-1410.

[16] M. Kira, T. Miyazawa, in *The Chemistry of Organic Silicon Compounds* Vol. 2; (Eds.: Z. Rappoport, Y. Apeloig, Wiley, Chichester, **1998**, p. 1311.

[17] J. Michl, R. West, in *Silicon Containing Polymers* (Eds.: R. G. Jones, W. Ando, J. Chojnowski), Kluwer Academic, Dordrecht (The Netherlands), **2000**, p. 499.

[18] R. West, in *The Chemistry of Organic Silicon Compounds* Vol. 3 (Eds.: Z. Rappoport, Y. Apeloig), Wiley, Chichester, **2001**, p. 541.

[19] H. A. Fogarty, D. L. Casher, R. Imhof, T. Schepers, D. W. Rooklin, J. Michl, *Pure Appl. Chem.* **2003**, *75*, 999-1020.

[20] H. Tsuji, J. Michl, A. Toshimitsu, K. Tamao, *J. Synth. Org. Chem. Jpn.* **2002**, *60*, 762-773.

[21] H. Tsuji, J. Michl, K. Tamao, *J. Organomet. Chem.* **2003**, *685*, 9-14.

[22] L. A. Harrah, J. M. Zeigler, *J. Polym. Sci. Polym. Lett. Ed.* **1985**, *23*, 209-211.

[23] P. Trefoñas, J. R. Damewood, R. West, R. D. Miller, *Organometallics* **1985**, *4*, 1318-1319.

[24] T. Gahimer, W. J. Welch, *Polymer* **1996**, *37*, 1815-1823.

[25] T. Sanji, K. Sakamoto, H. Sakurai, K. Ono, *Maclomolecules* **1999**, *32*, 3788-3794.

[26] S. S. Bukalov, L. A. Leites, R. West, *Maclomolecules* **2001**, *34*, 6003-6004.

[27] K. Obata, M. Kira, *RIKEN Rev.* **1995**, *11*, 39-40.

[28] H. A. Fogarty, C. H. Ottosson, J. Michl, *J. Mol. Struct.* **2000**, *556*, 105-121.

[29] H. A. Fogarty, C. H. Ottosson, J. Michl, *J. Mol. Struct.* **2000**, *506*, 243-255.

[30] J. Michl, R. West, *Acc. Chem. Res.* **2000**, *33*, 821-823.

[31] H. A. Fogarty, C. H. Ottosson, J. Michl, *J. Phys. Chem. B* **2006**, *110*, 25485-25495.

[32] H. Tsuji, M. Terada, A. Toshimitsu, K. Tamao, *J. Am. Chem. Soc.* **2003**, *125*, 7486-7487.

[33] A. Bande, J. Michl, *Chem. Eur. J.* **2009**, *15*, 8504-8517.

[34] R. Crespo, M. C. Piqueras, J. Michl, *Theor. Chem. Acc.* **2007**, *118*, 81-87.

[35] H. Teramae, J. Michl, *Mol. Cryst. Liq. Cryst.* **1994**, *256*, 149-159.

[36] H. S. Plitt, J. W. Downing, M. K. Raymond, V. Balaji, J. Michl, *J. Chem. Soc. Faraday Trans.* **1994**, *90*, 1653-1662.

[37] T. Schepers, J. Michl, *J. Phys. Org. Chem.* **2002**, *15*, 490-498.

[38] F. Neumann, H. Teramae, J. W. Downing, J. Michl, *J. Am. Chem. Soc.* **1998**, *120*, 573-582.

[39] B. Albinsson, D. Antic, F. Neumann, J. Michl, *J. Phys. Chem. A* **1999**, *103*, 2184-2196.

[40] C. H. Ottosson, J. Michl, *J. Phys. Chem. A* **2000**, *104*, 3367-3380.

[41] R. West, *J. Organomet. Chem.* **2003**, *685*, 6-8.

[42] S. Ohashi, Y. Naruse, S. Inagaki, *J. Organomet. Chem.* **2003**, *682*, 119-122.

[43] R. Crespo, H. Teramae, D. Antic, J. Michl, *Chem. Phys.* **1999**, *244*, 203-214.

[44] R. Crespo, M. Merchan, J. Michl, *J. Phys. Chem. A* **2000**, *104*, 8593-8599.

[45] M. C. Piqueras, M. Merchan, R. Crespo, J. Michl, *J. Phys. Chem. A* **2002**, *106*, 9868-9873.

[46] B. Albinsson, H. Teramae, J. W. Downing, J. Michl, *Chem. Eur. J.* **1996**, *2*, 529-538.

[47] M. C. Piqueras, R. Crespo, J. Michl, *J. Phys. Chem. A* **2003**, *107*, 4661-4668.

[48] D. W. Rooklin, T. Schepers, M. K. Raymond-Johansson, J. Michl, *Photochem. Photobiol. Sci.* **2003**, *2*, 511-517.

[49] H. S. Plitt, J. Michl, *Chem. Phys. Lett.* **1992**, *198*, 400-405.

[50] R. Imhof, H. Teramae, J. Michl, *Chem. Phys. Lett.* **1997**, *270*, 500-505.

[51] R. Imhof, D. Antic, D. E. David, J. Michl, *J. Phys. Chem. A* **1997**, *101*, 4579-4586.

[52] H. A. Fogarty, H. Tsuji, D. E. David, C. H. Ottosson, J. Michl, K. Tamao, M. Ehara, H. Nakatsuji, *J. Phys. Chem. A* **2002**, *106*, 2369-2373.

[53] K. Tamao, H. Tsuji, M. Terada, M. Asahara, S. Yamaguchi, A. Toshimitsu, *Angew. Chem. Int. Ed.* **2000**, *112*, 3425-3428.

[54] H. Tsuji, A. Toshimitsu, K. Tamao, J. Michl, *J. Phys. Chem. A* **2001**, *105*, 10246-10248.

[55] S. Seki, K. Okamoto, Y. Matsuji, S. Tagawa, H. Tsuji, A. Toshimitsu, K.Tamao, *Chem. Phys. Lett.* **2003**, *380*, 141-145.

[56] H. Mallesha, H. Tsuji, K. Tamao, *Organometallics* **2004**, *23*, 1639-1642.

[57] H. Tsuji, A. Fukazawa, S. Yamaguchi, A. Toshimitsu, K. Tamao, *Organometallics* **2004**, *23*, 3375-3377.

[58] A. Fukazawa, H. Tsuji, K. Tamao, *J. Am. Chem. Soc.* **2006**, *128*, 6800-6801.

[59] R. Tanaka, M. Unno, H. Matsuoto, *Chem. Lett.* **1999**, 595-596.

[60] I. El-Sayed, Y. Hatanaka, C. Muguruma, S. Shimada, M. Tanaka, N. Koga, M. Mikami,

J. Am. Chem. Soc. **1999**, *121*, 5095-5096.

[61] I. El-Sayed, Y. Hatanaka, S. Onozawa, M. Tanaka, *J. Am. Chem. Soc.* **2001**, *123*, 3597-3598.

[62] Y. Hatanaka, *J. Synth. Org. Chem. Jpn.* **2001**, *59*, 996-1004.

[63] Y. Hatanaka, *J. Organomet. Chem.* **2003**, *685*, 207-217.

[64] K. Obata, C. Kabuto, M. Kira, *J. Am. Chem. Soc.* **1997**, *119*, 11345-11346.

[65] H. S. Oh, L. S. Park, Y. Kawakami, *Chirality* **2003**, *15*, 646-653.

[66] T. Sanji, K. Takase, H. Sakurai, *Bull. Chem. Soc. Jpn.* **2004**, *77*, 1607-1611.

[67] M. Fujiki, *J. Am. Chem. Soc.* **1994**, *116*, 6017-6018.

[68] M. Fujiki, *J. Organomet. Chem.* **2003**, *685*, 15-34.

[69] H. Okumura, A. Kawaguchi, A. Harada, *Macromol. Rapid Commun* **2002**, *23*, 781.

[70] K. Sakamoto, T. Naruoka, M. Kira, *Chem. Lett.* **2003**, *32*, 380-381.

[71] T. Sanji, A. Yoshiwara, H. Sakurai, M. Tanaka, *Chem. Commun.* **2003**, 1506-1507.

[72] T. Sanji, M. Kato, M. Tanaka, *Maclomolecules* **2005**, *38*, 4034-4037.

[73] T. Sanji, N. Kato, M. Tanaka, *Chem. Lett.* **2005**, *34*, 1144-1145.

[74] T. Sanji, N. Kato, M. Kato, A. Tanaka, *Angew. Chem.* **2005**, *117*, 7467-7470.

[75] H. Nakatsuji, *Chem. Phys. Lett.* **1978**, *59*, 362-364.

[76] H. Nakatsuji, *Chem. Phys. Lett.* **1979**, *67*, 329-333.

[77] C. Adamo, V. Barone, *J. Chem. Phys.* **1998**, *108*, 664-675.

[78] E. C. Murray, R. N. Keller, *J. Org. Chem.* **1969**, *34*, 2234-2235.

[79] M. Klessinger, J. Michl, *Excited States and Photochemistry of Organic Molecules*, Wiley-VCH, Weinheim, **1995**.

[80] A. J. McCaffery, P. J. Stephens, P. N. Schatz, *Inorg. Chem.* **1967**, *6*, 1614-1625.

[81] J. Michl, E. W. Thulstrup, *Spectroscopy with Polarized Light: Solute Alignment by Photoselection in Liquid Crystals, Polymers, and Membranes*, Wiley-VCH, Weinheim, **1995**.

[82] A. D. Becke, *J. Chem. Phys.* **1993**, *98*, 5648-5652.

[83] R. Krishnan, J. S. Binkley, R. Seeger, J. A. Pople, *J. Chem. Phys.* **1980**, *72*, 650-654.

[84] C. Adamo, D. Jacquemin, *Chem. Soc. Rev.* **2013**, *42*, 845-856.

[85] D. Jacquemin, E. A. Perpète, I. Ciofini, C. Adamo, R. Valero, Y. Zhao, D. G. Truhlar, *J. Chem. Theory Comput.* **2010**, *6*, 2071−2085.

[86] D. Bousquet, R. Fukuda, P. Maitarad, D. Jacquemin, I. Ciofini, C. Adamo, M. Ehara, *J. Chem. Theory Comput.* **2013**, *9*, 2368−2379.

[87] D. Bousquet, R. Fukuda, D. Jacquemin, I. Ciofini, C. Adamo, M. Ehara, *J. Chem. Theory Comput.* **2014**, *10*, 3969−3979.

[88] H. Nakatsuji, in *Computational Chemistry-Reviews of Current Trends*, Vol. 2 (Ed.: J. Leszczynski), World Scientific, Singapore, **1997**, pp. 62-124.

[89] M. Ehara, J. Hasegawa, H. Nakatsuji, in T*heory and Applications of Computational Chemistry: The First 40 Years* (Eds.: C. E. Dykstra, G. Frenking, K. S. Kim, G. E. Scuseria), Elsevier, Oxford, **2005**.

[90] H. Nakatsuji, *Chem. Phys.* **1983**, *75*, 425-441.

[91] R. Fukuda, H. Nakatsuji, *J. Chem. Phys.* **2008**, *128*, 094105.

[92] A. D. McLean, G. S. Chandler, *J. Chem. Phys.* **1980**, *72*, 5639-5648.

[93] T. H. Dunning, Jr., P. J. Hay, in *Methods of Electronic Structure Theory* (Ed.: H. F. Schaefer III), Plenum Press, New York, **1977**.

[94] R. Fukuda, M. Ehara, *J. Comput. Chem.* **2014**, *35*, 2163-2176.

[95] M. Ehara, R. Fukuda, C. Adamo, I. Ciofini, *J. Comput. Chem.* **2013**, *34*, 2498-2501.

[96] C. Adamo, T. L. Bahers, M. Savarese, L. Wilbraham, G. García, R. Fukuda, M. Ehara, N. Rega, I. Ciofini, *Coord. Chem. Rev.* **2015**, *304-305*, 166-178.

[97] Gaussian 09, Revision B.01, M. J. Frisch, G. W. Trucks, H. B. Schlegel, G. E. Scuseria, M. A. Robb, J. R. Cheeseman, G. Scalmani, V. Barone, B. Mennucci, G. A. Petersson, H. Nakatsuji, M. Caricato, X. Li, H. P. Hratchian, A. F. Izmaylov, J. Bloino, G. Zheng, J. L. Sonnenberg, M. Hada, M. Ehara, K. Toyota, R. Fukuda, J. Hasegawa, M. Ishida, T. Nakajima, Y. Honda, O. Kitao, H. Nakai, T. Vreven, J. A. Montgomery, Jr., J. E. Peralta, F. Ogliaro, M. Bearpark, J. J. Heyd, E. Brothers, K. N. Kudin, V. N. Staroverov, R. Kobayashi, J. Normand, K. Raghavachari, A. Rendell, J. C. Burant, S. S. Iyengar, J. Tomasi, M. Cossi, N. Rega, J. M. Millam, M. Klene, J. E. Knox, J. B., Cross, V. Bakken, C. Adamo, J. Jaramillo, R. Gomperts, R. E. Stratmann, O. Yazyev, A. J. Austin, R. Cammi, C. Pomelli, J. W. Ochterski, R. L. Martin, K. Morokuma, V. G. Zakrzewski, G. A. Voth, P. Salvador, J. J. Dannenberg, S. Dapprich, A. D. Daniels, O. Farkas, J. B. Foresman, J. V. Ortiz, J. Cioslowski, D. J. Fox, Gaussian, Inc. Wallingford CT, **2010**.

[98] F. Weinhold, J. E. Carpenter, in The Structure of Small Molecules and Ions, Ed. R. Naaman and Z. Vager (Plenum, 1988) 227-236.

Supporting Information

Table 2.S1. Percentages of σ and π character in frontier MOs of *SAS*, *AAS*, and *AEA* calculated by natural hybrid orbitals of RHF/6-311(2d)(Si)+D95v(C,H).

	SAS-2		*AAS*		*AEA*-3	
	σ(%)	π(%)	σ(%)	π(%)	σ(%)	π(%)
L+3	55	45	3	97	32	68
L+2	48	52	66	34	22	78
L+1	12	88	16	84	57	43
L	91	9	90	10	85	15
H	100	0	100	0	100	0
H-1	100	0	100	0	99	1
H-2	99	1	100	0	98	2
H-3	99	1	100	0	98	2

Table 2.S2. Calculated geometrical parameters of peralkylated hexasilanes **1-3**.

compound	dihedral angle (°)		valence angle (°)		Si-Si distance (Å)	
1 (*SAS*)						
SAS-1 (C$_i$)	ω_1	21.1	θ_1	122.0	r_1	2.388
	ω_2	180.0	θ_2	117.3	r_2	2.407
	ω_3	-21.1	θ_3	117.3	r_3	2.394
			θ_4	122.0	r_4	2.407
					r_5	2.388
SAS-2 (C$_i$)	ω_1	13.2	θ_1	121.3	r_1	2.389
	ω_2	180.0	θ_2	117.9	r_2	2.397
	ω_3	-13.2	θ_3	117.9	r_3	2.391
			θ_4	121.3	r_4	2.397
					r_5	2.389
SAS-3 (C$_2$)	ω_1	29.6	θ_1	120.8	r_1	2.387
	ω_2	174.9	θ_2	116.3	r_2	2.377
	ω_3	29.6	θ_3	116.3	r_3	2.394
			θ_4	120.8	r_4	2.377
					r_5	2.387
2 (*AAS*)						
	ω_1	13.6	θ_1	122.4	r_1	2.387
	ω_2	178.0	θ_2	114.8	r_2	2.411
	ω_3	179.7	θ_3	117.3	r_3	2.417
			θ_4	115.8	r_4	2.379
					r_5	2.418
3 (*AEA*)						
AEA-1 (C$_1$)	ω_1	173.7	θ_1	116.6	r_1	2.412
	ω_2	118.9	θ_2	116.6	r_2	2.380
	ω_3	167.4	θ_3	119.9	r_3	2.453
			θ_4	116.2	r_4	2.385
					r_5	2.417
AEA-2 (C$_1$)	ω_1	174.0	θ_1	116.7	r_1	2.416
	ω_2	129.7	θ_2	116.2	r_2	2.391
	ω_3	171.1	θ_3	119.2	r_3	2.455
			θ_4	115.4	r_4	2.399
					r_5	2.417
AEA-3 (C$_2$)	ω_1	168.9	θ_1	114.5	r_1	2.417
	ω_2	118.5	θ_2	120.1	r_2	2.385

	ω_3	168.9	θ_3	120.1	r_3	2.460
			θ_4	114.5	r_4	2.385
					r_5	2.417
AEA-4 (C$_2$)	ω_1	169.2	θ_1	116.6	r_1	2.415
	ω_2	108.8	θ_2	117.8	r_2	2.377
	ω_3	169.2	θ_3	117.8	r_3	2.470
			θ_4	116.6	r_4	2.377
					r_5	2.415

Table 2.S3. Energy and dihedral angles of three local minima in compound **1** (*SAS*) calculated by B3LYP/6-311G(d).

Conf.	Sym.	Total energy (au)	ΔE (kcal/mol)	Dihedral angle (degree) ω_1	ω_2	ω_3
SAS-1	C_i	-2763.15737	0.00	21.1	180.0	−21.1
SAS-2	C_i	-2763.15563	1.09	13.2	180.0	−13.2
SAS-3	C_2	-2763.15325	2.58	29.6	174.9	29.6

Table 2.S4. Energy and dihedral angles of four local minima in compound **3** (*AEA*) calculated by B3LYP/6-311G(d).

Conf.	Sym.	Total energy (au)	ΔE (kcal/mol)	Dihedral angle (degree) ω_1	ω_2	ω_3
AEA-1	C_1	-2763.13630	0.00	173.7	118.9	167.4
AEA-2	C_1	-2763.13589	0.25	174.0	129.7	171.1
AEA-3	C_2	-2763.13477	0.70	168.9	118.5	168.9
AEA-4	C_2	-2763.13428	1.01	169.2	108.8	169.2

Table 2.S5. Excited states of compound **1** (*SAS*) calculated by SAC-CI/6-311G(2d) (Si)+D95v(C,H).

Num.	Sym.	ΔE ($10^3 \times cm^{-1}$)	f	Character[a]
SAS-1 (C$_i$)				
1	Au	39.7	0.082	H − L
2	Au	42.5	0.283	H − L+1
3	Ag	44.8	0.000	H-1 − L
4	Au	45.1	0.041	H-2 − L
5	Au	47.5	0.153	H-2 − L+1
6	Ag	47.9	0.000	H-1 − L
7	Ag	49.0	0.000	H-1 − L+1
8	Ag	50.6	0.000	H − L+3
9	Au	52.7	0.176	H-3 − L
10	Ag	53.5	0.000	H-4 − L
SAS-2 (C$_i$)				
1	Au	41.5	0.182	H − L, H − L+1
2	Au	42.1	0.200	H − L, H − L+1
3	Au	44.8	0.151	H-2 − L
4	Ag	45.6	0.000	H − L+2
5	Au	46.6	0.010	H-2 − L+1
6	Ag	46.7	0.000	H-1 − L
7	Ag	48.3	0.000	H − L+2
8	Ag	50.2	0.000	H − L+3
9	Au	53.5	0.473	H-3 − L
10	Ag	53.9	0.000	H-2 − L+2
SAS-3 (C$_2$)				
1	B	40.9	0.386	H − L
2	A	42.4	0.003	H − L+1
3	B	44.3	0.106	H-2 − L
4	B	46.6	0.120	H − L+2
5	A	46.7	0.010	H-1 − L
6	A	47.6	0.003	H-2 − L+1
7	B	48.9	0.043	H-2 − L+2
8	A	50.2	0.001	H − L+3
9	B	52.2	0.105	H-3 − L
10	A	54.5	0.007	H-4 − L

[a] H and L represent HOMO and LUMO, respectively.

Table 2.S6. Excited states of compound **1** (*SAS*) calculated by PBE0/6-311G(d).

Num.	Sym.	ΔE $(10^3 \times cm^{-1})$	f	Character[a]
SAS-1 (C$_i$)				
1	Au	41.9	0.053	H − L
2	Au	44.3	0.210	H − L+1
3	Ag	45.1	0.000	H-1 − L
4	Au	45.7	0.036	H-2 − L
5	Au	47.0	0.107	H-2 − L+1
6	Ag	47.2	0.000	H-1 − L+1
7	Ag	47.6	0.000	H − L+2
SAS-2 (C$_i$)				
1	Au	43.4	0.049	H − L+1
2	Au	43.9	0.219	H − L
3	Au	45.4	0.140	H-1 − L
4	Ag	45.8	0.000	H-2 − L
5	Ag	46.3	0.000	H-2 − L
6	Au	46.6	0.008	H-1 − L+1
7	Ag	47.6	0.000	H − L+2
SAS-3 (C$_2$)				
1	B	43.4	0.298	H − L
2	A	44.4	0.003	H − L+1
3	B	45.4	0.090	H-1 − L
4	A	46.2	0.010	H-2 − L
5	B	47.3	0.120	H − L+2
6	A	47.7	0.002	H-1 − L+1
7	B	48.4	0.002	H − L+2

[a] H and L represent HOMO and LUMO, respectively.

Table 2.S7. Excited states of compound **3** (*AEA*) calculated by SAC-CI/6-311G(2d) (Si)+D95v(C,H).

Num.	Sym.[a]	ΔE $(10^3 \times cm^{-1})$	f	Character[b]
AEA-1 (C$_1$)				
1	A(B)	37.0	0.778	H − L
2	A(A)	43.4	0.026	H − L+1
3	A(A)	43.6	0.003	H-1 − L
4	A(B)	44.7	0.018	H-2 − L
5	A(A)	47.4	0.007	H-3 − L
6	A(B)	49.4	0.106	H-1 − L+1
7	A(B)	50.1	0.049	H-4 − L
8	A(A)	51.5	0.030	H-2 − L+1
9	A(A)	52.0	0.006	H-1 − L+3
10	A(A)	52.1	0.058	H − L+2
AEA-2 (C$_1$)				
1	A(B)	35.9	0.780	H − L
2	A(A)	43.0	0.015	H − L+1
3	A(B)	43.1	0.007	H-2 − L
4	A(A)	43.4	0.017	H-1 − L
5	A(A)	46.6	0.003	H-3 − L
6	A(B)	48.9	0.039	H-4 − L
7	A(A)	49.5	0.067	H − L+2
8	A(A)	50.9	0.033	H-2 − L+1
9	A(B)	51.5	0.010	H − L+3
10	A(B)	52.3	0.083	H-1 − L+1
AEA-3 (C$_2$)				
1	B	36.9	0.794	H − L
2	A	41.7	0.011	H − L+1
3	A	43.6	0.012	H-1 − L
4	B	44.0	0.010	H-2 − L
5	A	47.0	0.008	H-3 − L
6	B	48.5	0.217	H-1 − L+1
7	A	49.2	0.032	H-2 − L+1
8	B	49.5	0.027	H-4 − L
9	B	50.4	0.021	H − L+3
10	A	50.8	0.000	H − L+2
AEA-4 (C$_2$)				
1	B	37.4	0.786	H − L
2	A	41.8	0.028	H − L+1
3	A	43.6	0.013	H-1 − L
4	B	44.6	0.013	H-2 − L
5	A	47.2	0.029	H-3 − L
6	B	48.6	0.192	H-1 − L+1
7	A	49.3	0.012	H-2 − L+1
8	B	50.2	0.019	H-4 − L
9	B	51.4	0.013	H − L+3
10	A	51.7	0.001	H − L+2

[a] Corresponding symmetry in C$_2$ is given in the parenthesis for C$_1$ structure.
[b] H and L represent HOMO and LUMO, respectively.

Table 2.S8. Excited states of compound **3** (*AEA*) calculated by PBE0/6-311G(d).

Num.	Sym.	ΔE ($10^3 \times cm^{-1}$)	f	Character[a]
AEA-1 (C$_1$)				
1	A	39.4	0.728	H − L
2	A	43.8	0.002	H − L+1
3	A	44.1	0.020	H-1 − L
4	A	45.0	0.009	H-2 − L
5	A	46.0	0.002	H-3 − L
6	A	47.1	0.090	H − L+2
7	A	47.6	0.007	H-4 − L
AEA-2 (C$_1$)				
1	A	38.7	0.751	H − L
2	A	43.7	0.010	H − L+1
3	A	44.0	0.011	H-1 − L
4	A	44.1	0.010	H-2 − L
5	A	45.8	0.000	H-3 − L
6	A	46.8	0.040	H-4 − L
7	A	47.1	0.031	H − L+2
AEA-3 (C$_2$)				
1	B	39.6	0.745	H − L
2	A	43.4	0.002	H − L+1
3	A	44.3	0.018	H-1 − L
4	B	45.6	0.006	H-2 − L
5	A	46.3	0.000	H-3 − L
6	B	47.1	0.180	H − L+3
7	A	47.6	0.000	H − L+2
AEA-4 (C$_2$)				
1	B	40.0	0.738	H − L
2	A	43.3	0.012	H − L+1
3	A	44.4	0.027	H-1 − L
4	B	45.7	0.009	H-2 − L
5	A	46.7	0.005	H-3 − L
6	B	47.2	0.160	H-1 − L+1
7	B	48.1	0.011	H − L+2

[a] H and L represent HOMO and LUMO, respectively.

Table 2.S9. Transition moments and oscillator strengths of **1-3** calculated by SAC-CI.

	ΔE (10³ X cm⁻¹)	transition moment (au)			f
		x	y	z	
SAS-2	41.5	-1.13	0.39	-0.11	0.18
(C$_i$)	42.1	-1.11	0.57	0.09	0.20
	44.8	-0.97	-0.41	-0.06	0.15
	45.6	0.00	0.00	0.00	0.00
	46.6	-0.21	-0.16	-0.03	0.01
	46.7	0.00	0.00	0.00	0.00
	48.3	0.00	0.00	0.00	0.00
AAS	37.4	-2.31	0.07	-0.13	0.61
	41.5	-0.41	0.18	-0.06	0.03
	44.2	-0.32	-0.08	0.22	0.02
	45.7	-0.35	-0.16	0.17	0.02
	47.4	0.29	0.08	-0.30	0.03
	47.7	-0.09	-0.03	0.14	0.00
	48.9	0.09	-0.16	-0.12	0.01
AEA-3	36.9	-0.22	2.65	0.00	0.79
(C$_2$)	41.7	0.00	0.00	0.29	0.01
	43.6	0.00	0.00	-0.30	0.01
	44.0	-0.25	0.11	0.00	0.01
	47.0	0.00	0.00	-0.24	0.01
	48.5	0.11	-1.21	0.00	0.22
	49.2	0.00	0.00	0.46	0.03

Axis

SAS-2
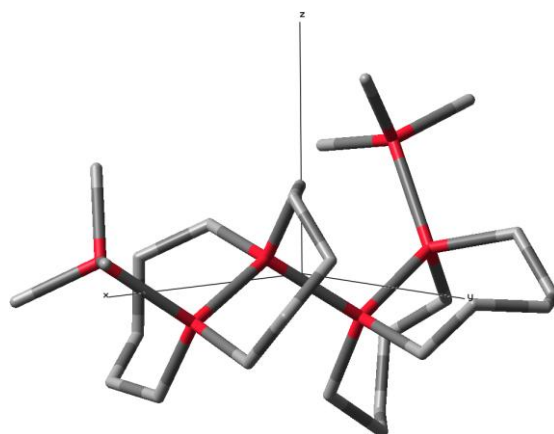
AAS
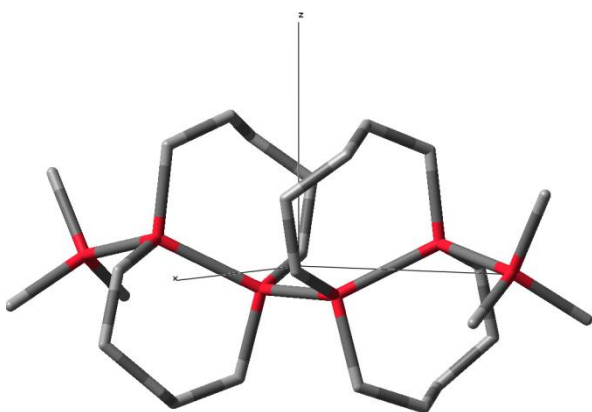
AEA-3

1 (*SAS*)

a) UV-Vis
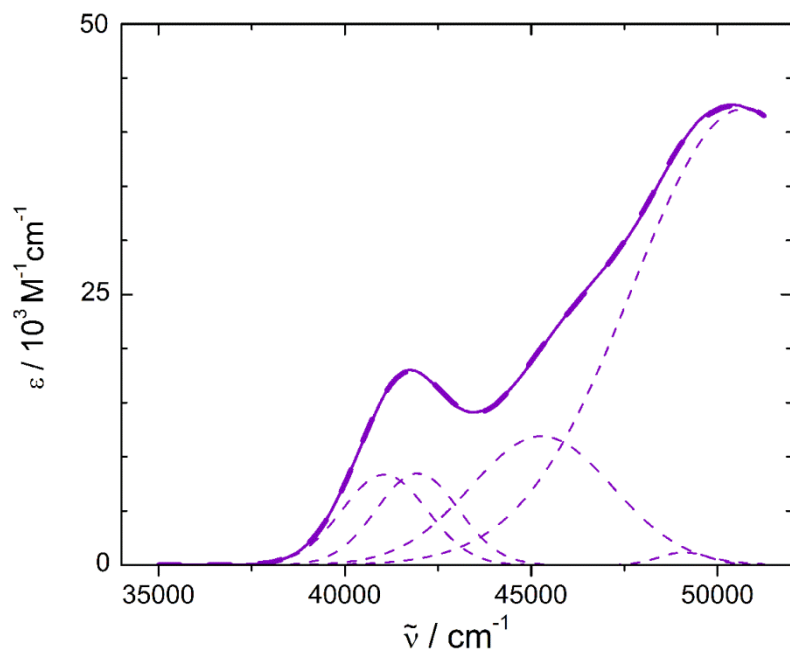
b) LD$_r$
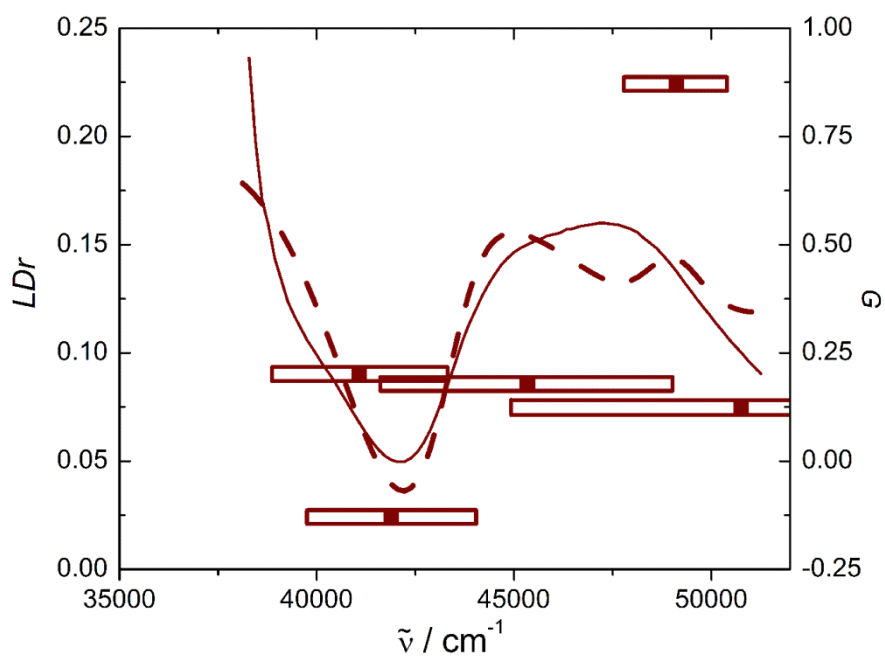
c) MCD
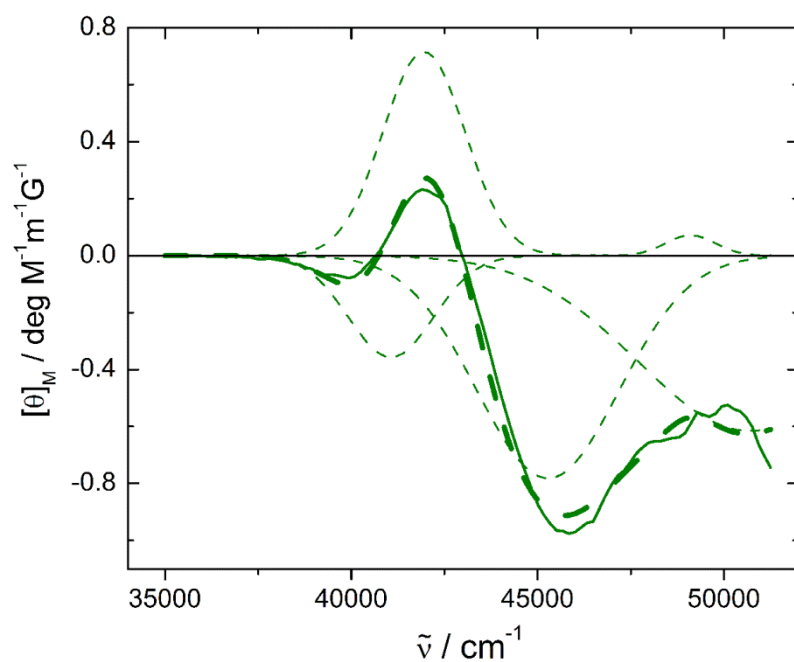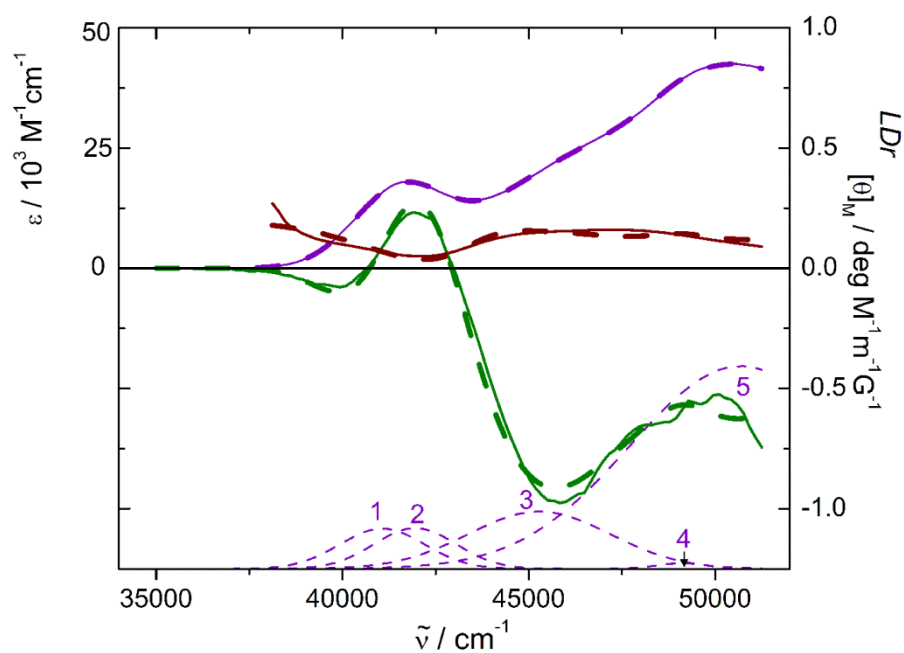
d) UV-Vis, LD_r, MCD

Figure 2.S1. (a) UV-Vis, (b) LD_r, (c) MCD, and (d) UV-Vis, LD_r, and MCD spectra of **1** (*SAS*). In (a)-(d), UV-Vis, LD_r and MCD spectra are shown in solid violet, red, and olive lines, respectively, and fitted UV-Vis, LD_r and MCD are in dashed lines along with the individual Gaussian contributions. In (b), contributions *G* of individual Gaussians are in boxes with red centers.

2 (*AAS*)

a) UV-Vis
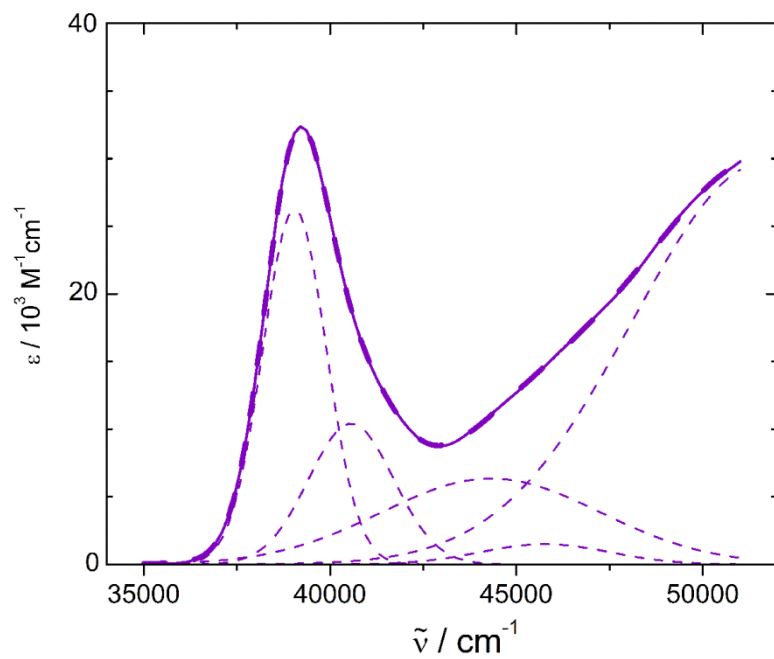
b) LD$_r$
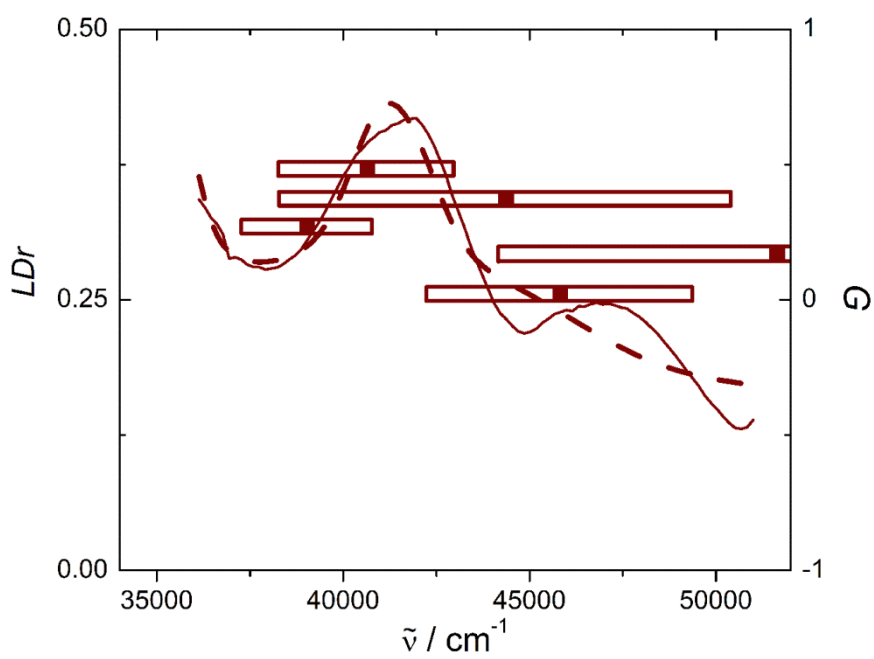
c) MCD
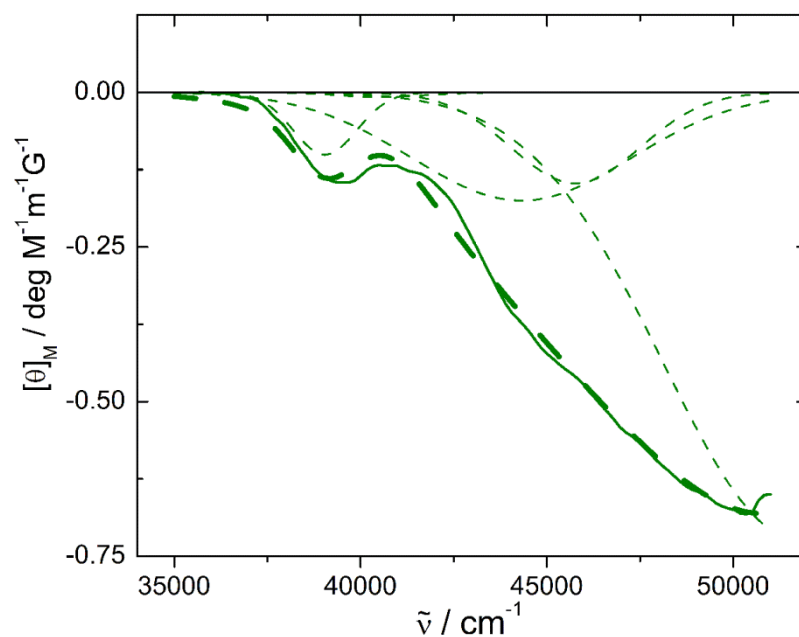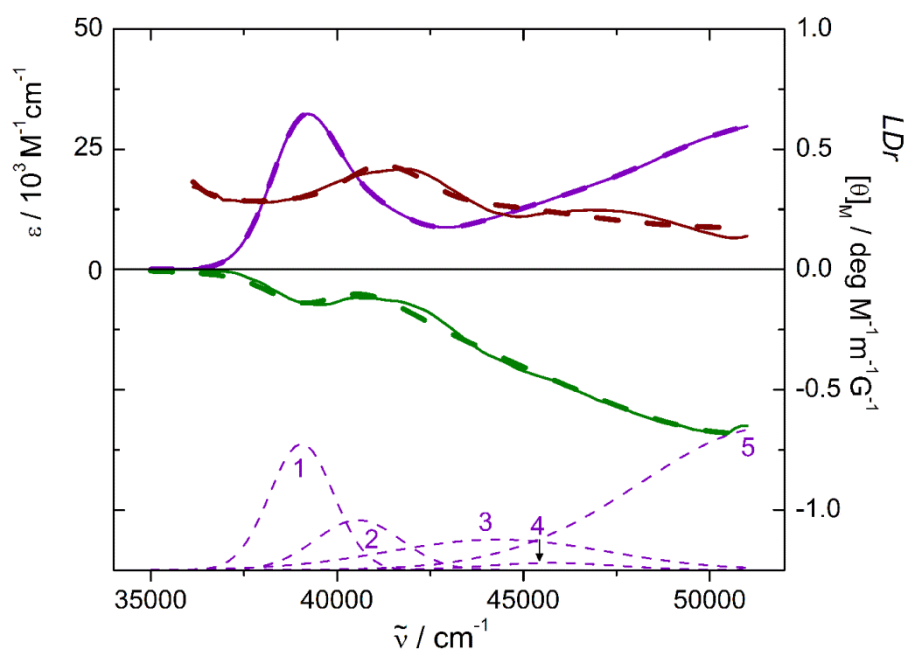
d) UV-Vis, LD_r, MCD

Figure 2.S2. (a) UV-Vis, (b) LD$_r$, (c) MCD, and (d) UV-Vis, LD$_r$, and MCD spectra of **2** (*AAS*). In (a)-(d), UV-Vis, LD$_r$ and MCD spectra are shown in solid violet, red, and olive lines, respectively, and fitted UV-Vis, LD$_r$ and MCD are in dashed lines along with the individual Gaussian contributions. In (b), contributions G of individual Gaussians are in boxes with red centers.

3 (*AEA*)

a) UV-Vis
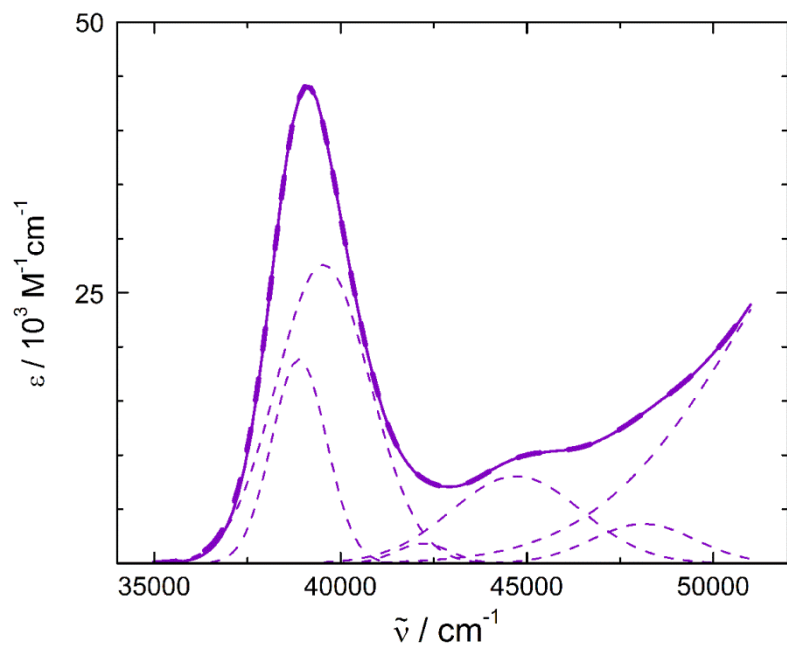
b) LD$_r$
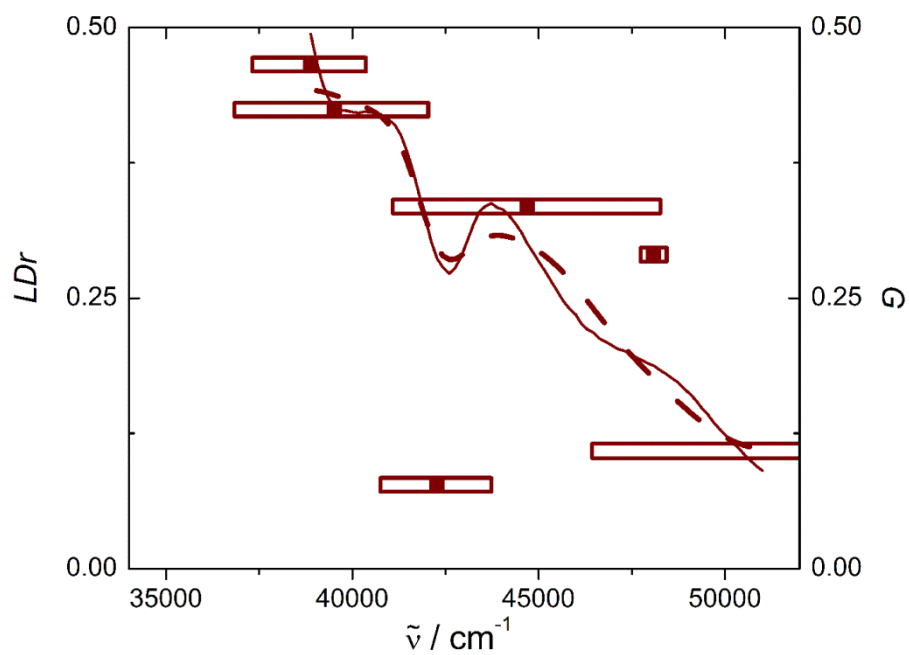
c) MCD
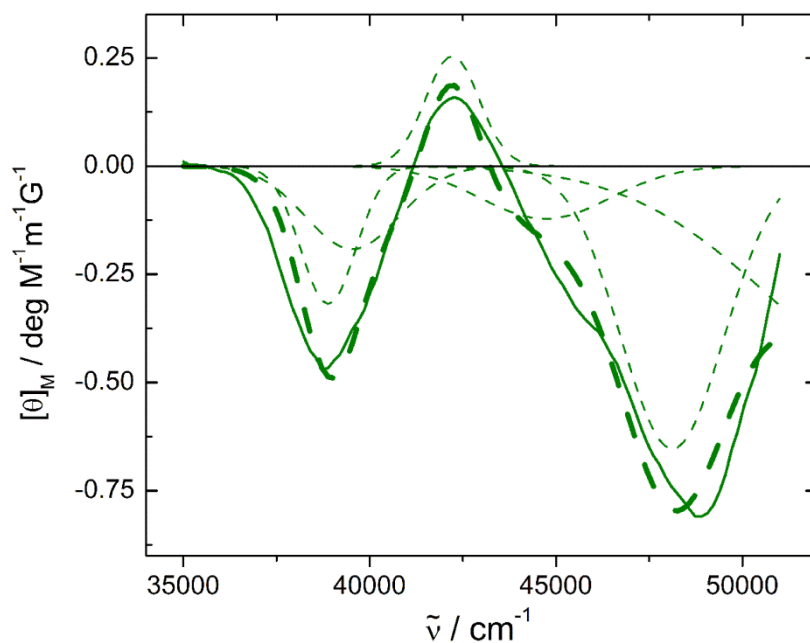
d) UV-Vis, LD$_r$, MCD
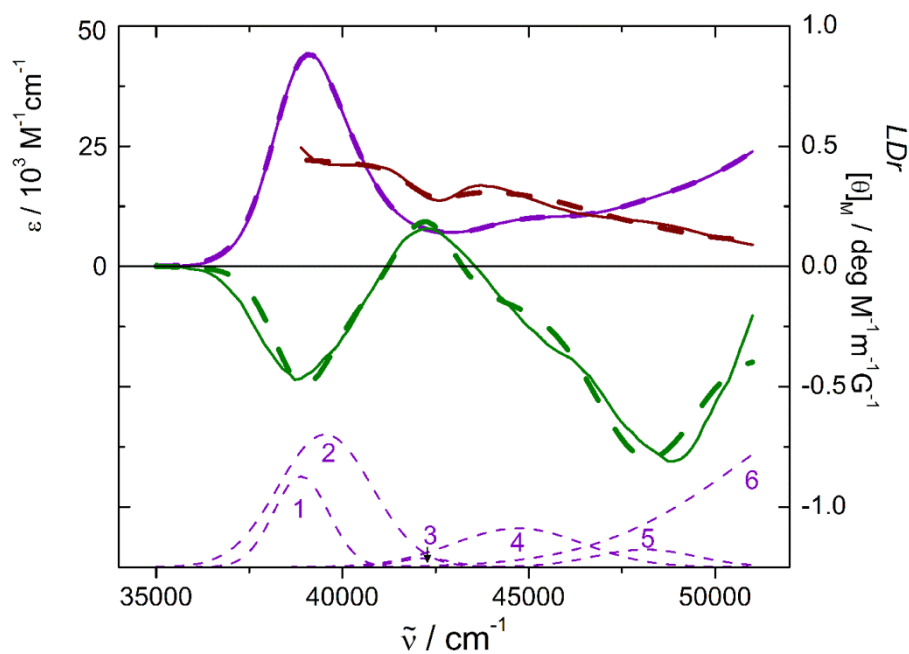
Figure 2.S3. (a) UV-Vis, (b) LD$_r$, (c) MCD, and (d) UV-Vis, LD$_r$, and MCD spectra of **3** (*AEA*). In (a)-(d), UV-Vis, LD$_r$ and MCD spectra are shown in solid violet, red, and olive lines, respectively, and fitted UV-Vis, LD$_r$ and MCD are in dashed lines along with the individual Gaussian contributions. In (b), contributions *G* of individual Gaussians are in boxes with red centers.
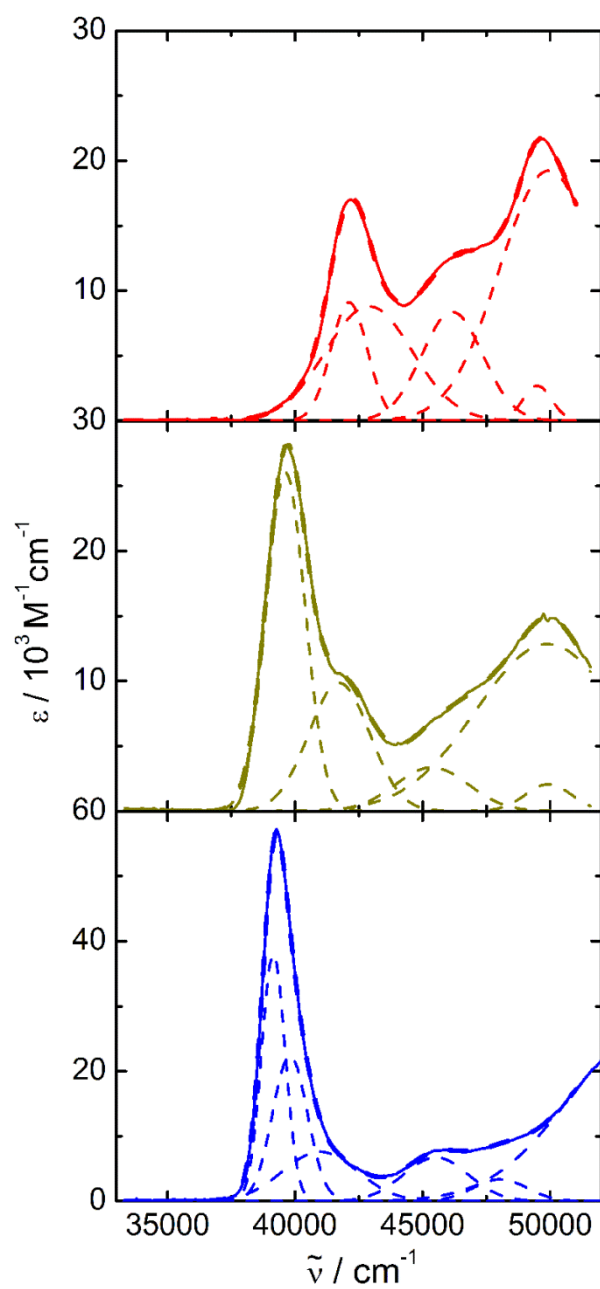
Figure 2.S4. UV-Vis of **1** (top), **2** (center), and **3** (bottom) in 3-MP at 77 K (solid lines) and their Gaussian fit (dashed lines, along with the individual Gaussian contributions).

a) 1 (*SAS*)
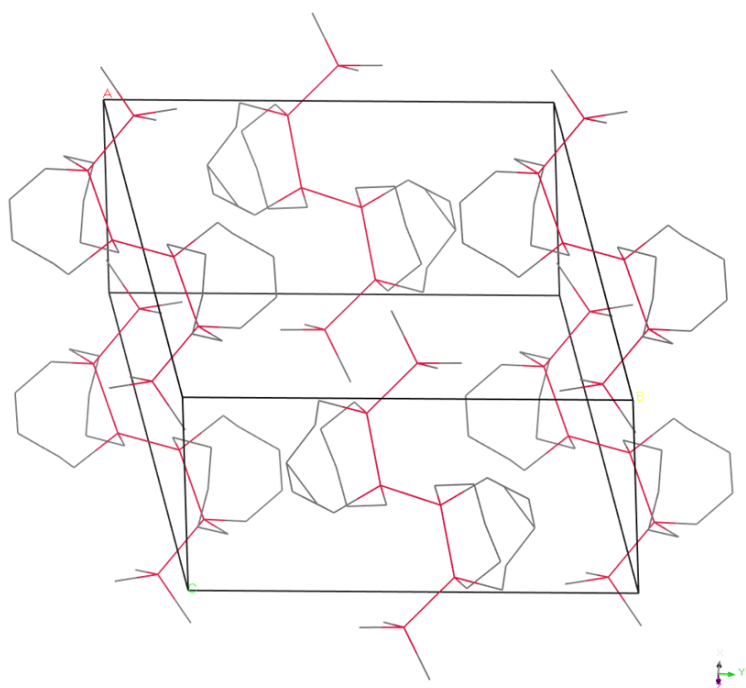
b) 3 (*AEA*)
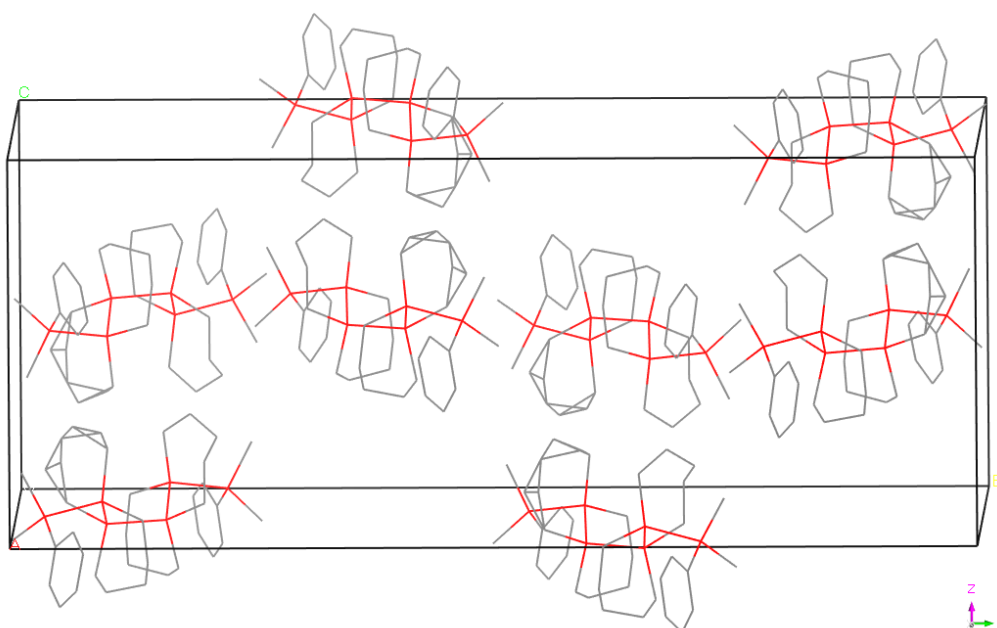
Figure 2.S5. X-ray crystal structures of (a) **1** (*SAS*) and (b) **3** (*AEA*). Si backbone bonds are shown in red. In **1** (*SAS*), two structures with the terminal dihedral angle $\omega=13°$ and $30°$ exist (Ref. 53). In **3** (*AEA*), structure is originally with phenyl group at terminal, which is replaced with methyl in the optimization.

a) 1 (*SAS*)
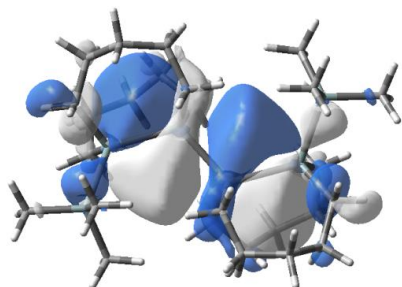
LUMO (σ*)
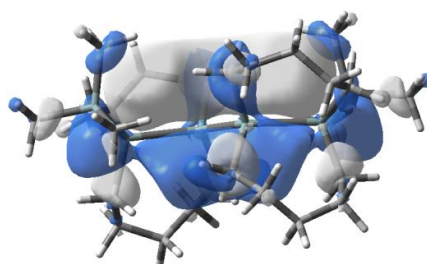
LUMO+1 (π*)

HOMO (σ₁)

HOMO−1 (σ₂)

b) 2 (*AAS*)

LUMO (σ*)

LUMO+1 (π*)

HOMO (σ₁)

HOMO−1 (σ₂)

48

c) 3 (*AEA*)

LUMO (σ*)

LUMO+1 (π*)

HOMO (σ$_1$)
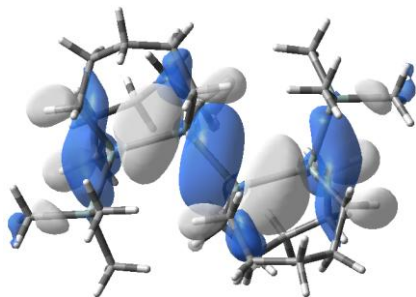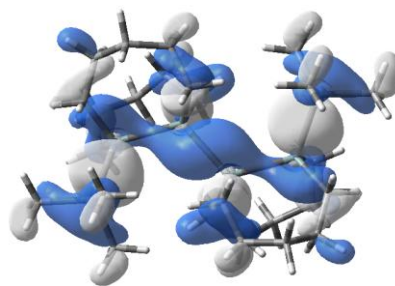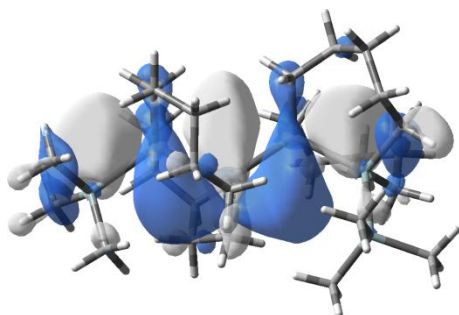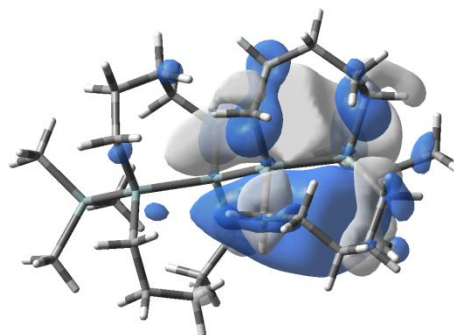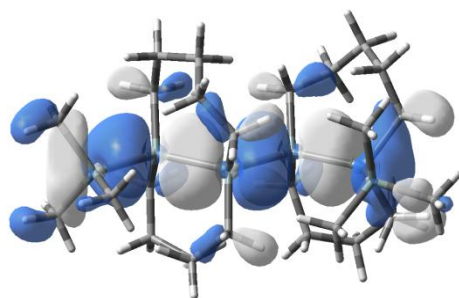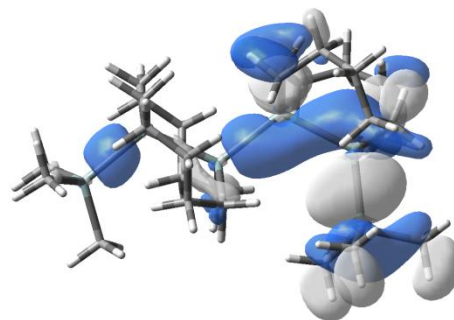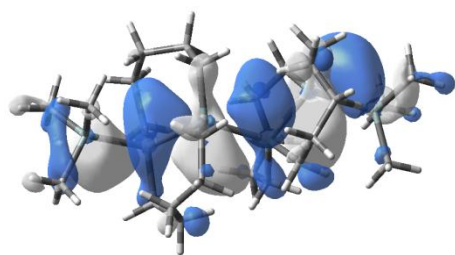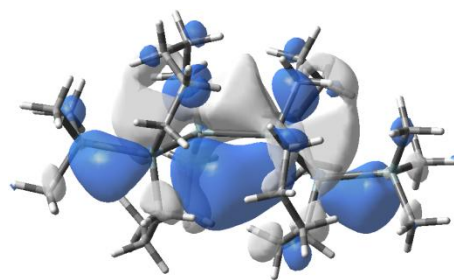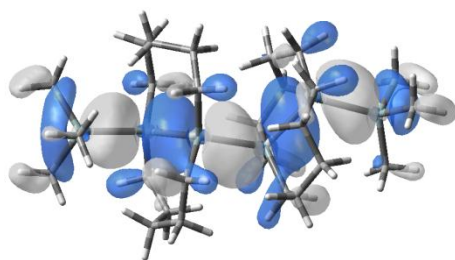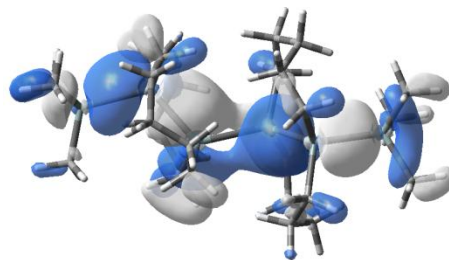
HOMO−1 (σ$_2$)

Figure 2.S6. Frontier MOs (HOMO−1, HOMO, LUMO, LUMO+1) relevant to low-lying transitions of peralkylated hexasilanes (a) **1** (*SAS*-2), (b) **2** (*AAS*), and (c) **3** (*AEA*-3) (isovalue=0.02).

(A) $\omega_1=0°–180°$, $\omega_2=180°$, $\omega_3=0°$
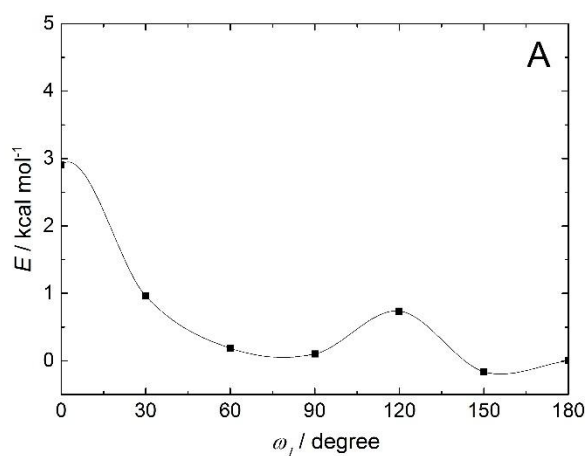
(B) $\omega_1=180°$, $\omega_2=180°$, $\omega_3=0°–180°$
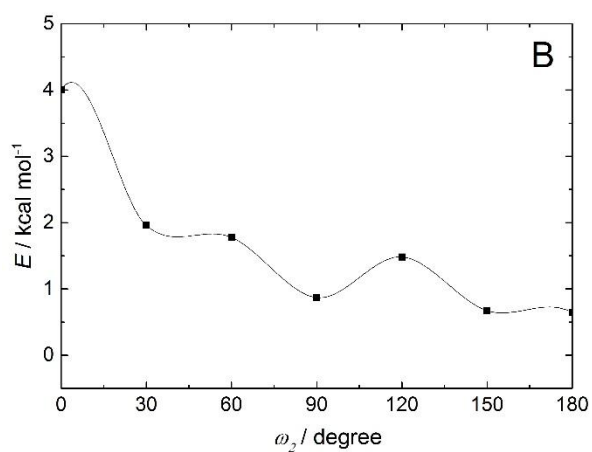
(C) $\omega_1=180°$, $\omega_2=0°–180°$, $\omega_3=180°$
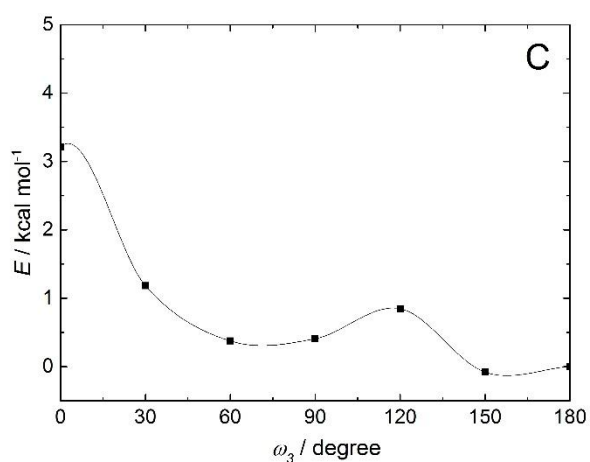
Figure 2.S7. Potential energy curves of n-Si$_6$Me$_{14}$ for (A) $\omega_1=0°–180°$, $\omega_2=180°$, $\omega_3=0°$, (B) $\omega_1=180°$, $\omega_2=180°$, $\omega_3=0°–180°$, and (C) $\omega_1=180°$, $\omega_2=0°–180°$, $\omega_3=180°$.

a) $\omega_1=0°$, $\omega_2=180°$, $\omega_3=0°$ (**SAS**)
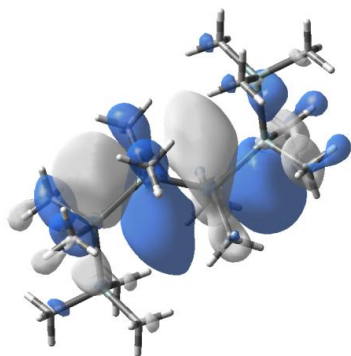
LUMO (σ^*)
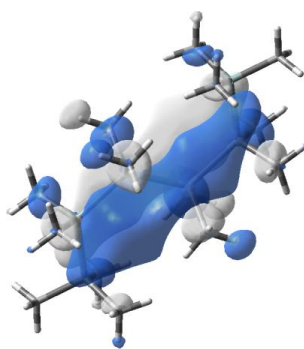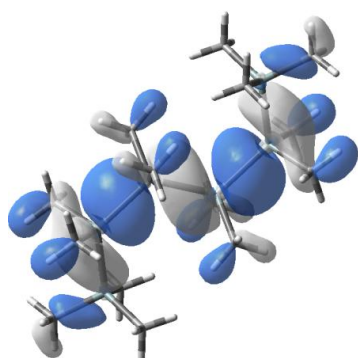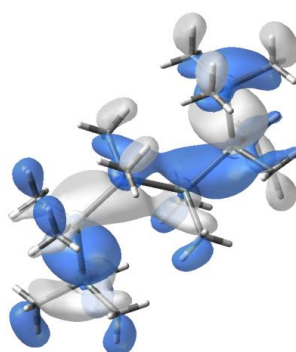
LUMO+1 (π^*)

HOMO (σ_1)

HOMO−1 (σ_2)

b) $\omega_1=90°$, $\omega_2=180°$, $\omega_3=0°$

LUMO (σ^*)

LUMO+1 (π^*)

HOMO (σ_1)

HOMO−1 (σ_2)

c) ω_1=180°, ω_2=180°, ω_3=0° (**AAS**)

LUMO (σ*)

LUMO+1 (π*)

HOMO (σ_1)
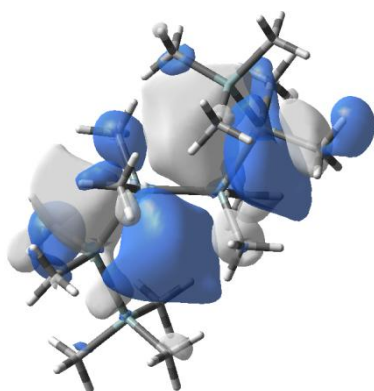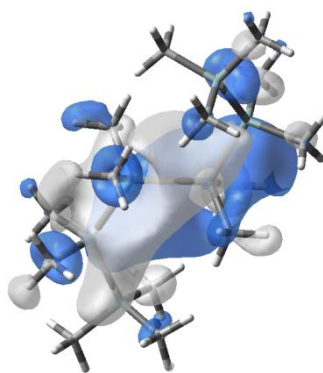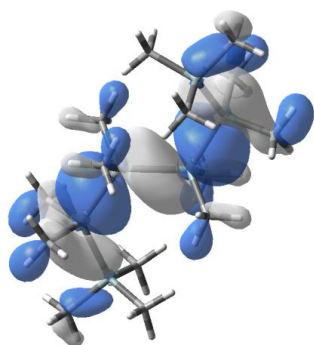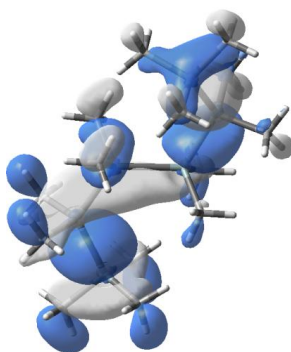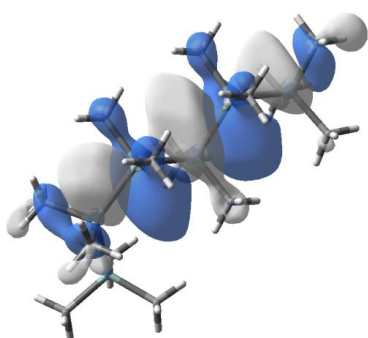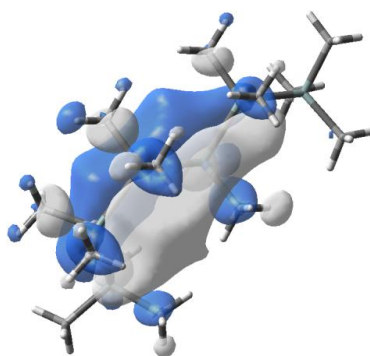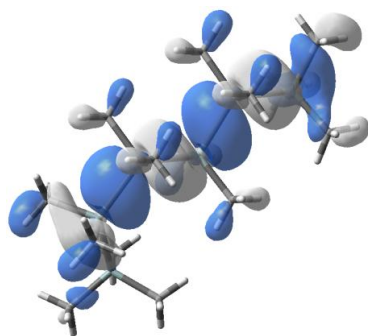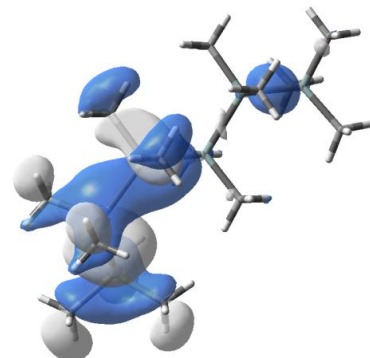
HOMO−1 (σ_2)

Figure 2.S8. Frontier MOs (HOMO−1 − LUMO+1) of n-Si$_6$Me$_{14}$ for ω_1=0° (*SAS*), 90°, 180° (*AAS*) with ω_2=180°, ω_3=0° (isovalue=0.02).

a) $\omega_1=180°$, $\omega_2=180°$, $\omega_3=90°$

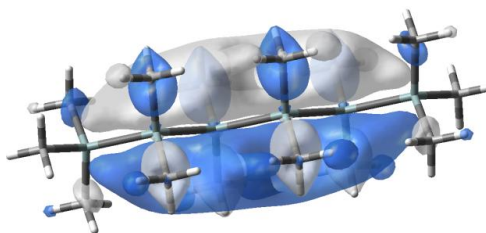
LUMO (σ^*)

LUMO+1 (π^*)

HOMO (σ_1)
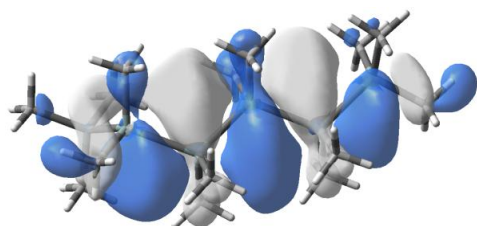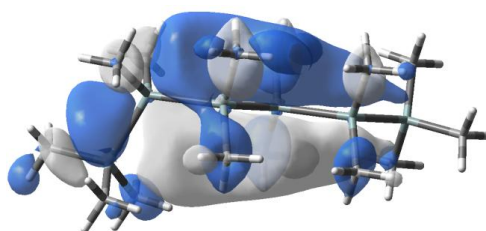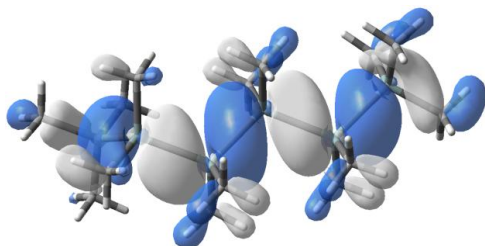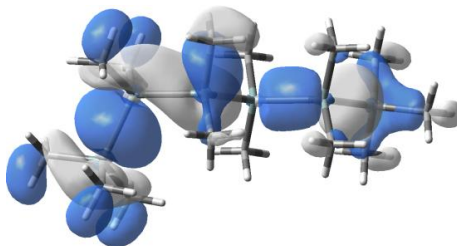
HOMO−1 (σ_2)
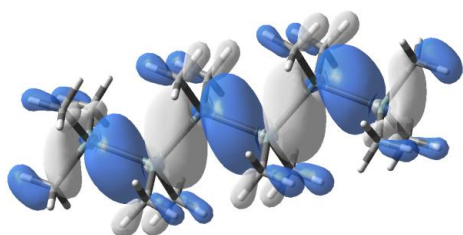
b) $\omega_1=180°$, $\omega_2=180°$, $\omega_3=180°$ (*AAA*)

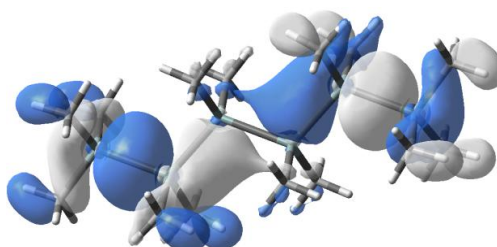
LUMO (σ^*)

LUMO+1 (π^*)

HOMO (σ_1)

HOMO−1 (σ_2)

Figure 2.S9. Frontier MOs (HOMO−1 − LUMO+1) of *n*-Si_6Me_{14} for $\omega_3=90°$, 180° (*AAA*) with $\omega_1=180°$, $\omega_2=180°$ (isovalue=0.02).

a) $\omega_1=180°$, $\omega_2=0°$, $\omega_3=180°$ (**ASA**)

LUMO (σ^*)

LUMO+1 (π^*)

HOMO (σ_1)
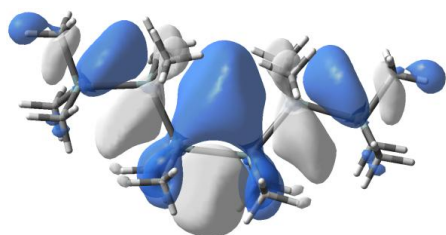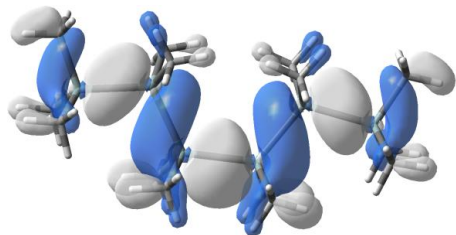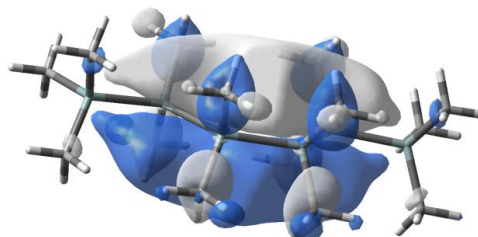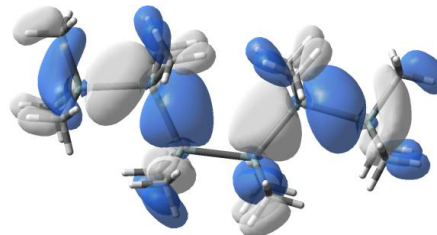
HOMO−1 (σ_2)

b) $\omega_1=180°$, $\omega_2=90°$, $\omega_3=180°$

LUMO (σ^*)

LUMO+1 (π^*)

HOMO (σ_1)
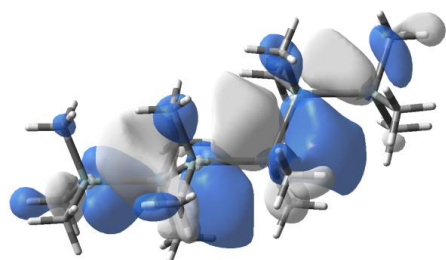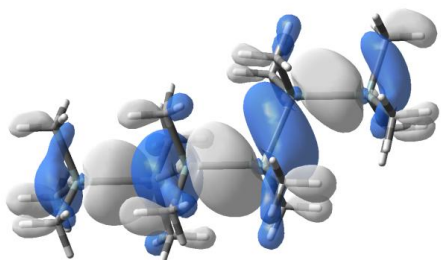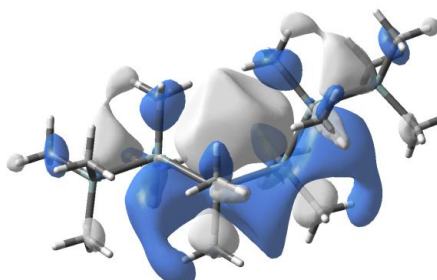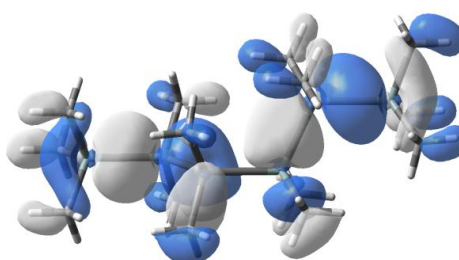
HOMO−1 (σ_2)

Figure 2.S10. Frontier MOs (HOMO−1 − LUMO+1) of n-Si_6Me_{14} for $\omega_2=0°$ (*ASA*), 90° with $\omega_1=180°$, $\omega_3=180°$ (isovalue=0.02).

Chapter 3

Difference in Excited-State Structure Relaxation of Peralkylated *n*-Oligosilanes along Silicon Chain Length

Abstract

The drastic change of the Stokes shift was observed in *n*-peralkylated oligosilanes with respect to its silicon chain length. In this work, the author investigated the mechanism of this variation for *n*-peralkylated oligosilanes, $n\text{-Si}_n\text{Me}_{2n+2}$ (n=4-8), by using the DFT calculations focusing on the excited-state geometry relaxation. In oligosilanes with short silicon chain (n=4, 5, and 6), the excitation is relatively localized at one or two Si-Si bonds and the molecular structure is asymmetrically deformed with the result that the emission occurs in longer wavelength. For those with longer silicon chain (n=7, 8), on the other hand, the excitation is delocalized over the molecule and the Stokes shift is relatively small and the emission occurs from charge reorganization state. To understand this feature, the author also studied the structurally restricted bridged pentasilane which was previously synthesized and found that the structure relaxation in the S_1 state is not localized and therefore, the Stokes shift is small.

Keywords: peralkylated *n*-oligosilane; excited-state geometry; Stokes shift; TD-DFT

3.1. Introduction

Polysilanes and oligosilanes compounds show characteristic photophysical properties due to the delocalization of σ electrons, which is more complicated than well-known delocalization of π electrons. The σ-delocalized systems generally have high conformational flexibility, and owing to this feature, the various optical properties of these systems can be controlled by molecular design. However, the guideline for using this feature has not been fully analyzed and proposed so far, in particular for the emission property.

The characteristic photophysical and electronic properties of these polysilanes and oligosilanes possessing a singly bonded chain with lateral substituents, have been extensively studied (e.g., UV absorption,[1-9] luminescence,[5-8, 10] non-linear polarizability,[11, 12] and photoconductivity[13]) and reviewed.[14-21] However, the understanding of σ delocalization in simple terms is still limited because of its strong conformational dependence, which is observed in the thermochromism[22-26] of oligosilanes.[27] The flexible unconstrained permethylated polysilanes usually have three favorable SiSiSiSi dihedral angles in their Si lain, *transoid* (165°), *gauche* (55°), and *ortho* (90°).[21, 28-30] It is generally known that among these conformations, the thermodynamically most stable transoid form predominates at low temperatures[31] and typically shows an intense long-wavelength absorption band.[32, 33]

Regarding photoabsorption of oligosilanes, much efforts have been made to clarify the conformational effects with respect to various Si-Si chain lengths. For example, the theoretical understanding of *n*-tetrasilanes, the shortest chains that exhibit conformational isomerism, has been well advanced. There are various computational studies reported for the ladder C and H models,[34-37] conformational analysis,[28, 29, 38-42] and excited states of the *n*-tetrasilanes Si_4H_{10}[43-45] and *n*-Si_4Me_{10},[9, 34, 46-48] and for longer chains.[33] Experimental studies have also been reported for matrix isolation of *n*-Si_4Me_{10} conformers,[46, 49] conformational control by cyclic carbosilanes,[6, 8, 49-52] bicyclic disilanes,[32, 52-56] bicyclic trisilanes,[57, 58] and bulky lateral substituents,[59] hypervalent silicons,[60-63] helicity introduction by chiral terminal[64-66] or lateral[67, 68] substituents, and inclusion into cyclodextrin and other hosts.[69-74]

The relationship between photoabsorptions and Si backbone conformational effects in the Si chains has been investigated in detail experimentally and theoretically for peralkylated *n*-tetrasilanes and *n*-hexasilanes. In particular, conformationally controlled *n*-hexasilanes with lateral bulky substituents where SiSiSiSi dihedral angles are controlled have been synthesized and their photophysical properties have been investigated. Previously, detailed theoretical analysis of the UV, MCD, and LDr spectra of peralkylated *n*-tetrasilanes[9] and *n*-hexasilanes[75] has been carried out. The longer chain in *n*-hexasilanes revealed richer effects of σ delocalization on electronic excitation because of the combination of three variable dihedral angles.[75]

n-Peralkylated oligosilanes show different emission spectra with respect to their Si chain length due to the variation of σ delocalization. In particular, Stokes shift of *n*-peralkylated oligosilanes shows significant change with Si chain length. The UV absorption and emission spectra of *n*-Si$_n$Me$_{2n+2}$ (n=2–8, 10, 16) observed previously are compared in Figure 3.1.[76-78] For oligosilanes with the Si chain length is long enough (n≧7), the absorption and emission spectra show small Stokes shifts. On the other side, for those with short Si chain (n≦6), they show significantly large Stokes shifts as seen in Figure 3.1 and in particular, their emission spectra show broad peak. It is anticipated that this behavior of the emission spectra is related to be the unique structure relaxation and conformational change in the excited state. Based on this assumption, the structurally restricted pentasilane which has *anti*-conformation shown in Figure 3.2 was previously synthesized and its photophysical properties were observed.[57]
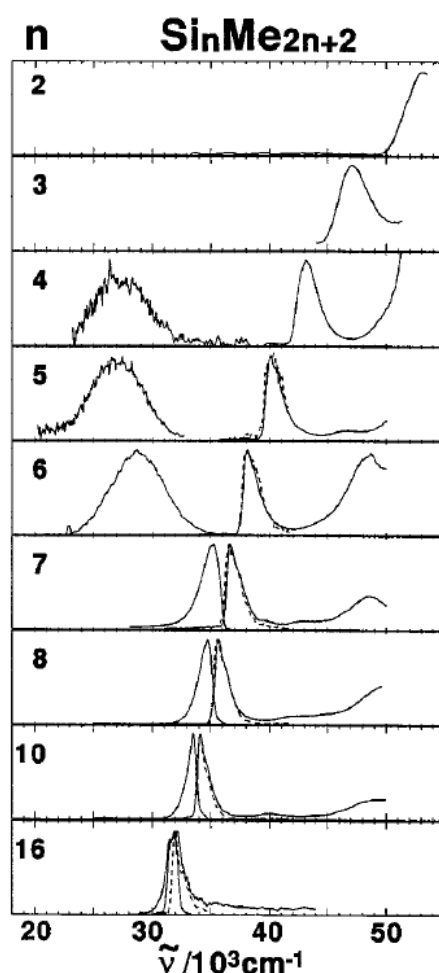
Figure 3.1. Emission, absorption, and excitation (dashed) spectra of *n*-peralkylated oligosilanes (Si$_n$Me$_{2n+2}$, n=2-8, 10, 16) cited from Ref. [78]. At 77 K in isopentane /cyclopentane (7 / 3, v / v), except for Si$_2$Me$_6$ (~10 K, in the Ar matrix[77]), Si$_4$Me$_{10}$ (17 K, neat), Si$_5$Me$_{12}$ (30 K), Si$_6$Me$_{14}$ (30 K), and Si$_{16}$Me$_{34}$ (3-methylpentane[76]). The peak maxima were normalized to unity.

In this work, the author investigated the geometrical and electronic structures of *n*-peralkylated oligosilanes *n*-Si$_n$Me$_{2n+2}$ (n=4-8) and the structurally restricted *n*-pentasilane by the DFT and TD-DFT calculations. In particular, the author examined the structure relaxation in the first excited state (S$_1$ state) of these oligosilanes and inspect the origin of the unique variation of the Stokes shift with respect to the Si chain length observed in *n*-peralkylated oligosilanes.

3.2. Computational details

The ground states of *n*-Si$_n$Me$_{2n+2}$ (n=4-8) were optimized by the DFT calculations with TPSSH functional. The basis sets were 6-31G(d) for Si and 6-31G for C and H atoms.[79, 80] The dihedral angles of the Si chain varies as *transoid*, *gauche*, *ortho*, and *anti* conformation with low energy barriers. Based on the previous studies of peralkylated *n*-tetrasilanes[9] and *n*-hexasilanes,[75] the author adopted the initial structures with all-*transoid* conformation, which is most stable, to locate the local minima of these *n*-Si$_n$Me$_{2n+2}$ (n=4-8) in both ground and excited states. The absorption spectra based on these ground-state structures were calculated by TDDFT with the same functional and basis sets.[81] The optimization of the S$_1$ state which is attributed to σ-σ* transition with considerable large oscillator strength was performed by TDDFT calculations with the same functional and basis sets and the emission energies were obtained. Various symmetrical or unsymmetrical initial structures were examined in the geometry optimization of the S$_1$ state. The accuracy of TDDFT calculations was benchmarked in various systems[82, 83] including peralkylated *n*-tetrasilane and *n*-hexasilane.[9, 75]

Regarding the structurally restricted peralkylated *n*-pentasilane, compound **1**, as shown in Figure 3.2, the initial structure was generated from the X-ray crystal structure of Ph$_2$Si$_5$Me$_6$((CH$_2$)$_4$)$_2$.[57] The geometry optimizations of the ground and exited states were performed in the same manner as in the cases of *n*-Si$_n$Me$_{2n+2}$ (n=4-8). The absorption and emission spectra were calculated by TDDFT with the same functional and basis sets.

All the DFT and TDDFT calculations including geometry optimization were performed by using Gaussian16 program ver. A01.[84]
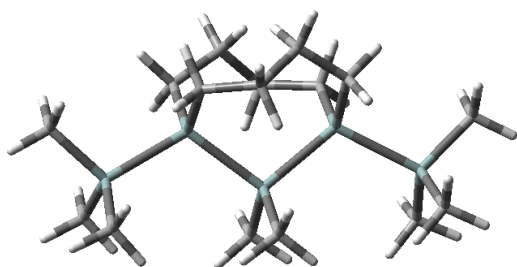
(a) structurally restricted *n*-pentasilane **1**
(compound **1**)
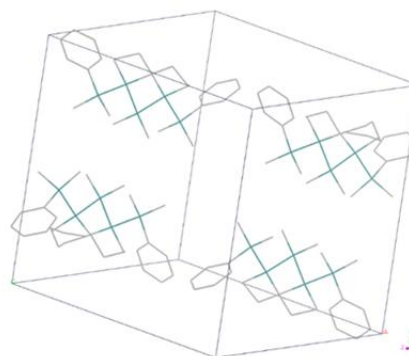
(b) X-ray structure of Ph$_2$Si$_5$Me$_6$((CH$_2$)$_4$)$_2$

Figure 3.2. (a) Structurally restricted *n*-pentasilane **1** and (b) X-ray structure of Ph$_2$Si$_5$Me$_6$((CH$_2$)$_4$)$_2$[57] used for generating the initial structure of geometry optimization of **1**.

3.3. Results and Discussion

A. Absorption and emission spectra of *n*-Si$_n$Me$_{2n+2}$ (n=4-8)

The calculated geometrical parameters of the S$_0$ and S$_1$ states of *n*-Si$_n$Me$_{2n+2}$ (n=5, 6, 7) and compound **1** are presented in Figure 3.3. The parameters of other molecules (n=4, 8) are compiled in Figure 3.S1. The calculated absorption and emission peaks of σ-σ* transition of all the *n*-Si$_n$Me$_{2n+2}$ (n=4-8) are compared in Figure 3.4 and Table 3.1. The highest occupied molecular orbitals (HOMO) and lowest unoccupied molecular orbitals (LUMO) that are relevant to the transition with considerable oscillator strength are shown in Figure 3.S2.
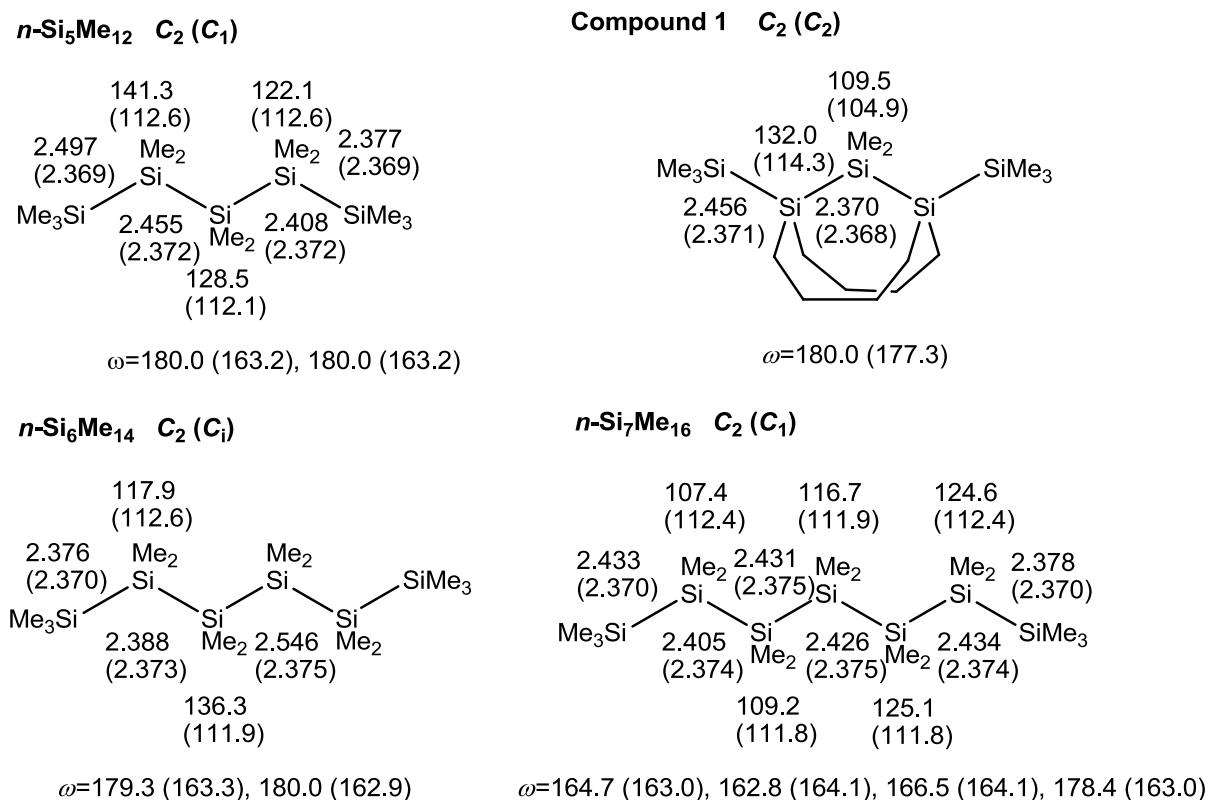
Figure 3.3. Geometrical parameters of *n*-Si$_n$Me$_{2n+2}$ (n=5, 6, 7) and compound **1** optimized by DFT and TDDFT calculations with TPSSH functional and the basis sets of 6-31G(d) for Si and 6-31G for C and H. Point group of the excited-state (ground-state) geometry is given. Excited-state geometrical parameters are shown with ground-state ones in the parenthesis. Si-Si bond distances are given in Å and valence and dihedral angles are in degree.
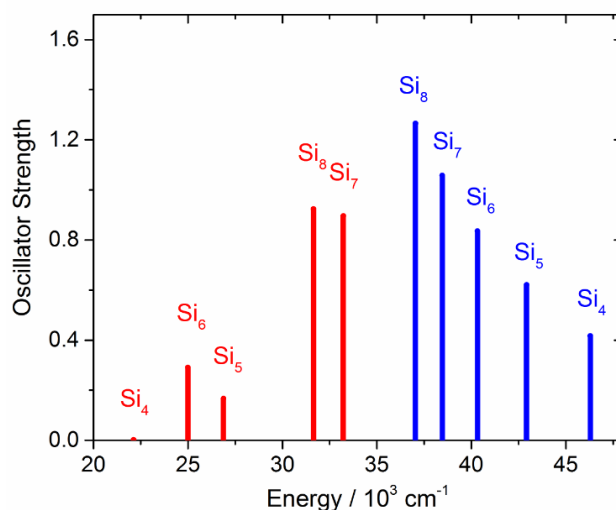
Figure 3.4. Calculated absorption peak (blue) and emission peak (red) of n-Si_nMe_{2n+2} (n=4-8)

Table 3.1. Calculated absorption (λ_{abs}) and emission (λ_{em}) wavelength (nm) of n-Si_nMe_{2n+2} (n=4-8) compared with experimental values.

	Expt.[a]	Theory		Expt.[a]	Theory	
	λ_{abs}	λ_{abs}	f	λ_{em}	λ_{em}	f
Si_4Me_{10}	232	216	0.416	377	452	0.002
Si_5Me_{12}	250	233	0.620	364	372	0.166
Si_6Me_{14}	260	248	0.835	344	400	0.290
Si_7Me_{16}	270	260	1.057	285	301	0.896
Si_8Me_{18}	281	270	1.265	290	316	0.924

[a] References [76-78]

The global minima of the ground-state structures of n-peralkylated oligosilenes, n-Si_nMe_{2n+2} (n=4-8), studied here belong to C_2 symmetry as shown in Figures 3.3 and 3.S1. The calculated Si-Si bond lengths in the S_0 state range 2.369–2.374 Å. For simplicity, only the structures in all-*transoid* conformation with calculated dihedral angles are ~163° are considered; other conformations are also possible at room temperature. The absorption spectra of these compounds were calculated at the optimized S_0 state geometry. The lowest excited state (S_1) in *B* symmetry which is assigned to σσ* transition has a considerable oscillator strength except for Si_4Me_{10} for which the second excited state is σσ* transition. This strong absorption peak compared in Figure 3.4 shows monotonic red shift along the elongation of Si chain due to the σ conjugation as observed in UV absorption spectra (Figure 3.1). The calculated values show fair agreement with the experimental values; the deviation from the experimental values are less than 15 nm; the overestimation of the absorption energy by TD-DFT calculations is less than 0.3 eV.

The trend of the structure relaxation due to excitation is different between n=4-6 and n=7,

8. Generally, the Si-Si bonds are elongated and valence angles become larger in the S_1 state as seen in Figures 3.3 and 3.S1. The molecular structures of n=4-6 in the S_1 state are nearly planar. The structures of tetrasilane and pentasilene are significantly deformed and non-symmetric, while the structure of hexasilane belongs to C_i symmetry. For n=7 and 8, the molecular structures in the S_1 state are also non-symmetric and many Si-Si bonds are elongated by 0.06 Å and 0.04 Å, respectively, except for one terminal bond. The symmetric structures of n=7 and n=8 are first-order transition state with one mode of imaginary vibrational frequency. Two valence angles at one terminal bond become large as ~125° and the dihedral angle at this terminal are 175-178°, while other valence angles and dihedral angles does not change significantly from the ground state *transoid* conformation (ω=164°).

For the compounds with short Si chain length (n=4-6), the calculated emission energy show very low as 2.78, 3.34, 3.10 eV (452, 372, and 400 nm), which are fair agreement with the experimental values as 377, 364, and 344 nm, respectively. This is due to the large structure relaxation in the S_1 state as mentioned above. The excitation is relatively localized at central region for these species: as seen in the variation of Si-Si bond length, only the central Si-Si bond is elongated as 2.62 or 2.63 Å from the ground-state bond length of 2.38 or 2.39 Å. This bond elongation at central Si-Si bond can be understood by the HOMO-LUMO transition which are characterized by the in-phase to anti-phase transition at this bond. Because of this localization of excitation in these compounds (n=4-6), the large Stokes shift was observed. The HOMO and LUMO are also shown at the S_1 state geometries in Figure 3.S2. The HOMO is localized at specific Si-Si bond for n=4-6, which also indicates the localization of excitation.

For n-Si$_n$Me$_{2n+2}$ (n=7 and 8), on the other hand, the geometrical relaxation in the S_1 state is delocalized over the entire molecule, in particular, for the Si-Si bond length as noted above. The calculated absorption and emission wavelength of n-Si$_8$Me$_{10}$ are 270 and 316 nm which agree well with the experimental values of 281 and 290 nm, respectively. Accordingly, the calculated Stokes shift of these two n-oligosilanes (n=7, 8) were calculated as small as ~0.3 eV compared to the experimental value of ~0.14 eV. As seen in the HOMO and LUMO at the S_1 state geometry in Figure 3.S2, the character at the S_1 state geometry is charge reorganization over the entire molecule for both n=7 and 8, which is different from n=4-6.

B. Structurally restricted pentasilane

In order to look into the structure relaxation and the excitation of n-oligosilanes with short Si chain, the structurally restricted peralkylated n-pentasilane, compound **1**, was previously synthesized and its photophysical properties were measured. The UV absorption and emission spectra are shown in Figure 3.5(a) compared with the calculated spectra in Figure 3.5(b). Again the TD-DFT calculations reproduced these spectra well. The structure relaxation in the S_1 state is shown in Figure 3.3. In the ground state, all four Si-Si bond are nearly the same as

61

2.368-2.371 Å, which are slightly shorter than those of peralkylated n-Si$_5$Me$_{12}$. On the other hand, the terminal Si-Si bonds are elongated in the S$_1$ state, which is different from that of n-Si$_5$Me$_{12}$. Due to the structure restriction of two -(CH$_2$)$_4$- bridges, two central Si-Si bonds are not so much affected by σ-σ* transition, while the terminal two Si-Si bonds are elongated. Because of this structure restriction, the emission energy does not significantly shift relative to absorption.
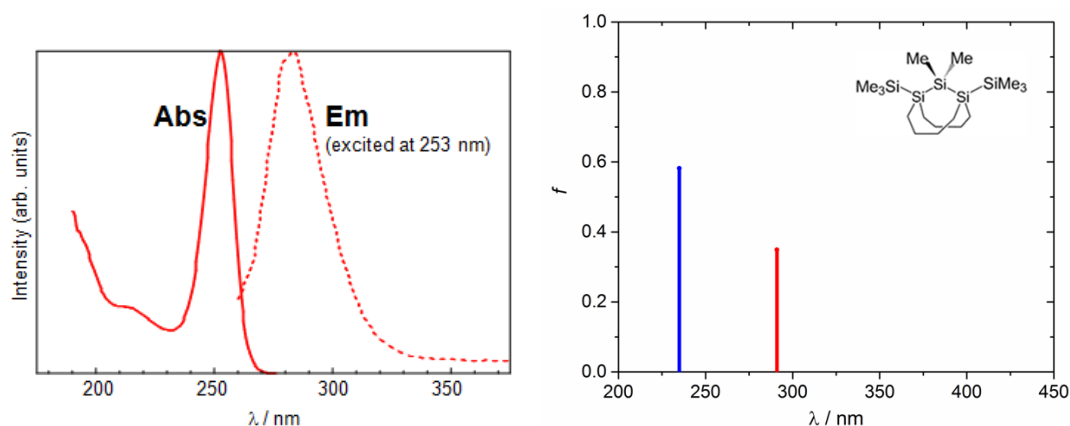
Figure 3.5. (a) Observed and (b) calculated absorption and emission peak of compound **1**.

Next, another stationary point of n-Si$_5$Me$_{12}$ was located by restricting the structure in C_2 symmetry. The results of the absorption and emission spectra are given in Figure 3.6 and the structural parameters are given in Figure 3.S1. In this case, the structural changes in the S$_1$ state are seen in the central two Si-Si bonds and the excitation is delocalized as compared with those in free optimized structure where the structural change is significant only in one Si-Si bond (2.63 Å). Thus, the emission from the structure in C_2 symmetry has the energy of 268 nm whose Stakes shift is relatively small.

Although the structure relaxation of compound **1** in the S$_1$ state is different from that of the structure in C_2 symmetry, the present theoretical and experimental findings revealed that the mechanism of irregular Stokes shift observed in oligosilanes in short Si chain and its drastic change in oligosilanes with longer Si chain.
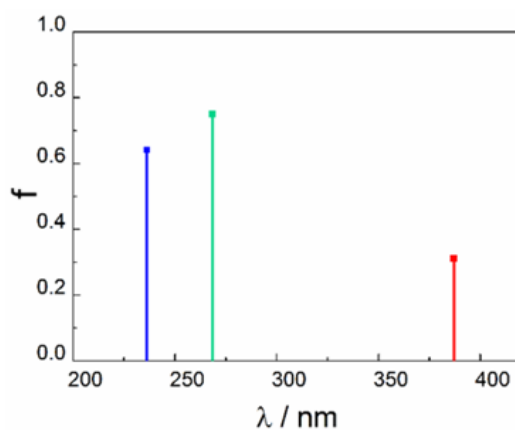
Figure 3.6. Calculated absorption and emission peak of n-Si$_5$Me$_{12}$: absorption (blue), emission from C$_2$ structure (green), and emission from C$_1$ structure (red)

3.4. Summary

The mechanism of the drastic change of Stokes shifts observed in n-peralkylated oligosilanes, n-Si$_n$Me$_{2n+2}$ (n=4-8), with respect to Si chain length has been investigated by the DFT calculations. In short silane chain (n=4-6), the excitation is relatively localized at one or two Si-Si bonds and the emission occurs from the distorted structure. For those with longer silane chain (n=7, 8), the excitation is delocalized and the emission from charge reorganization state occurs. To understand the details of this mechanism, structurally restricted bridged pentasilane, compound **1**, was considered and the calculated Stokes shift was small due to the symmetric structure in the S$_1$ state where the excitation is delocalized.

References

(1)   Gilman, H.; Atwell, W. H.; Schwebke, G. L. *Chem. Ind.* **1964**,   1063.

(2)   Gilman, H.; Atwell, W. H.; Shwebke, G. L. *J. Organomet. Chem.* **1964**, *2*, 369-371.

(3)   Sakurai, H.; Kumada, M. *Bull. Chem. Soc. Jpn.* **1964**, *37*, 1894.

(4)   Hague, D. N.; Prince, R. H. *Chem. Age.* **1964**,   1492.

(5)   Obata, K.; Kira, M. *Organometallics* **1999**, *18*, 2216-2222.

(6)   Fogarty, H. A.; Imhof, R.; Michl, J. *Proc. Natl. Acad. Sci. USA* **2004**, *101*, 10517-10522.

(7)   Raymond, M. K. *Ph.D. Dissertation, University of Colorado, Boulder* **1997**.

(8)   Fogarty, H. A. *Ph.D. Dissertation, University of Colorado, Boulder* **2005**.

(9)   Tsuji, H.; Fogarty, H. A.; Ehara, M.; Fukuda, R.; Casher, D. L.; Tamao, K.; Nakatsuji, H.; Michl, J. *Chem. Eur. J.* **2014**, *20*, 9431-9441.

(10)   Mazières, S.; Raymond, M. K.; Raabe, G.; Prodi, A.; Michl, J. *J. Am. Chem. Soc.* **1997**, *119*, 6682-6683.

(11)   Williams, D. J. *Angew. Chem.* **1984**, *96*, 637-651.

(12)   Kishida, H.; Hasegawa, T.; Iwasa, Y.; Koda, T.; Tokura, Y. *Phys. Rev. Lett.* **1993**, *70*, 3724-3727.

(13)   Kepler, R. G.; Soos, Z. G. In *Primary Photoexcitations in Conjugated Polymers*, Sariciftci, N. S., Ed. World Scientific: Singapore, **1997**; pp 363-383.

(14)   Kumada, M.; Tamao, K. *Adv. Organomet. Chem.* **1968**, *6*, 19-117.

(15)   Miller, R. D.; Michl, J. *Chem. Rev.* **1989**, *89*, 1359-1410.

(16)   Kira, M.; Miyazawa, T. In *The Chemistry of Organic Silicon Compounds Vol.2*, Rappoport, Z.; Apeloig, Y., Eds. Wiley: Chichester, **1998**; p 1311.

(17)   Michl, J.; West, R. In *Silicon Containing Polymers*,   Jones, R. G.; Ando, W.; Chojnowski, J., Eds. Kluwer Academic: Dordrecht (The Netherlands), **2000**; p 499.
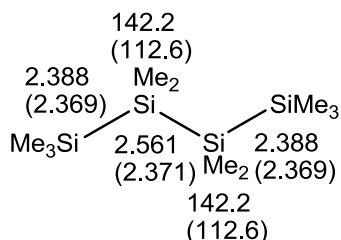
(18) West, R. In *The Chemistry of Organic Silicon Compounds Vol. 3*, Rappoport, Z.; Apeloig, Y., Eds. Wiley: Chichester, **2001**; p 541.

(19) Fogarty, H. A.; Casher, D. L.; Imhof, R.; Schepers, T.; Rooklin, D. W.; Michl, J. *Pure Appl. Chem.* **2003**, *75*, 999-1020.

(20) Tsuji, H.; Michl, J.; Toshimitsu, A.; Tamao, K. *J. Synth. Org. Chem. Jpn.* **2002**, *60*, 762-773.

(21) Tsuji, H.; Michl, J.; Tamao, K. *J. Organomet. Chem.* **2003**, *685*, 9-14.

(22) Harrah, L. A.; Zeigler, J. M. *J. Polym. Sci. Polym. Lett. Ed.* **1985**, *23*, 209-211.

(23) Trefoñas, P.; Damewood, J. R.; West, R.; Miller, R. D. *Organometallics* **1985**, *4*, 1318-1319.

(24) Gahimer, T.; Welch, W. J. *Polymer* **1996**, *37*, 1815-1823.

(25) Sanji, T.; Sakamoto, K.; Sakurai, H.; Ono, K. *Maclomolecules* **1999**, *32*, 3788-3794.

(26) Bukalov, S. S.; Leites, L. A.; West, R. *Maclomolecules* **2001**, *34*, 6003-6004.

(27) Obata, K.; Kira, M. *RIKEN Rev.* **1995**, *11*, 39-40.

(28) Fogarty, H. A.; Ottosson, C. H.; Michl, J. *J. Mol. Struct.* **2000**, *556*, 105-121.

(29) Fogarty, H. A.; Ottosson, C. H.; Michl, J. *J. Mol. Struct.* **2000**, *506*, 243-255.

(30) Michl, J.; West, R. *Acc. Chem. Res.* **2000**, *33*, 821-823.

(31) Fogarty, H. A.; Ottosson, C. H.; Michl, J. *J. Phys. Chem. B* **2006**, *110*, 25485-25495.

(32) Tsuji, H.; Terada, M.; Toshimitsu, A.; Tamao, K. *J. Am. Chem. Soc.* **2003**, *125*, 7486-7487.

(33) Bande, A.; Michl, J. *Chem. Eur. J.* **2009**, *15*, 8504-8517.

(34) Crespo, R.; Piqueras, M. C.; Michl, J. *Theor. Chem. Acc.* **2007**, *118*, 81-87.

(35) Teramae, H.; Michl, J. *Mol. Cryst. Liq. Cryst.* **1994**, *256*, 149-159.

(36) Plitt, H. S.; Downing, J. W.; Raymond, M. K.; Balaji, V.; Michl, J. *J. Chem. Soc. Faraday Trans.* **1994**, *90*, 1653-1662.

(37) Schepers, T.; Michl, J. *J. Phys. Org. Chem.* **2002**, *15*, 490-498.

(38) Neumann, F.; Teramae, H.; Downing, J. W.; Michl, J. *J. Am. Chem. Soc.* **1998**, *120*, 573-582.

(39) Albinsson, B.; Antic, D.; Neumann, F.; Michl, J. *J. Phys. Chem. A* **1999**, *103*, 2184-2196.

(40) Ottosson, C. H.; Michl, J. *J. Phys. Chem. A* **2000**, *104*, 3367-3380.

(41) West, R. *J. Organomet. Chem.* **2003**, *685*, 6-8.

(42) Ohashi, S.; Naruse, Y.; Inagaki, S. *J. Organomet. Chem.* **2003**, *682*, 119-122.

(43) Crespo, R.; Teramae, H.; Antic, D.; Michl, J. *Chem. Phys.* **1999**, *244*, 203-214.

(44) Crespo, R.; Merchan, M.; Michl, J. *J. Phys. Chem. A* **2000**, *104*, 8593-8599.

(45) Piqueras, M. C.; Merchan, M.; Crespo, R.; Michl, J. *J. Phys. Chem. A* **2002**, *106*, 9868-9873.

(46) Albinsson, B.; Teramae, H.; Downing, J. W.; Michl, J. *Chem. Eur. J.* **1996**, *2*, 529-538.

(47) Piqueras, M. C.; Crespo, R.; Michl, J. *J. Phys. Chem. A* **2003**, *107*, 4661-4668.

(48) Rooklin, D. W.; Schepers, T.; Raymond-Johansson, M. K.; Michl, J. *Photochem. Photobiol. Sci.* **2003**, *2*, 511-517.

(49) Plitt, H. S.; Michl, J. *Chem. Phys. Lett.* **1992**, *198*, 400-405.

(50) Imhof, R.; Teramae, H.; Michl, J. *Chem. Phys. Lett.* **1997**, *270*, 500-505.

(51) Imhof, R.; Antic, D.; David, D. E.; Michl, J. *J. Phys. Chem. A* **1997**, *101*, 4579-4586.

(52) Fogarty, H. A.; Tsuji, H.; David, D. E.; Ottosson, C. H.; Michl, J.; Tamao, K.; Ehara, M.; H. Nakatsuji *J. Phys. Chem. A* **2002**, *106*, 2369-2373.

(53) Tamao, K.; Tsuji, H.; Terada, M.; Asahara, M.; Yamaguchi, S.; Toshimitsu, A. *Angew. Chem. Int. Ed.* **2000**, *112*, 3425-3428.

(54) Tsuji, H.; Toshimitsu, A.; Tamao, K.; Michl, J. *J. Phys. Chem. A* **2001**, *105*, 10246-10248.

(55) Seki, S.; Okamoto, K.; Matsuji, Y.; Tagawa, S.; Tsuji, H.; Toshimitsu, A.; K.Tamao *Chem. Phys. Lett.* **2003**, *380*, 141-145.

(56) Mallesha, H.; Tsuji, H.; Tamao, K. *Organometallics* **2004**, *23*, 1639-1642.

(57) Tsuji, H.; Fukazawa, A.; Yamaguchi, S.; Toshimitsu, A.; Tamao, K. *Organometallics* **2004**, *23*, 3375-3377.

(58) Fukazawa, A.; Tsuji, H.; Tamao, K. *J. Am. Chem. Soc.* **2006**, *128*, 6800-6801.

(59) Tanaka, R.; Unno, M.; Matsuoto, H. *Chem. Lett.* **1999**, 595-596.

(60) El-Sayed, I.; Hatanaka, Y.; Muguruma, C.; Shimada, S.; Tanaka, M.; Koga, N.; Mikami, M. *J. Am. Chem. Soc.* **1999**, *121*, 5095-5096.

(61) El-Sayed, I.; Hatanaka, Y.; Onozawa, S.; Tanaka, M. *J. Am. Chem. Soc.* **2001**, *123*, 3597-3598.

(62) Hatanaka, Y. *J. Synth. Org. Chem. Jpn.* **2001**, *59*, 996-1004.

(63) Hatanaka, Y. *J. Organomet. Chem.* **2003**, *685*, 207-217.

(64) Obata, K.; Kabuto, C.; Kira, M. *J. Am. Chem. Soc.* **1997**, *119*, 11345-11346.

(65) Oh, H. S.; Park, L. S.; Kawakami, Y. *Chirality* **2003**, *15*, 646-653.

(66) Sanji, T.; Takase, K.; Sakurai, H. *Bull. Chem. Soc. Jpn.* **2004**, *77*, 1607-1611.

(67) Fujiki, M. *J. Am. Chem. Soc.* **1994**, *116*, 6017-6018.

(68) Fujiki, M. *J. Organomet. Chem.* **2003**, *685*, 15-34.

(69) Okumura, H.; Kawaguchi, A.; Harada, A. *Macromol. Rapid Commun* **2002**, *23*, 781.

(70) Sakamoto, K.; Naruoka, T.; Kira, M. *Chem. Lett.* **2003**, *32*, 380-381.

(71) Sanji, T.; Yoshiwara, A.; Sakurai, H.; Tanaka, M. *Chem. Commun.* **2003**, 1506-1507.

(72) Sanji, T.; Kato, M.; Tanaka, M. *Maclomolecules* **2005**, *38*, 4034-4037.

(73) Sanji, T.; Kato, N.; Tanaka, M. *Chem. Lett.* **2005**, *34*, 1144-1145.

(74) Sanji, T.; Kato, N.; Kato, M.; Tanaka, A. *Angew. Chem.* **2005**, *117*, 7467-7470.

(75) Kanazawa, Y.; Tsuji, H.; Ehara, M.; Fukuda, R.; Casher, D. L.; Tamao, K.; Nakatsuji, H.; Michl, J. *ChemPhysChem* **2016**, *19*, 3010-3022.

(76) Sun, Y.-P.; Hamada, Y.; Huang, L. M.; Maxka, J.; Hsiao, J.-S.; West, R.; Michl, J. *J. Am. Chem. Soc* **1992**, *114*, 6301.

(77) Plitt, H.; Balaji, V.; Michl, J. *Chem. Phys. Lett.* **1993**, *213*, 158.

(78) Raymond, M. K.; Michl, J. *Int. J. Quantum Chem.* **1999**, *72*, 361-367.

(79) Becke, A. D. *J. Chem. Phys.* **1993**, *98*, 5648-5652.

(80) Krishnan, R.; Binkley, J. S.; Seeger, R.; Pople, J. A. *J. Chem. Phys.* **1980**, *72*, 650-654.

(81) Adamo, C.; Barone, V. *J. Chem. Phys.* **1998**, *108*, 664-675.

(82) Bousquet, D.; Fukuda, R.; Maitarad, P.; Jacquemin, D.; Ciofini, I.; Adamo, C.; Ehara, M. *J. Chem. Theory Comput.* **2013**, *9*, 2368−2379.

(83) Bousquet, D.; Fukuda, R.; Jacquemin, D.; Ciofini, I.; Adamo, C.; Ehara, M. *J. Chem. Theory Comput.* **2014**, *10*, 3969−3979.

(84) Frisch, M. J.; Trucks, G. W.; Schlegel, H. B.; Scuseria, G. E.; Robb, M. A.; Cheeseman, J. R.; Scalmani, G.; Barone, V.; Petersson, G. A.; Nakatsuji_et_al, H. *Gaussian 16 Rev. A.03* **2016**.
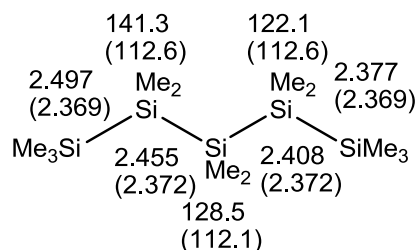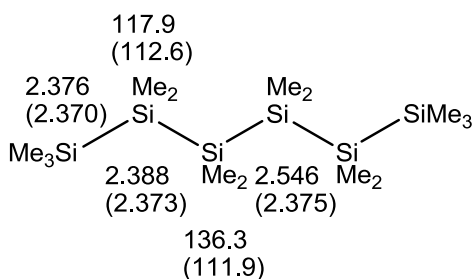
Supporting Information

n-Si₄Me₁₀   C₂ (C₁)

$$n\text{-Si}_4\text{Me}_{10}\quad C_2\ (C_1)$$

142.2
(112.6)
2.388   Me₂
(2.369) Si   SiMe₃
Me₃Si 2.561 Si 2.388
(2.371) Me₂ (2.369)
142.2
(112.6)

ω=179.8 (163.2)

n-Si₅Me₁₂   C₂ (C₁)

141.3   122.1
(112.6)   (112.6)   2.377
2.497   Me₂   Me₂   (2.369)
(2.369) Si   Si
Me₃Si 2.455 Si 2.408 SiMe₃
(2.372) Me₂ (2.372)
128.5
(112.1)

ω=180.0 (163.2), 180.0 (163.2)

n-Si₆Me₁₄   C₂ (Cᵢ)

117.9
(112.6)
2.376   Me₂   Me₂
(2.370) Si   Si   SiMe₃
Me₃Si   Si   Si
2.388 Me₂ 2.546 Me₂
(2.373)   (2.375)
136.3
(111.9)

ω=179.3 (163.3), 180.0 (162.9)

n-Si₇Me₁₆   C₂ (C₁)

107.4   116.7   124.6
(112.4)   (111.9)   (112.4)
2.433   Me₂ 2.431 Me₂   Me₂ 2.378
(2.370) Si (2.375)Si   Si (2.370)
Me₃Si 2.405 Si 2.426 Si 2.434 SiMe₃
(2.374) Me₂ (2.375)Me₂ (2.374)
109.2   125.1
(111.8)   (111.8)
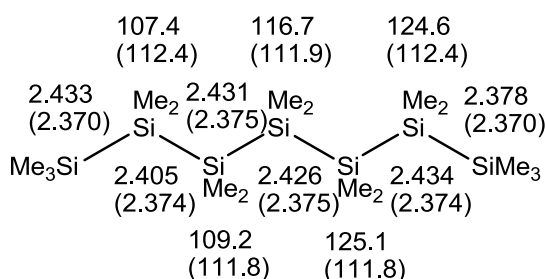
ω=164.7 (163.0), 162.8 (164.1), 166.5 (164.1), 178.4 (163.0)

n-Si₈Me₁₈   C₂ (C₁)

106.2   111.8   125.4
(112.6)   (111.8)   (111.8)
2.419   Me₂2.419 Me₂ 2.420 Me₂
(2.369) Si (2.375)Si (2.375)Si   SiMe₃
Me₃Si 2.407 Si 2.412 Si 2.424 Si 2.383
(2.374) Me₂ (2.376)Me₂ (2.374)Me₂ (2.369)
106.4   118.9   124.3
(111.8)   (111.8)   (112.6)
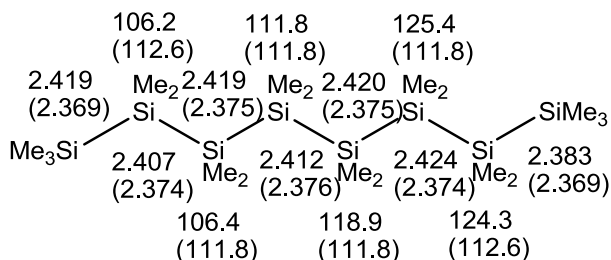
ω=163.5 (162.7), 164.3 (163.5), 162.6 (162.5), 168.3 (163.5), 175.1 (163.5)

Compound 1   C₂ (C₂)

109.5
(104.9)
132.0   Me₂
Me₃Si (114.3) Si   SiMe₃
2.456 Si 2.370 Si
(2.371) (2.368)
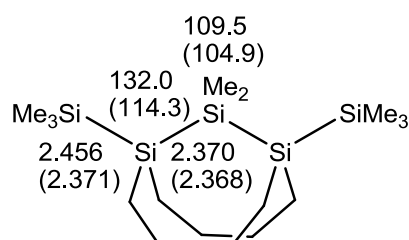
ω=180.0 (177.3)

Figure 3.S1. Geometrical parameters of $n\text{-Si}_n\text{Me}_{2n+2}$ (n=4-8) and compound 1 optimized by DFT and TDDFT calculations with TPSSH functional and the basis sets of 6-31G(d) for Si and 6-31G for C and H. Point group of the excited-state geometry is given in the parenthesis. Excited-state geometrical parameters are listed with ground-state ones in the parenthesis. Si-Si bond distances are given in Å and valence and dihedral angles are in degree.

67

n-Si₄Me₁₀

ground-state geometry
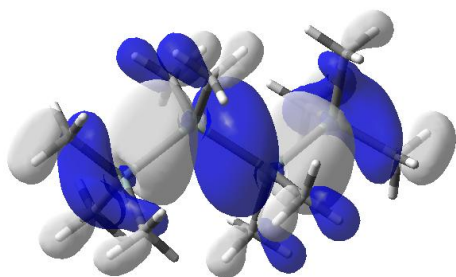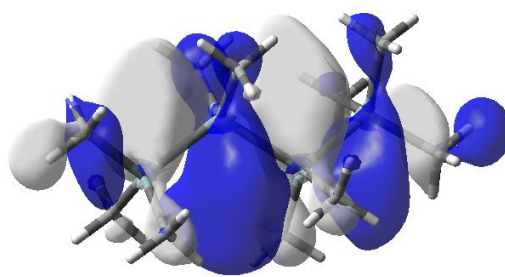
HOMO LUMO

S₁-state geometry
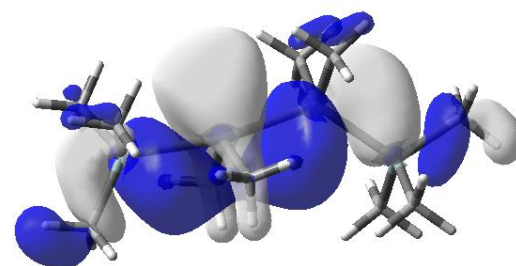
HOMO LUMO

Compound 1(structure restricted peralkylated pentasilane)

ground-state geometry
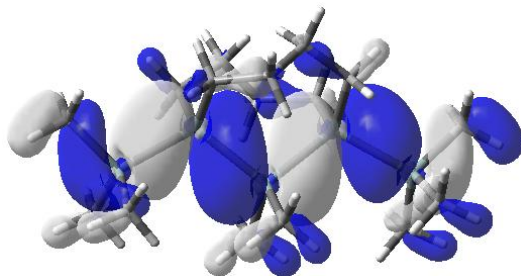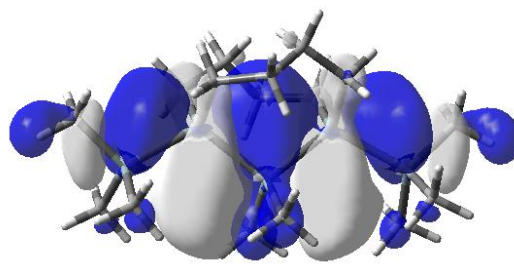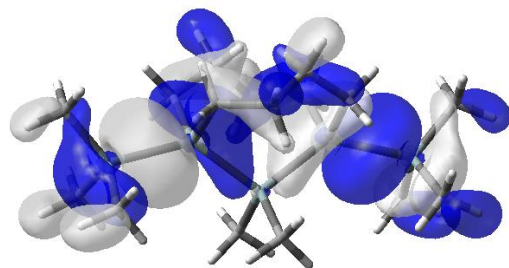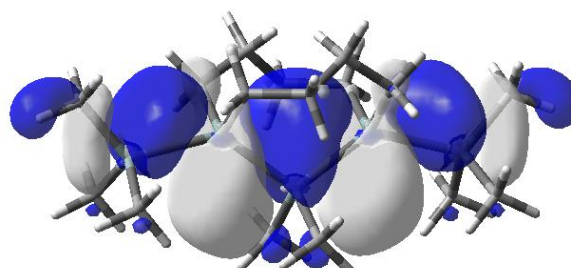
HOMO LUMO

S₁-state geometry

HOMO LUMO

Figure 3.S2. HOMO and LUMO in the S_0 and S_1 state geometries of n-Si_nMe_{2n+2} (n=4-8) and compound 1 (continue)

n-Si₅Me₁₂

ground-state geometry
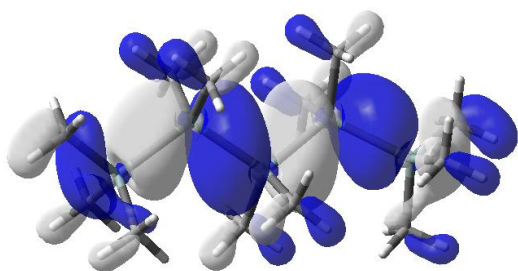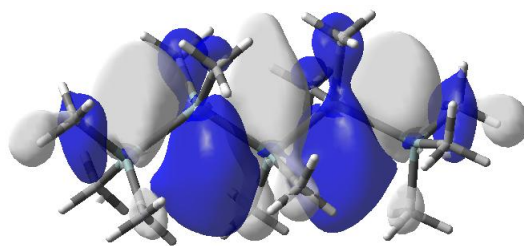
HOMO   LUMO
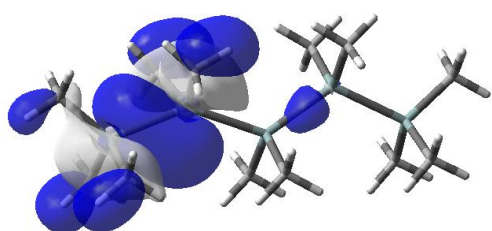
S₁-state geometry
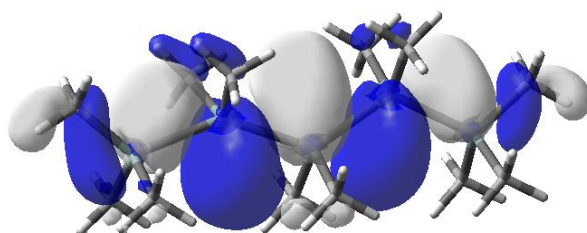
HOMO   LUMO

n-Si₆Me₁₄

ground-state geometry
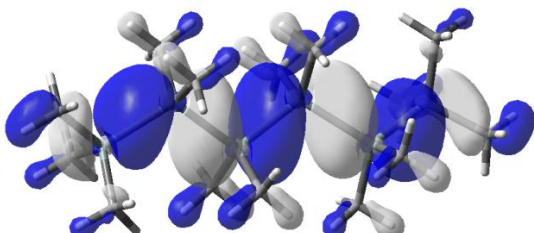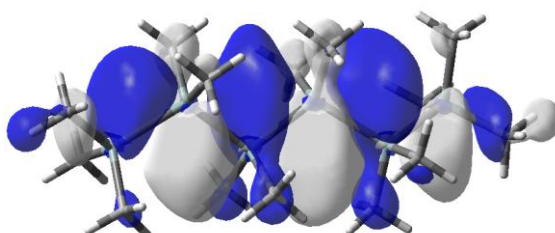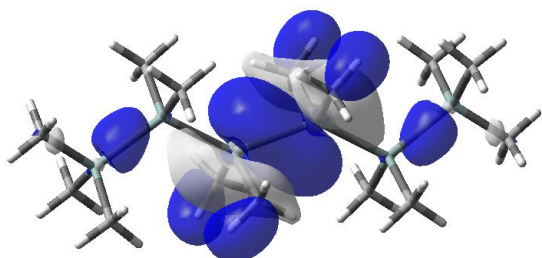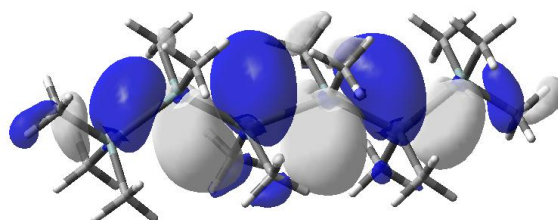
HOMO   LUMO

S₁-state geometry

HOMO   LUMO

Figure 3.S2. HOMO and LUMO in the S_0 and S_1 state geometries of *n*-Si$_n$Me$_{2n+2}$ (n=4-8) and compound 1 (continue)

69

n-Si₇Me₁₆

n-**Si₇Me₁₆**

ground-state geometry
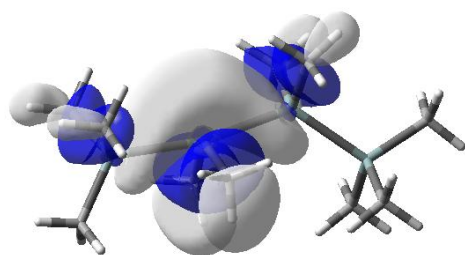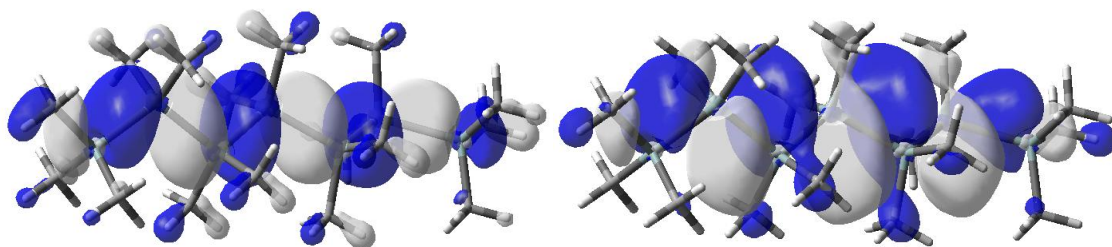

HOMO   LUMO
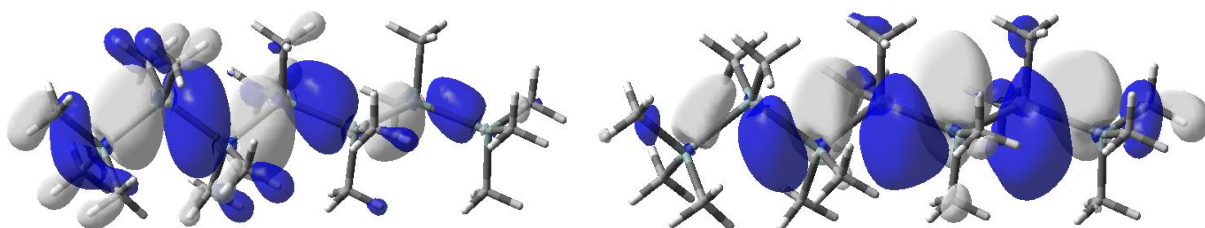
S₁-state geometry

HOMO   LUMO

n-**Si₈Me₁₈**

ground-state geometry
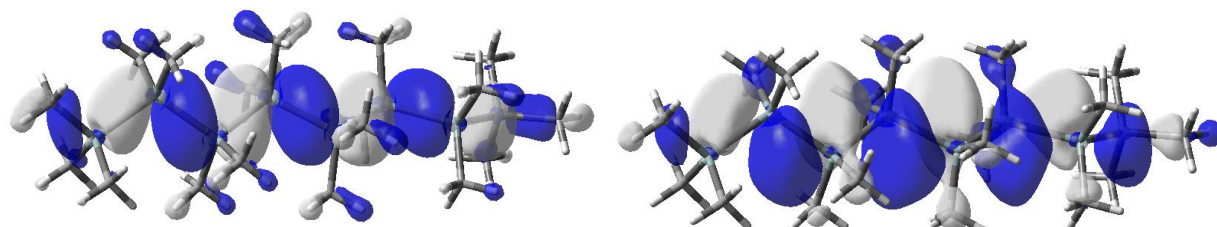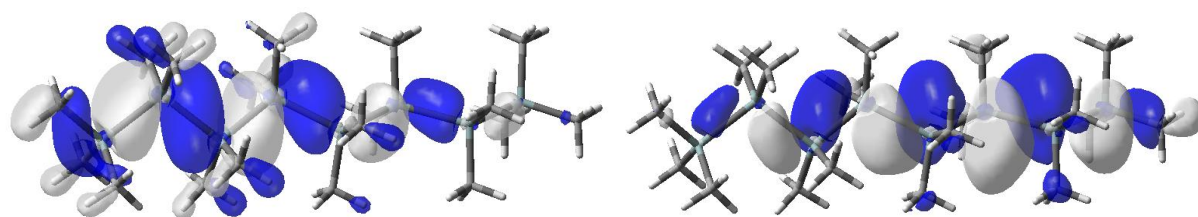
HOMO   LUMO

S₁-state geometry

HOMO   LUMO

Figure 3.S2. HOMO and LUMO in the S_0 and S_1 state geometries of *n*-Si_nMe_{2n+2} (n=4-8) and compound 1 (continued)

Chapter 4

Low-lying π* Resonances of Standard and Rare DNA and RNA Bases Studied by the Projected CAP/SAC-CI Method

The author investigated the low-lying π* resonance states of DNA and RNA bases by the recently developed projected complex absorbing potential (CAP)/symmetry-adapted cluster-configuration interaction (SAC-CI) method with a smooth Voronoi potential as CAP. In spite of the challenging CAP applications to higher resonance states of molecules of this size, the present calculations reproduce resonance positions observed by electron transmission spectra (ETS) provided the anticipated deviations due to vibronic effects and limited basis sets are taken into account. Moreover, for the standard nucleobases, the calculated positions and widths qualitatively agree with those obtained in previous electron scattering calculations. For guanine, both keto and enol forms were examined, and the calculated values of the keto form agree clearly better with the experimental findings. In addition to these standard bases, three modified forms of cytosine, which serve as epigenetic or biomarkers, were investigated: formylcytosine, methylcytosine, and chlorocytosine. Last, a strong correlation between the computed positions and the observed ETS values is demonstrated, clearly suggesting that the present computational protocol should be useful for predicting the π* resonances of congeners of DNA and RNA bases.

4.1. INTRODUCTION

The character and efficiency of electron transfer or electron injection in DNA and RNA play a crucial role in various biological processes.[1-6] On the one hand, this process is relevant to the more general question of charge transfer in DNA, and much experimental and theoretical effort has been devoted to the study of electron attachment to the vacant π^* molecular orbitals (MOs) of DNA bases. On the other hand, low energy electron attachment is responsible for a large percentage of the indirect radiation damage to biological systems.[7-9] Moreover, direct damage, in which energy deposition and subsequent reactions occur directly in DNA, has been observed in ultrafast electron transfer experiments in DNA.[10] In low-energy (< 3eV) electron-induced processes, so-called transient or temporary negative ions, also referred to as resonance states, are early key intermediates in the damage of DNA strands.

Experimentally, the electron transmission spectra (ETS) of the standard DNA and RNA bases have been measured by Aflatooni et al.[6] They observed the electron attachment energies of the lowest three π^* resonances of each base. Theoretically, adiabatic electron attachment of the DNA bases have been extensively studied by many standard quantum chemical calculations,[11-13] the resonance states formed by vertical attachment, however, have been examined less. So far, the resonance states of DNA and RNA bases have been investigated mostly by the electron scattering calculations. The resonances of uracil and its derivatives have been intensively examined by Schwinger multichannel calculations (SMC), for example, uracil by Winstead and Mckoy[14] and more recently, uracil and its halide derivatives by Kossoski et al.[15] In addition, *R*-matrix calculations of uracil have been done by Tonzani and Greene,[16] Gianturco and Lucchese,[17] and Dora and Tennyson et al.[18] There is little systematic theoretical work for the whole series of DNA/RNA bases except for the *R*-matrix calculations at the Hartree-Fock level,[16] followed by the work for the DNA base-pairs where *A*- and *B*-forms of decamers were examined.[19, 20] Recently, electron scattering calculations based on complete active space-configuration interaction (CAS-CI) or Hartree-Fock (HF) wavefunctions were performed for cytosine, thymine,[21] and purine bases.[22] Also, for pyrimidine[23] and purine[24] bases, the interaction of low-energy electrons with nucleosides and nucleotides were examined. Kossoski et al. studied the fragmentation of 2-chloroadenine using density functional theory (DFT) based *R*-matrix calculations.[25] The only application of the complex absorbing potential (CAP) method is work considering the fragmentation of 5-chlorouracil using again HF wavefunctions.[26] However, to our best knowledge, there have been no theoretical studies using the CAP

approach—or any other method yielding lifetimes for multiple states—at correlated levels, because, on the one hand, these molecules have so far been considered to be too "large" for CAP—or similar—calculations at correlated levels beyond second-order perturbation schemes, and, on the other hand, because the calculations of higher lying π^* resonances are inherently challenging.

In the CAP approach a complex potential is added to the normal Hamiltonian, so that the boundary conditions for resonances states change from outgoing-wave to bound state; for the theoretical background of CAPs see Ref. [27]. Thus, the resulting problem can in principle be solved with conventional bound state electronic structure methodologies. Yet, as the resonance is normally not the lowest state in a calculation, and several discretized continuum states are energetically below it, a multi-root electronic structure method is necessary. This requirement naturally limits the applicable electronic structure theories to, for example, HF in the sense of Koopmans's theorem, configuration interaction, Green's function, or equation-of-motion type approaches. The CAP method has been incorporated with multi-reference configuration interaction calculations,[28-32] Green's function methods,[33, 34] and coupled cluster[35-40] as well as related orbital theories.[41, 42] Applications of these methods have been performed for a number metastable systems ranging from electron autoattachment,[43-45] and ionization, to interatomic/intermolecular Coulombic decay.[46]

Here, a method combination of a CAP with symmetry-adapted cluster-configuration interaction (SAC-CI) theory[47-49] is used (CAP/SAC-CI). This particular CAP/SAC-CI combination employs a projection scheme, that is, the CAP Hamiltonian is projected into a set of real SAC-CI vectors,[35, 36] and in a first pilot application,[35] a typical soft-box potential[33] was adopted as a CAP. Recently, the collaborators of the author have introduced two types of Voronoi potentials as CAPs,[50, 51] which have advantages in using the same space symmetry as the investigated molecule and applying to complex molecular structures or clusters, for example, wrapping around side chains and distantly placed monomers. The projected CAP/SAC-CI method with a smooth Voronoi potential has been successfully applied to the π^* resonances of double-bonds and five- and six-membered ring heteroaromatic compounds.[36] The calculated resonance positions are in excellent agreement with the experimental trend: all computed resonance energies are about 0.5 eV higher than the observed ETS values, which can be explained in terms of vibrational effects and the limited basis set. The calculated resonance widths also agree well with those from electron scattering calculations using the *R*-matrix method for pyrazine.[52] It should also be noted that the excited states including circular dichroism

73

(CD) spectra of DNA bases were successfully calculated by the SAC-CI method.[53, 54]

In this work, the lowest three or four π^* resonance states of the standard DNA and RNA bases are investigated: uracil, thymine, cytosine, guanine in its keto and enol forms, and adenine (Figure 4.1). In addition, the rare bases 5-formylcytosine, 5-methylcytosine and 5-chlorocytosine are investigated. These bases are epigenetic markers [see e.g. Refs. [55] and [56]]. While formylcytosine only recently has been identified as a marker as such, and its function is so far unknown, methylcytosine has been studied for far longer and is well known to change the physical properties of the DNA duplex, to be associated with certain diseases, and to play a fundamental role in memory formation. Chlorocytosine, known as an inflammation biomaker, was shown to be intrinsically mutagenic and toxic causing C-T transitions.[57] (Figure 4.1) In the following, the author describes the outline of the projected CAP/SAC-CI theory and the computational details. Then, the author discusses the calculated results referring to the ETS measurements[6] and other previous electron scattering calculations, especially for uracil.
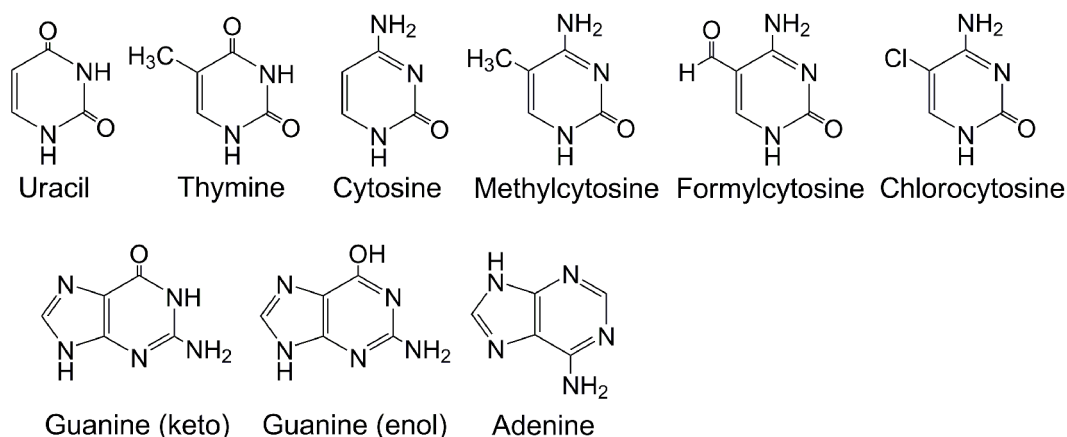
Figure 4.1. Nucleobases studied in the present work.

4.2. THEORETICAL OUTLINE

In order to establish some notation, CAPs as such and our projected CAP/SAC-CI method is briefly summarized. A CAP calculation provides the complex Siegert energy of a resonance,[58, 59]

$$E_{\text{res}} = E_{\text{r}} - i\,\Gamma/2, \tag{1}$$

where E_{r} and Γ, are the resonance position and width, respectively. To locate this

resonance, a CAP, $-iW$, is added to the physical Hamiltonian, H, yielding a non-Hermitian, complex-symmetric Hamiltonian

$$H(\eta) = H - i\eta W, \tag{2}$$

where η is a strength parameter.[60] In this work, a smooth Voronoi CAP is used, which wraps around the molecule like a van der Waals cavity.[50, 51] The resonance energy, E_{res}, is obtained from one of the η-trajectories of the eigenvalues of $H(\eta)$. The eigenvalue representing the resonance typically shows a pronounced stabilization where its η-velocity shows a minimum.[27, 33] Both the uncorrected trajectories, $E(\eta)$, and the corrected trajectories, $E(\eta) - dE(\eta)/d\ln\eta$, were examined with only the corrected resonance energies reported in the paper. Note that the minimum of the "speed" of the uncorrected trajectories corresponds to the minimum of the absolute value of the derivative of the complex eigenvalue with respect to $\ln\eta$, whereas the speed of the corrected trajectories corresponds to the minimum of the curvature of the uncorrected trajectories.[33]

For calculating the temporary anions, the author adopted the projected CAP/SAC-CI method,[35, 36] which has advantages for large systems due to its high throughput character. The projected CAP/SAC-CI starts from the standard electron-attachment (EA) SAC-CI method.[48] The wavefunction of an (N+1)-electron system is represented by

$$\left|\Psi_\mu^{\text{SAC-CI}}\right\rangle = R_\mu^{(N+1)}\left|\Psi_g^{\text{SAC}}\right\rangle, \tag{3}$$

where $\left|\Psi_g^{\text{SAC}}\right\rangle = \exp(\sum_I C_I S_I^\dagger)\left|\Phi_0\right\rangle$ is the ground state SAC wavefunction and $R_\mu^{(N+1)}$ is a linear combination of the electron-attachment operators. For temporary anions of closed-shell systems, electron-attachment can be well described by one-electron operators, and therefore, one can use the SAC-CI SD-R method,[48] in which the excitation operators are limited up to singles and doubles.

The SAC-CI equation can be written in an equation-of-motion formula as[61, 62]

$$\left[H, R_\mu^{(N+1)}\right]\left|\Psi_g^{SAC}\right\rangle = \Delta E R_\mu^{(N+1)}\left|\Psi_g^{SAC}\right\rangle \tag{4}$$

where ΔE is an electron-attachment energy in the present case, $\Delta E = E_\mu^{\text{SAC-CI}} - E_g^{\text{SAC}}$, and $R_\mu^{(N+1)}$ is an electron-attachment operator. Projecting this equation to the space of $\left\langle\Phi_0\right|R_K e^{-S}$, one obtains the working equations,

$$\langle\Phi_0|R_K e^{-S}\left[H,R_\mu^{(N+1)}\right]e^S|\Phi_0\rangle = \Delta E\langle\Phi_0|R_K R_\mu^{(N+1)}|\Phi_0\rangle. \tag{5}$$

This is the SAC-CI NV (non-variational) equation of the electron-attached states. In addition, the author adopted the SAC-CI-V (variational) approximation, where the SAC-CI vectors were obtained from an approximate, symmetrized SAC-CI matrix (SAC-CI-V). The non-symmetric SAC-CI-NV approach was also examined in the previous work,[35] and the energy difference between V and NV schemes was confirmed to be usually small in the projected CAP/SAC-CI calculations.

In a projected method[35, 36] the CAP Hamiltonian as defined in Eq. (2) is expanded within a small subset of SAC-CI eigenvectors analogous to the projected CAP/CI method[31]

$$\langle\Psi_\mu^{\text{SAC-CI}}|H-i\eta W|\Psi_\nu^{\text{SAC-CI}}\rangle = \sum_M\sum_N d_M^\mu d_N^\nu\left(\bar{H}_{MN}+\sum_I C_I\bar{H}_{M,NI}\right) \tag{6}$$

where $\bar{H}_{MN}$ are the matrix elements of $H-i\eta W$ in the configuration basis, $\Psi_\mu^{\text{SAC-CI}}$ and $\Psi_\nu^{\text{SAC-CI}}$ are the μ-th and ν-th SAC-CI-V vectors, the d_N^μ are their SAC-CI coefficients, and $\bar{H}_{M,NI}=\langle\Phi_0|R_M\bar{H}R_N^\dagger S_I^\dagger|\Phi_0\rangle$. In the case of calculating only linear terms, which is a good approximation adopted in the present work, the projected CAP Hamiltonian is complex symmetric similar to the projected CAP/CI method.

Almost simultaneously with the CAP/SAC-CI combination, the CAP approach was also introduced in the EOM-CC method,[37] which is—as discussed above—closely related to the SAC-CI method. Later, an alternative CAP/EOM-CC procedure was implemented, which includes a CAP already at SCF level for the neutral (CAP-SCF).[40] In both CAP/SAC-CI and the earlier CAP/EOM-CC variant, the CAP is included only in calculations for anion states.[35, 36] Despite these technical differences, the three methods usually provide results in excellent agreement with each other provided basis sets and CAPs of similar quality are used. For example, using a soft-box CAP, for the π^* resonance of N_2 the differences for resonance position and width were only a few tenth of an eV: the reported values are 2.44 and 0.39 eV (Ref. [37]) and 2.51 and 0.36 eV (Ref. [40]), respectively, by CAP/EOM-CC, and 2.56 and 0.40 eV by CAP/SAC-CI (Ref. [51]) (the experimental values are 2.32 and 0.41 eV), although the basis sets were not strictly identical.

In the CAP approach, the crucial factor is, of course, the CAP. For simple system like diatomics or linear molecules, the soft-box potential[60] works well. However, for medium-size molecules–depending on symmetry and shape–it can be difficult to choose a box. To overcome this problem, the collaborators of the author introduced two types of Voronoi potentials.[50, 51] In this work, the author uses the smooth Voronoi-CAP, that circumvents any sharp edges at the boundaries between Voronoi cells.[51] Voronoi-CAPs have advantages over the conventional box potential as they, first, have the same symmetry as the molecular system, and, more importantly, can treat large molecules with asymmetric side chains and even molecular clusters without leaving any "dead space", that is, space, which is both poorly described by the atom centered basis set and not in the absorbing region of the CAP. Last, Voronoi CAPs use only one cutoff parameter, that is, a distance between potential and target molecule(s)[51] and the results are less dependent on this parameter in both resonance position and width.[51] A disadvantage is that the integrals must be computed numerically. A similar CAP was also adopted in the field ionization problem.[63, 64] For details, readers are referred to the original articles.[50, 51]

4.3. COMPUTATIONAL DETAILS

In CAP calculations, a sufficiently number of diffuse functions needs to be included for obtaining a satisfactory stabilization of the η-trajectory of the resonance state. In the present calculations, Dunning's cc-pVDZ valence sets[65] was used and augmented with [2s5p2d] sets of diffuse functions on carbon, nitrogen and oxygen. The effect of using a triple zeta basis was not so significant, about 0.1 eV for calculating resonances,[35, 36] provided the number of diffuse functions added is sufficient. The exponents of these diffuse functions must be chosen fairly close, so that an outgoing wave can be represented, yet not too close to avoid near-linear-dependency. Our [2s5p2d] set is a well-tested set fulfilling these criteria. The associated ratios for the diffuse functions are 1.5 for the 5p sets on C, N, and O atoms, and 2 for both the s and d functions. For each atom the scaling procedure starts with the exponent of the outermost orbital in the respective valence cc-pVDZ basis set. With this basis set, the total number of basis functions varied from 348 for uracil to 476 for adenine and guanine. Resonance energies were calculated as vertical transitions at the geometry of the neutral molecule, which itself was computed with the B3LYP/cc-pVTZ[65] method.

The electron-attachment (EA) SAC-CI SD-R calculations were performed with the direct algorithm,[66] where all the product terms are included. To reduce the computational cost, the author employed the perturbation selection procedure for both R and S operators.[67] Recently, the collaborators of the author have performed the benchmark SAC-CI SD-R calculations regarding the energy thresholds of operator selection using the reference functions of canonical and localized MOs.[68] The "LevelThree" accuracy with the energy thresholds of $\lambda_g = 1 \times 10^{-5}$ and $\lambda_e = 1 \times 10^{-6}$ was adopted in the present calculations, which provides reasonable accuracy and computational cost for the present molecules.

The dependence of the resonance energy and width was previously examined for cutoff parameters of the smooth Voronoi potential, which were varied between 0.2~4.0 au.[36, 51] Based on these calculations, the author adopted a cutoff parameter of 4.0 au in the present work.

The EA-SAC-CI and projected CAP/SAC-CI calculations were conducted using the Gaussian09 suite of programs, Revision B.01.[69]

4.4. RESULTS AND DISCUSSION

4.4.1. Uracil

The CAP/SAC-CI results of the π^* resonance states of uracil are summarized in Table 4.1 together with the experimental ETS resonance positions[6] and theoretical results of electron scattering calculations.[14-18] In the EA-SAC-CI calculations, 30 states were computed to cover the energy range up to about 7 eV with the present basis sets. The corrected and uncorrected η-trajectories and their results are shown in Figure 4.S1 and Table 4.S1 in the Supporting Information. The corrected trajectories show clear stabilization for three resonances with the resonance positions at 0.57, 2.21, and 4.82 eV, which are in fair agreement with the observed ETS values by Aflatooni et al., 0.22, 1.58 and 3.83 eV,[6] respectively. Experimentally, these resonances are all assigned to π^* resonances. The present deviations of 0.3~0.6 eV for the π_1^* and π_2^* peaks are assumed to be due to the geometry relaxation effects and the limited basis sets as previously discussed for the double-bond and heteroaromatic compounds.[36] The deviation of the highest π_3^* resonance, however, is as large as about 1.0 eV, which was also observed in the recent electron scattering calculations.[15]

The resonance states of uracil have been intensively studied by the electron

scattering calculations.[14-18] The present calculated values are also in good agreement with those by the recent SMCPP calculations of Kossoski et al.,[15] (0.14, 1.76, and 4.83 eV) and the SMC calculations of Winstead and McKoy (0.32, 1.91, 5.08 eV).[14] These agreements are surprisingly good considering the different methodologies and basis sets adopted. In contrast, the R-matrix calculations based on Hartree-Fock theory (HF/R-matrix) of Tonzani and Greene[16] overestimated resonance positions by about 1.5~2.0 eV but still reproduce the experimental trend[6] similar to the R-matrix calculations of Gianturco and Lucchese (π^* resonances at 2.2, 3.5 and 6.5 eV[17]). It should be emphasized at this point that the disagreements between the theoretical results are not so much due to the differences in the continuum methods or the one-particle basis sets, but foremost due to the differences between the electron correlation treatments. Any electronic structure method used in this context must describe in a balanced manner the decay from an (N+1)-electron system to an N-electron system, that is, some mixture of an (N+1)-electron and an N-electron plus free electron wavefunction; a tough challenge for electron structure theory.

The respective widths for these three resonances were calculated to be 0.05, 0.09 and 0.58 eV. These results are mostly consistent with the features of the ETS cross section data: the π_1^* resonance is narrow, while the π_2^* and π_3^* resonances are broad. It is noted that the computed width is just the electronic contribution, while the observed width may have a substantial vibrational contribution as well. The SMC calculations of Winstead and Mckoy gave the resonance widths of 0.018, 0.16, and 0.40 eV.[14] Considering the different character of the methods, the agreement of the widths is astonishing. Other electron scattering calculations provided similar trends, though the ranges of the widths are wider than those of the resonance positions (see Table 4.1), for example, R-matrix calculations at HF-like levels yielded large widths for the π_3^* resonance: 1.03[17] and 0.9 eV.[16]

Table 4.1. Resonance Position and Width (eV) of π^* Resonance States of Uracil

	π_1^*		π_2^*		π_3^*	
	E_r	Γ	E_r	Γ	E_r	Γ
Expt.[a]	0.22	–	1.58	–	3.83	–
CAP/SAC-CI[b]	0.57	0.05	2.21	0.09	4.82	0.58
SMCPP (2014)[c]	0.14	0.005	1.76	0.15	4.83	0.78
CC (2009)[d]	0.13	0.003	1.94	0.17	4.95	0.38
SEP (2007)[e]	0.32	0.018	1.91	0.16	5.08	0.40
R-matrix (2004)[f]	2.27	0.21	3.51	0.38	6.5	1.03
R-matrix (2006)[g]	2.16	0.2	5.16	0.6	7.80	0.9

[a] Aflatooni et al. in Ref. [6], [b] Corrected η-trajectory was used., [c] Kossoski et al. in Ref. [15], [d] Dora and Tennyson et al. in Ref. [18], [e] Winstead and McKoy in Ref. [14], [f] Gianturco and Lucchese in Ref. [17], [g] Tonzani and Greene in Ref. [16]

4.4.2. Thymine

The π^* resonances of thymine were investigated by the ETS[6] and electron scattering calculations,[16, 21, 23] while vibrational Feshbach resonances associated to σ^* orbitals were also intensively studied.[70] Here, the author focus on the three low-lying π^* resonances. Thymine can be thought of as a σ-electron donating methyl group bonded to a uracil unit and therefore, the resonance positions of thymine are expected to be shifted up relative to those of uracil, similar to what is known for formaldehyde and acetaldehyde.[35, 36, 71, 72] The uracil derivatives with electron-withdrawing halogen substituents were studied by the SMC calculations, and as expected the σ-withdrawing effect of the halogen substituents had the opposite effect on the resonance positions.[15]

The results of thymine based on corrected η-trajectories are summarized in Table 4.2. Both corrected and uncorrected η-trajectories of three π^* resonances are shown in Figure 4.S2. The CAP/SAC-CI resonance positions are 0.67, 2.28, and 5.14 eV. These positions are about 0.1 eV higher than those of uracil as expected due to the methyl group. Thus, the CAP calculations reproduce the trend observed in ETS measurements.[6] This trend was also reproduced in R-matrix calculations,[16] though the absolute values were significantly overestimated, while it was not necessarily reproduced in other electron scattering static-exchange plus polarization (SEP) calculations.[23] Both corrected and uncorrected η-trajectories showed clear stabilization except for the π_3^* resonance, for which only the corrected trajectory gave a satisfactory stabilization behavior (Figure 4.S2). These shape resonances were observed at 0.29, 1.71, and 4.05 eV by the ETS by Aflatooni et al.,[6] which are 0.07~0.22 eV higher than those of uracil. Again, the expected agreement was obtained for π_1^* and π_2^* resonances, but, the deviation is larger for the π_3^* resonance. The uncorrected close-coupling (u-CC) calculations by Dora and Tennyson et al.,[21] which was based on CAS-CI and the best approximation in their calculations, gave similar results with our calculations. The R-matrix calculations by Tonzani and Greene[16] are based on HF theory, and are therefore expected to give much higher positions and much larger widths than our CAP/SAC-CI calculations, which is true.[16] Unfortunately, there are no experimental values reported regarding resonance widths.

Table 4.2. Resonance Position and Width (eV) of π* Resonance States of Thymine

	π_1*		π_2*		π_3*	
	E_r	Γ	E_r	Γ	E_r	Γ
Expt.[a]	0.29	–	1.71	–	4.05	–
CAP/SAC-CI[b]	0.67	0.11	2.28	0.15	5.14	0.41
u-CC (2012)[c]	0.53	0.08	2.41	0.10	5.26	–
SEP (2012)[c]	0.60	0.11	2.73	0.11	5.52	0.57
SEP (2007)[d]	0.30	–	0.19	–	5.70	–
R-matrix (2006)[e]	2.40	0.20	5.50	0.60	7.90	1.00

[a] Ref. [6], [b] Projected CAP/SAC-CI with smooth Voronoi potential using corrected trajectory, [c] Dora and Tennyson et al., Ref. [21], [d] Winstead and McKoy et al., Ref. [23], [e] Tonzani and Greene, Ref. [16]

4.4.3. Cytosine, Formylcytosine, Methylcytosine, and Chlorocytosine

Using ETS, the π* resonances of cytosine were observed at 0.32, 1.53, and 4.50 eV.[6] The π_1* and π_3* resonances are less bound compared to uracil or thymine as cytosine has only one electron-withdrawing carbonyl group, however, the π_2* resonance position is somewhat lower in energy in cytosine. The projected CAP/SAC-CI calculations reproduced this trend as shown in Table 4.3. The calculated resonance positions are 0.70, 2.18, and 5.66 eV. Both corrected and uncorrected trajectories showed clear stabilization for all of these three resonances as shown in Figure 4.S3.

Electron scattering calculations were also reported for the π* resonances of this molecule.[16, 21, 23] Again, considering the different character of the methods, the agreement is good in particular in comparison with the u-CC values of Dora et al.;[21] the resonance positions were reported as 0.36, 2.05, and 5.35 eV. The position for π_3* resonances were overestimated in all other R-matrix (SEP) calculations as ~6.30[21, 23] and ~8.1 eV.[16] The resonance widths of the present CAP/SAC-CI results are close to those of Ref. [21]; the present values of 0.16, 0.30, and 0.63 eV compare well with those by Dora et al. of 0.05, 0.33, and 0.72 eV (SEP), respectively. R-matrix calculations of Tonzani et al.[16] again gave much larger widths for these resonances owing to the HF level used in these calculations, 0.5, 0.7, and 0.8 eV, respectively.

The derivatives of cytosine are of interest in view of the control of the electron attachment resonance position. The simplest case, methylcytosine was first studied. As established in the uracil-thymine and formaldehyde-acetaldehyde cases, a methyl group should have a slightly destabilizing effect on the π* resonance levels due its inductive

effect. However, the three π^* resonance positions were calculated at 0.74, 2.57, and 5.44 eV, and only the lower two resonances follow the expected trend. The author emphasizes that the stabilizations of the η-trajectories of all of these resonances are clear (Figure 4.S4). Clearly, in larger molecules methyl substitutions cannot be expected to have a uniform effect on all π^* levels.

5-Formylcytosine is a rare base found in mammalian DNA sequence and has been recently studied.[55] From a "study of resonances" point of view, this molecule is of interest because it extends the conjugation present in cytosine. Moreover, from a technical point of view, its irregular molecular shape is a good example for the use of a smooth Voronoi potential in contrast to a soft box-potential. The two lower π_1^* and π_2^* resonances showed a clear stabilization for both the corrected and uncorrected trajectories (Figure 4.S5), their resonance positions are calculated at 0.53 and 2.65 eV, respectively (Table 4.3). The π_1^* resonance is lower than that of cytosine due to the extended π-conjugation, while the π_2^* resonance shows the opposite trend. The resonance position of the π_3^* state (4.85 eV) whose stabilization is less clear, in particular, for the uncorrected η-trajectory, was calculated much lower than that of cytosine.

The Cl substitution is of interest in view of fragmentation due to low-energy electrons. Previously, the CAP study based on HF was performed for the fragmentation of 5-chlorouracil.[26] Also electron scattering calculations were recently applied to chlorouracil.[15] In this work, three π^* resonances of 5-chlorocytosine were obtained at 0.43, 2.05, and 5.35 eV (Table 4.3, Figure 4.S6). Reflecting σ-electron-withdrawing nature of Cl, all the calculated resonance positions of chlorocytosine are lower than those of pristine cytosine. The resonance widths of this Cl-derivative are slightly narrower than those of cytosine.

Table 4.3. Resonance Position and Width (eV) of π* Resonance States of Cytosine and its Derivatives

	π_1*		π_2*		π_3*	
	E_r	Γ	E_r	Γ	E_r	Γ
Cytosine						
Expt.[a]	0.32	–	1.53	–	4.50	–
CAP/SAC-CI[b]	0.70	0.16	2.18	0.30	5.66	0.63
u-CC (2012)[c]	0.36	0.016	2.05	0.30	5.35	–
SEP (2012)[c]	0.71	0.05	2.66	0.33	6.29	0.72
SEP (2007)[d]	0.50	–	2.40	–	6.30	–
R-matrix (2006)[e]	1.7	0.5	4.3	0.7	8.1	0.8
5-Methylcytosine						
CAP/SAC-CI[b]	0.74	0.17	2.57	0.34	5.44	0.33
5-Formylcytosine						
CAP/SAC-CI[b]	0.53	0.28	2.65	0.30	4.85	0.23
5-Chlorocytosine						
CAP/SAC-CI[b]	0.43	0.17	2.05	0.18	5.35	0.38

[a] Ref. [6], [b] Projected CAP/SAC-CI with smooth Voronoi potential using corrected trajectory, [c] Dora and Tennyson et al., Ref. [21], [d] Winstead and McKoy et al., Ref. [23], [e] Tonzani and Greene, Ref. [16]

4.4.4. Guanine

Guanine has keto and enol tautomers located close in energy (Figure 4.1) so that in equilibrium both should be present; the relative free energy in the gas phase was theoretically evaluated as 0.6 kcal/mol.[73] In the ETS experiment, the enol tautomer was suggested to dominate, on the one hand, since it was observed in the environment of rare gas matrices, and, on the other hand, based on an analysis of the spectra with a help of SCF MO calculations.[6] Here, three π* resonances of both structures were computed using the projected CAP/SAC-CI method. The results are summarized in Table 4.4 together with the ETS values.[6] In the present CAP calculations of guanine, both corrected and uncorrected η-trajectories showed clear stabilization as shown in Figures 4.S7 and 4.S8. Previous electron scattering calculations[16, 22, 24] for the keto form are also given.

Table 4.4. compares the CAP/SAC-CI results for both guanine tautomers with all previous scattering results. The previous electron scattering calculations gave higher resonance positions for these three resonance states compared to experiment and the present results except for π_1* state;[16, 22, 24] the present values, 1.11, 1.66 and 3.21 eV, are

83

compared to those of u-CC values based on CAS-CI,[21] 0.97, 2.41 and 3.78 eV, respectively. Referring to the resonance widths calculated by u-CC in Ref. [22, 24], the present resonance widths are larger, in particular for π_1* resonance. Moreover, for guanine, in addition to the π_1*-π_3* resonances, the author could locate the fourth $\pi*$ resonance at ~6.50 eV, though only the corrected trajectory gave a clear stabilization. The previous u-CC result is 6.42 eV with a resonance width of 0.72 eV, which are both close to the present calculations.[21]

Table 4.4. Resonance Position and Width (eV) of $\pi*$ Resonance States of Guanine (Keto and Enol Form)

	π_1*		π_2*		π_3*		π_4*	
	E_r	Γ	E_r	Γ	E_r	Γ	E_r	Γ
Keto								
Expt.[a]	0.46	–	1.37	–	2.36	–	–	–
CAP/SAC-CI[b]	1.11	0.64	1.66	0.34	3.21	0.55	6.50	0.92
u-CC (2012)[c]	0.97	0.006	2.41	0.15	3.78	0.29	6.42	0.72
SEP (2012)[c]	1.83	0.16	3.30	0.24	4.25	0.33	7.36	0.27
SEP (2007)[d]	1.55	–	2.40	–	3.75	–	–	–
R-matrix (2006)[e]	2.00	0.20	3.80	0.25	4.80	0.35	8.90	0.60
Enol								
CAP/SAC-CI[b]	1.26	0.15	2.19	0.09	3.13	0.33	6.61	0.72

[a] Ref. [6], [b] Projected CAP/SAC-CI with smooth Voronoi potential using corrected trajectory, [c] Dora and Tennyson et al., Ref. [22], [d] Winstead and McKoy et al., Ref. [24], [e] Tonzani and Greene, Ref. [16]

Based on our calculations, the results of the keto form are closer to the ETS values, in particular for the π_1* to π_2* resonances. The agreement of the resonance positions was similar for other nucleobases: typical deviations are 0.55 and 0.29 eV for the lower two resonances and 0.85 eV for π_3* resonance. Thus, the author attributed the peaks observed by ETS to those of the keto form, and not to the enol tautomer—opposed to the original assignment based on SCF calculations.[6]

4.4.5. Adenine

The CAP/SAC-CI results of adenine are listed in Table 4.5 with ETS experiment and other electron scattering calculations.[16, 22, 24] In contrast to the other nucleobases, the agreement of the resonance position for the π_3* state is better for adenine; with the deviation being 0.55 eV. Compared to other electron scattering calculations, the agreement of the calculated resonance positions with ETS values is generally good for

the low-lying three resonances. It is noted that for the π_2^* resonance the stabilization was less clear than for the other bases for both the corrected and uncorrected trajectories, yet clear enough to locate the position. As for other nucleobases, the present resonance widths are larger than those of u-CC and SEP calculations.[21]

As in guanine, the fourth π^* resonance can be seen in the η-trajectories at 6.65 eV. The stabilization of this resonance is clear in both the corrected and uncorrected trajectories, and its correlation with the unoccupied SCF MOs is demonstrated in the Supporting Information. This state was also obtained by u-CC and SEP calculations by Dora et al.,[21] though the energy was reported higher, at 7.97 and 7.07 eV, respectively. Recently, SMC calculations based on B3LYP were done for 2-chloroadenine. Four π^* resonance states were calculated at 0.56, 1.12, 2.72, and 6.02 eV.[25] The resonance energies of this derivative are similar though the widths deviate from those of adenine.

**Table 4.5.** Resonance Position and Width (eV) of π^* Resonance States of Adenine

	π_1^*		π_2^*		π_3^*		π_4^*	
	E_r	Γ	E_r	Γ	E_r	Γ	E_r	Γ
Expt.[a]	0.54	–	1.36	–	2.17	–	–	–
CAP/SAC-CI[b]	0.89	0.13	1.93	0.29	2.72	0.17	6.65	0.57
u-CC (2012)[c]	1.58	0.22	2.44	0.14	4.38	0.67	7.94	0.57
SEP (2012)[c]	1.30	0.14	2.12	0.09	3.12	0.28	7.07	0.24
SEP (2007)[d]	1.10	–	1.80	–	4.10	–	–	–
R-matrix (2006)[e]	2.40	0.20	3.20	0.20	4.40	0.30	–	–

[a] Ref. [6], [b] Projected CAP/SAC-CI with smooth Voronoi potential using corrected trajectory, [c] Dora and Tennyson et al., Ref. [22], [d] Winstead and McKoy et al., Ref. [24], [e] Tonzani and Greene, Ref. [16]

4.6. Correlation with ETS measurements

It is clear that there is currently no practical method to predict energies and lifetimes of temporary anions of molecules in the size range of nucleobases with high accuracy. However, there are clearly methods that will reproduce the relevant trends quite closely, in particular if dynamic electronic correlation beyond second order is taken into account. Here this reproduction of trends is investigated more quantitatively. The correlation between ETS and CAP/SAC-CI values for all the π^* resonance states of the DNA and RNA bases, uracil, thymine, cytosine, guanine (keto), and adenine, is plotted in Figure 4.2. The agreement with the ETS values is excellent like in the previous study for the double-bond and heteroaromatic resonances.[35, 36] The linear fit is obtained as $E(\text{ETS})=0.84E_r(\text{CAP/SAC-CI})-0.26$ (all in eV). Note however, that for this

highly specialized set of molecules the linear fit is somewhat different than that from the more generic set of molecules. The agreement is surprisingly good, especially considering that the present data set includes high-lying resonances of up to ~5 eV. Clearly, the present computational protocol combined with the established empirical relationship can be used to predict the experimental resonance positions of π^* resonances of molecules related to this set, for example, derivatives of DNA and RNA bases such as the epigenetic markers investigated here.
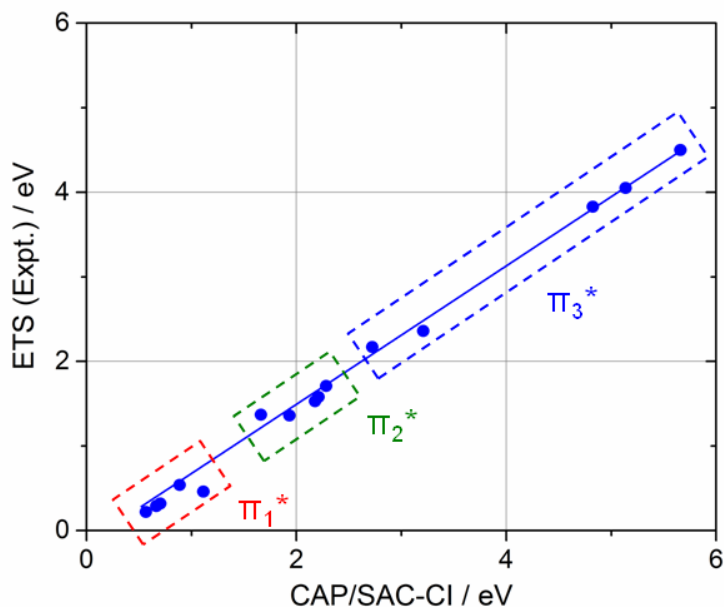
Figure 4.2. Correlation of the ETS and CAP/SAC-CI (smooth Voronoi potential) values for the π^* resonance states of five DNA and RNA bases.

4.5. SUMMARY

The author has investigated low-lying π^* resonance states of common and rare DNA and RNA bases by the recently developed projected CAP/SAC-CI method combined with a smooth Voronoi potential as a CAP. This method is size-consistent and takes dynamic electron correlation well beyond second-order perturbation theory into account. It is nevertheless able to characterize several resonances for molecules in the size range of guanine or adenine—a challenge for CAP/SAC-CI calculations. The calculated resonance positions are in good agreement with the experimental ETS values provided the anticipated deviations due to vibronic effects and the limited basis sets are taken into account.[35, 36] Similar to more generic π^* resonances, this more specialized set

of molecules also shows a strong correlation between the computed positions and the ETS values clearly suggesting that the present computational protocol should be useful for predicting the π^* resonances of congeners of the DNA/RNA bases.

The comparison with the results of the previous electron scattering calculations was also encouraging. For the standard nucleobases, the trend of the calculated positions and widths agrees well with that of the most recent SMC or *R*-matrix calculations. The π_3^* resonance position seems to be still challenging and the deviation from the ETS value is around 1 eV similar to the latest SMC calculations, though the present CAP calculations improved the position especially for adenine. Resonances of three modified forms of cytosine, which serve as epigenetic or biomarkers, were predicted, whose values would be insightful for electron trapping of correspondingly modified DNA.[55] This application also shows the advantage of using a Voronoi potential for molecules with a side chain or branched conjugation. Last, for guanine, the author examined the resonances of both keto and enol forms. The calculated values of the keto tautomer agree clearly better with the ETS values, which is different from the original interpretation.

ASSOCIATED CONTENT
Supporting Information
All corrected and uncorrected η-trajectories, π^* MOs, and resonance position and width of all the molecules. The Supporting Information is available free of charge on the ACS Publications website.

REFERENCES
(1)   Dandliker, P. J.; Holmlin, R. E.; Barton, J. K., Oxidative Thymine Dimer Repair in the DNA Helix. *Science* **1997**, *275*, 1465-1468.

(2)   Brun, A. M.; Harriman, A., Energy-Transfer and Electron-Transfer Processes Involving Palladium Porphyrins Bound to DNA. *J. Am. Chem. Soc.* **1994**, *116*, 10383-10393.

(3)   Meade, T. J.; Kayyem, J. F., Electron Transfer through DNA: Site-Specific Modification of Duplex DNA with Ruthenium Donors and Acceptors. *Angew. Chem. Int. Ed. Engl.* **1995**, *34*, 352-354.

(4)   Felts, A. K.; Pollard, W. T.; Friesner, R. A., Multilevel Redfield Treatment of Bridge-Mediated Long-Range Electron-Transfer - a Mechanism for Anomalous Distance Dependence. *J. Phys. Chem.* **1995**, *99*, 2929-2940.

(5)   Riyadarshy, S.; Risser, S. M.; Beratan, D. N., DNA is not a Molecular Wire: Protein-Like Electron-Transfer Predicted for an Extended π-Electron System. *J. Phys. Chem.* **1996**, *100*,

17678-17682.

(6)   Aflatooni, K.; Gallup, G. A.; Burrow, P. D., Electron Attachment Energies of the DNA Bases. *J. Phys. Chem. A* **1998**, *102*, 6205-6207.

(7)   Sanche, L., Low Energy Electron-Driven Damage in Biomolecules. *Eur. Phys. J* **2005**, *35*, 367-390.

(8)   Baccarelli, I.; Bald, I.; Gianturco, F. A.; Illenberger, E.; Kopyra, J., Electron-Induced Damage of DNA and Its Components: Experiments and Theoretical Models. *Phys. Rep.* **2011**, *508*, 1-44.

(9)   Bald, I.; Illenberger, E.; Kopyra, J., Damage of DNA by Low Energy Electrons (< 3 eV). *J. Phys.: Conf. Ser.* **2012**, *373*, 012008.

(10)   Nguyen, J.; Ma, Y.; Luo, T.; Bristow, R. G.; Faffray, D. A.; Lu, Q. B., Direct Observation of Ultrafast-Electron-Transfer Reactions Unravels High Effectiveness of Reductive DNA Damage. *Proc. Natl. Acad. Sci. U.S.A. (PNAS)* **2011**, *108*, 11778-11783.

(11)   Roca-Sanjuan, D.; Merchan, M.; Serrano-Andres, L.; Rubio, M., Ab initio determination of the electron affinities of DNA and RNA nucleobases *J. Chem. Phys.* **2008**, *129*, 095104.

(12)   Dediková, P.; Demovič, L.; Pitoňák, M.; Neogrády, P.; Urban, M., CCSD(T) Calculations of the Electron Affinity of the Uracil Molecule *Chem. Phys. Lett.* **2009**, *481*, 107-111.

(13)   Dutta, A. K.; Sengupta, T.; Vaval, N.; Pal, S., Electron Attachment to DNA and RNA Nucleobases: An EOMCC Investigation. *Int. J. Quantum Chem.* **2015**, *115*, 753-764.

(14)   Winstead, C.; McKoy, V., Low-Energy Electron Collisions with Gas-Phase Uracil. *J. Chem. Phys.* **2006**, *125*, 174304.

(15)   Kossoski, F.; Bettega, M. H. F.; do N Varella, M. T., Shape Resonance Spectra of Uracil, 5-Fluorouracil, and 5-Chlorouracil. *J. Chem. Phys.* **2014**, *140*, 024317.

(16)   Tonzani, S.; Greene, C. H., Low-Energy Electron Scattering from DNA and RNA Bases: Shape Resonances and Radiation Damage. *J. Chem. Phys.* **2006**, *124*, 054312.

(17)   Gianturco, F. A.; Lucchese, R. R., Radiation Damage of Biosystems Mediated by Secondary Electrons: Resonant Precursors for Uracil Molecules. *J. Chem. Phys.* **2004**, *120*, 7446-7455.

(18)   Dora, A.; Tennyson, J.; Bryjko, L.; van Mourik, T., R-Matrix Calculation of Low-Energy Electron Collisions with Uracil. *J. Chem. Phys.* **2009**, *130*, 164307.

(19)   Caron, L.; Sanche, L.; Tonzani, S.; Greene, C. H., Diffraction in Low-Energy Electron Scattering from DNA: Bridging Gas-Phase and Solid-State Theory. *Phys. Rev. A* **2008**, *78*, 042710.

(20)   Caron, L.; Sanche, L.; Tonzani, S.; Greene, C. H., Low-Energy Electron Scattering from DNA Including Structural Water and Base-Pair Irregularities. *Phys. Rev. A* **2009**, *80*, 012705.

(21)   Dora, A.; Bryjko, L.; van Mourik, T.; Tennyson, J., R-matrix Study of Elastic and Inelastic

Electron Collisions with Cytosine and Thymine. *J. Phys. B: At. Mol. Opt. Phys.* **2012**, *45*, 175203.

(22) Dora, A.; Bryjko, L.; van Mourik, T.; Tennyson, J., Low-energy Electron Scattering with the Purine Bases of DNA/RNA Using the R-matrix Method. *J. Chem. Phys.* **2012**, *136*, 024324.

(23) Winstead, C.; McKoy, V.; d'Almeida Sanchez, S., Interaction of Low-energy Electrons with the Pyrimidine Bases and Nucleosides of DNA. *J. Chem. Phys.* **2007**, *127*, 085105.

(24) Winstead, C.; McKoy, V., Interaction of Low-energy Electrons with the Purine Bases, Nucleosides, and Nucleotides of DNA. *J. Chem. Phys.* **2006**, *125*, 244302.

(25) Kossoski, F.; Kopyra, J.; do N Varella, M. T., Anion States and Fragmentation of 2-Chloroadenine upon Low-energy Electron Collisions. *Phys. Chem. Chem. Phys.* **2015**, *17*, 28958-28965.

(26) Sommerfeld, T., Electron-Induced Chemistry of 5-Chlorouracil. *ChemPhysChem* **2001**, *2*, 677-679.

(27) Riss, U. V.; Meyer, H.-D., Calculation of Resonance Energies and Widths Using the Complex Absorbing Potential Method. *J. Phys. B* **1993**, *26*, 4503-4536.

(28) Chao, J. S.-Y.; Falcetta, M. F.; Jordan, K. D., Application of the Stabilization Method to the N_2 ($1^2\Pi_g$) and Mg^- (1^2P) Temporary Anion States. *J. Chem. Phys.* **1990**, *93*, 1125-1135.

(29) Sommerfeld, T.; Riss, U. V.; Meyer, H.-D.; Cederbaum, L. S.; Engels, B.; Suter, H. U., Temporary Anions - Calculation of Energy and Lifetime by Absorbing Potentials: The N_2^- $^2\Pi_g$ Resonance. *J. Phys. B.* **1998**, *31*, 4107-4122.

(30) Sommerfeld, T.; Tarantelli, F.; Meyer, H.-D.; Cederbaum, L. S., Ab Initio Calculation of Energies and Lifetimes of Metastable Dianions: The C_2^{2-} Resonance. *J. Chem. Phys.* **2000**, *112*, 6635-6642.

(31) Sommerfeld, T., Resonance states of atomic Di-anions. *Phys. Rev. Lett.* **2000**, *85*, 956-959.

(32) Sommerfeld, T.; Santra, R., Efficient Method to Perform CAP/CI Calculations for Temporary Anions. *Intern. J. Quantum Chem.* **2001**, *82*, 218-226.

(33) Santra, R.; Cederbaum, L. S., Complex Absorbing Potentials in the Framework of Electron Propagator Theory. I. General Formalism. *J. Chem. Phys.* **2002**, *117*, 5511-5521.

(34) Feuerbacher, S.; Sommerfeld, T.; Santra, R.; Cederbaum, L. S., Complex Absorbing Potentials in the Framework of Electron Propagator Theory. II. Application to Temporary Anions. *J. Chem. Phys.* **2003**, *118*, 6188-6199.

(35) Ehara, M.; Sommerfeld, T., CAP/SAC-CI Method for Calculating Resonance States of Metastable Anions. *Chem. Phys. Lett.* **2012**, *537*, 107-112.

(36) Ehara, M.; Fukuda, R.; Sommerfeld, T., Projected CAP/SAC-CI Method with Smooth Voronoi Potential for Calculating Resonance States. *J. Comput. Chem.* **2016**, *37*, 242-249.
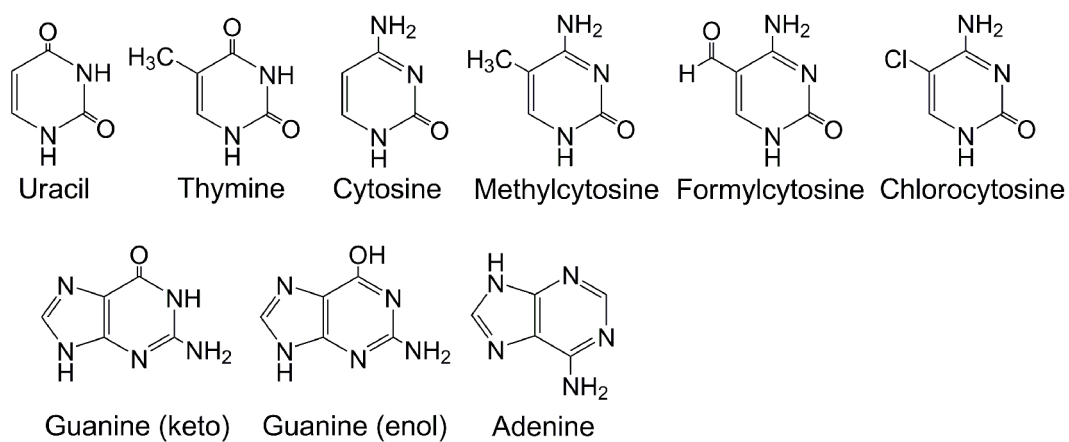
(37) Ghosh, A.; Vaval, N.; Pal, S., Equation-of-Motion Coupled-Cluster Method for the Study

of Shape Resonance. *J. Chem. Phys.* **2012**, *136*, 234110.

(38) Ghosh, A.; Karne, A.; Pal, S., CAP/EOM-CCSD Method for the Study of Potential Curves of Resonant States. *Phys. Chem. Chem. Phys.* **2013**, *15*, 17915-17921.

(39) Jagau, T. C.; Zuev, D.; Bravaya, K. B.; Epifanovsky, E.; Krylov, A. I., A Fresh Look at Resonances and Complex Absorbing Potentials: Density Matrix-Based Approach. *J. Phys. Chem. Lett.* **2014**, *5*, 310-315.

(40) Zuev, D.; Jagau, T. C.; Bravaya, K. B.; Epifanovsky, E.; Shao, Y. H.; Sundstrom, E.; Head-Gordon, M.; Krylov, A. I., Complex Absorbing Potentials within EOM-CC Family of Methods: Theory, Implementation, and Benchmarks. *J. Chem. Phys.* **2014**, *141*, 024102.

(41) Sajeev, Y.; Pal, S., A General Formalism of the Fock Space Multireference Coupled Cluster Method for Investigating Molecular Electronic Resonances. *Mol. Phys.* **2005**, *103*, 2267-2275.

(42) Sajeev, Y.; Santra, R.; Pal, S., Analytically Continued Fock Space Multireference Coupled-Cluster Theory: Application to the $^2\Pi_g$ Shape Resonance in E-N_2 Scattering. *J. Chem. Phys.* **2005**, *122*, 234320.

(43) Čársky, P.; Čurík, R., *Low-Energy Electron Scattering from Molecules, Biomolecules and Surfaces (CRC 2012).* CRC Press: Boca Raton, 2012.

(44) Sugioka, Y.; Takayanagi, T., A Practical Approach to Temperature Effects in Dissociative Electron Attachment Cross Sections Using Local Complex Potential Theory. *Chem. Phys.* **2012**, *405*, 189-196.

(45) Kunitsa, A. A.; Bravaya, K. B., First-Principles Calculations of the Energy and Width of the ^2A_u Shape Resonance in p-Benzoquinone: A Gateway State for Electron Transfer *J. Phys. Chem. Lett.* **2015**, *6*, 1053-1058.

(46) Sajeev, Y.; Ghosh, A.; Vaval, N.; Pal, S., Coupled Cluster Methods for Autoionisation Resonances. *Int. Rev. Phys. Chem.* **2014**, *33*, 397-425.

(47) Nakatsuji, H., Cluster Expansion of Wavefunction - Excited-States. *Chem. Phys. Lett.* **1978**, *59*, 362-364.

(48) Nakatsuji, H., Cluster Expansion of the Wavefunction - Electron Correlations in Ground and Excited-States by SAC (Symmetry-Adapted-Cluster) and SAC CI Theories. *Chem. Phys. Lett.* **1979**, *67*, 329-333.

(49) Nakatsuji, H., Electronic-Structures of Ground, Excited, Ionized and Anion States Studied by the SAC/SAC-CI Theory. *Acta Chim. Acad. Sci. Hung.* **1992**, *129*, 719-776.

(50) Sommerfeld, T.; Ehara, M., Short-Range Stabilizing Potential for Computing Energies and Lifetimes of Temporary Anions with Extrapolation Methods. *J. Chem. Phys.* **2015**, *142*, 034105.

(51) Sommerfeld, T.; Ehara, M., Complex Absorbing Potentials with Voronoi Isosufaces Wrapping Perfectly around Molecules. *J. Chem. Theory Comput.* **2015**, *11*, 4627-4633.

(52) Mašin, Z.; Gorfinkiel, J. D., Elastic and Inelastic Low-Energy Electron Collisions with Pyrazine. *J. Chem. Phys.* **2011**, *135*, 144308.

(53) Miyahara, T.; Nakatsuji, H.; Sugiyama, H., Helical Structure and Circular Dichroism Spectra of DNA: A Theoretical Study. *J. Phys. Chem. A* **2013**, *117*, 42-55.

(54) Miyahara, T.; Nakatsuji, H., Indicator of the Stacking Interaction in the DNA Double-Helical Structure: ChiraSac Study. *J. Phys. Chem. A* **2015**, *119*, 8269-8278.

(55) Bachman, M.; Uribe-Lewis, S.; Yang, X.; Burgess, H. E.; Iurlaro, M.; Reik, W.; Murrell, A.; Balasubramanian, S., 5-Formylcytosine can be a Stable DNA Modification in Mammals. *Nature Chem. Bio.* **2015**, *11*, 555-558.

(56) Axtell, R. C.; de Jong, B. A.; Boniface, K.; van der Voort, L. F.; Bhat, R.; De Sarno, P.; Naves, R.; Han, M.; Zhong, F.; Castellanos, J. G.; Mair, R.; Christakos, A.; Kolkowitz, I.; Katz, L.; Killestein, J.; Polman, C. H.; de Waal Malefyt, R.; Steinman, L.; Raman, C., T Helper Type 1 and 17 Cells Determine Efficacy of Interferon-β in Multiple Sclerosis and Experimental Encephalomyelitis. *Nature Medicine* **2010**, *16*, 406-214.

(57) Fedeles, B. I.; Freudenthal, B. D.; Yau, E.; Singh, V.; Chang, S.; Li, D.; Delaney, J. C.; Wilson, S. H.; Essigmann, J. M., Intrinsic Mutagenic Properties of 5-Chlorocytosine: A Mechanistic Connection between Chronic Inflammation and Cancer. *Proc. Natl. Acad. Sci. U.S.A. (PNAS)* **2015**, *112*, E4571-E4580.

(58) Gamow, G., Quantum Theory of Atomic Nuclei. *Z. Phys.* **1928**, *51*, 204.

(59) Siegert, A. J. F., On the Derivation of the Dispersion Formula for Nuclear Reactions. *Phys. Rev.* **1939**, *56*, 750.

(60) Santra, R.; Cederbaum, L. S.; Meyer, H.-D., Electronic Decay of Molecular Clusters: Non-Stationary States Computed by Standard Quantum Chemistry Methods. *Chem. Phys. Lett.* **1999**, *303*, 413-419.

(61) Hirao, K., Direct Cluster-Expansion Method - Application to Glyoxal. *J. Chem. Phys.* **1983**, *79*, 5000-5010.

(62) Nakatsuji, H.; Ehara, M., Symmetry-Adapted Cluster-Configuration Interaction Study on the Excited and Ionized States of $TiBr_4$ and TiI_4. *J. Chem. Phys.* **1994**, *101*, 7658-7671.

(63) Krause, P.; Sonk, J. A.; Schlegel, H. B., Strong-Field Ionization Rates of Linear Polyenes Simulated with Time-Dependent Configuration Interaction with an Absorbing Potential. *J. Chem. Phys.* **2014**, *140*, 174113.

(64) Krause, P.; Schlegel, H. B., Angle-Dependent Ionization of Hydrides AH(n) Calculated by Time-Dependent Configuration Interaction with an Absorbing Potential. *J. Phys. Chem. A* **2015**, *119*, 10212-10220.

(65) Dunning, Jr, T. H., Gaussian-Basis Sets for Use in Correlated Molecular Calculations .1. The Atoms Boron through Neon and Hydrogen. *J. Chem. Phys.* **1989**, *90*, 1007-1023.

(66) Fukuda, R.; Nakatsuji, H., Formulation and Implementation of Direct Algorithm for the Symmetry-Adapted Cluster and Symmetry-Adapted Cluster-Configuration Interaction Method. *J. Chem. Phys.* **2008**, *128*, 094105.

(67) Nakatsuji, H., Cluster-Expansion of the Wavefunction - Valence and Rydberg Excitations, Ionizations, and Inner-Valence Ionizations of CO_2 and N_2O Studied by the SAC and SAC CI Theories. *Chem. Phys.* **1983**, *75*, 425-441.

(68) Fukuda, R.; Ehara, M., Efficiency of Perturbation-Selection and its Orbital Dependence in the SAC-CI Calculations for Valence Excitations of Medium-Size Molecules. *J. Comput. Chem.* **2014**, *35*, 2163-2176.

(69) Frisch, M. J.; Trucks, G. W.; Schlegel, H. B.; Scuseria, G. E.; Robb, M. A.; Cheeseman, J. R.; Scalmani, G.; Barone, V.; Mennucci, B.; Petersson, G. A.; Nakatsuji, H.; Caricato, M.; Li, X.; Hratchian, H. P.; Izmaylov, A. F.; Bloino, J.; Zheng, G.; Sonnenberg, J. L.; Hada, M.; Ehara, M.; Toyota, K.; Fukuda, R.; Hasegawa, J.; Ishida, M.; Nakajima, T.; Honda, Y.; Kitao, O.; Nakai, H.; Vreven, T.; Montgomery, Jr., J. A.; Peralta, J. E.; Ogliaro, F.; Bearpark, M.; Heyd, J. J.; Brothers, E.; Kudin, K. N.; Staroverov, V. N.; Keith, T.; Kobayashi, R.; Normand, J.; Raghavachari, K.; Rendell, A.; Burant, J. C.; Iyengar, S. S.; Tomasi, J.; Cossi, M.; Rega, N.; Millam, J. M.; Klene, M.; Knox, J. E.; Cross, J. B.; Bakken, V.; Adamo, C.; Jaramillo, J.; Gomperts, R.; Stratmann, R. E.; Yazyev, O.; Austin, A. J.; Cammi, R.; Pomelli, C.; Ochterski, J. W.; Martin, R. L.; Morokuma, K.; Zakrzewski, V. G.; Voth, G. A.; Salvador, P.; Dannenberg, J. J.; Dapprich, S.; Daniels, A. D.; Farkas, O.; Foresman, J. B.; Ortiz, J. V.; Cioslowski, J.; Fox, D. J., *GAUSSIAN09 Rev. B.01*. Gaussian Inc.: Wallingford CT, 2010.

(70) Burrow, P. D.; Gallup, G. A.; Scheer, A. M.; Denifl, S.; Ptasinska, S.; Mark, T.; Scheier, P., Vibrational Feshbach Resonances in Uracil and Thymine. *J. Chem. Phys.* **2006**, *124*, 124310.

(71) Burrow, P. D.; Michejda, J. A., Electron Transmission Study of Formaldehyde Electron-Affinity. *Chem. Phys. Lett.* **1976**, *42*, 223-226.

(72) Jordan, K. D.; Burrow, P. D., Temporary Anion States of Polyatomic Hydrocarbons. *Chem. Rev.* **1987**, *87*, 557-588.

(73) Jang, Y. H.; Goddard III, W. A.; Noyes, K. T.; Sowers, L. C.; Hwang, S.; Chung, D. S., pKa Values of Guanine in Water: Density Functional Theory Calculations Combined with Poisson-Boltzmann Continuum - Solvation Model. *J. Phys. Chem. B* **2003**, *107*, 344-357.
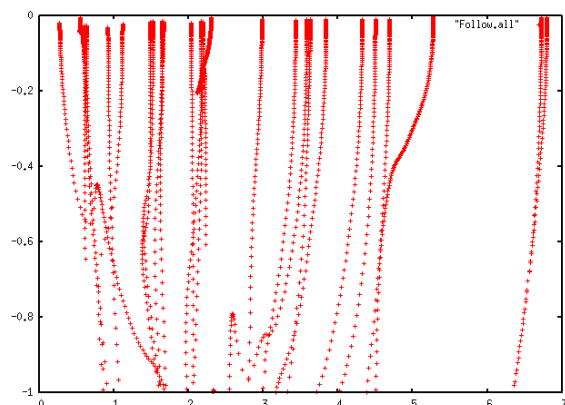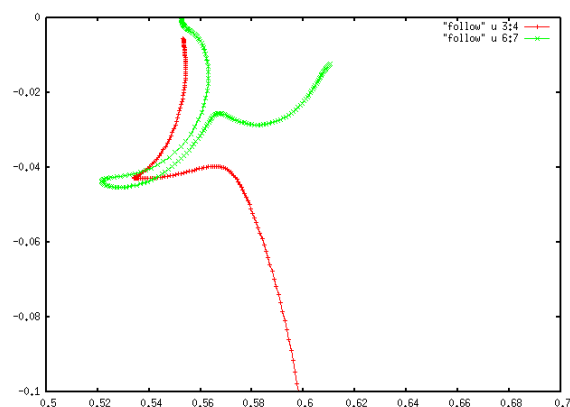
Supporting Information

Uracil   Thymine   Cytosine   Methylcytosine   Formylcytosine   Chlorocytosine

Guanine (keto)   Guanine (enol)   Adenine

In all Figures, horizontal axis is Re(E) and vertical axis is Im(E) in the complex plane in eV.
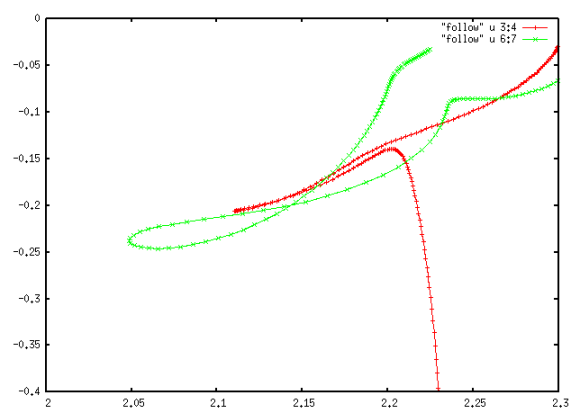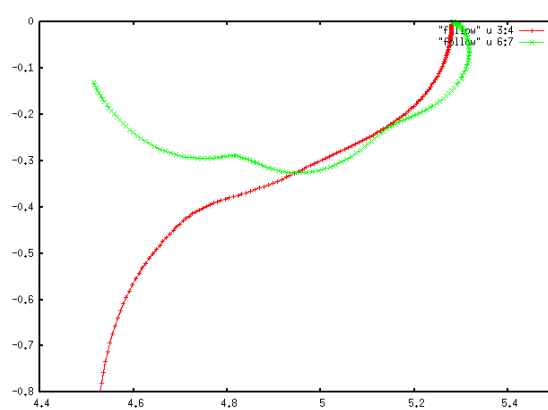
Uracil

(a) All uncorrected trajectories
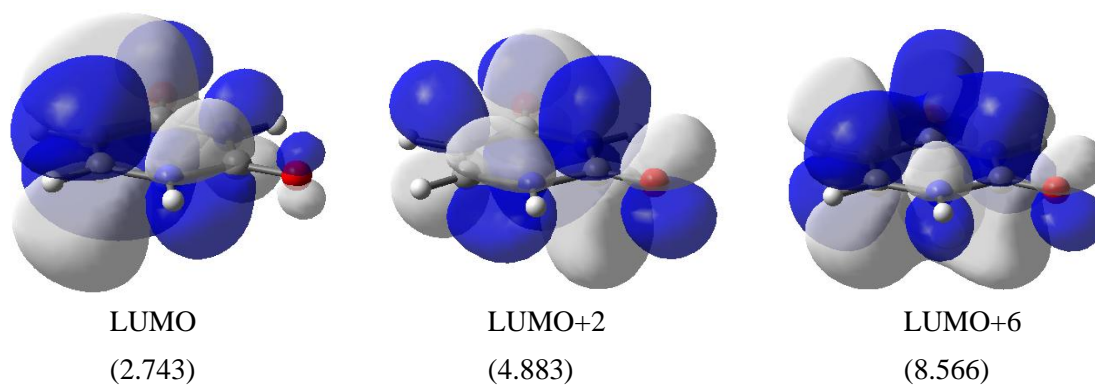
(b) π_1* resonance

(c) π_2* resonance

(d) π_3* resonance

Figure 4.S1. (a) All uncorrected trajectories, (b-d) corrected (green) and uncorrected (red) η-trajectories for the π_1*, π_2*, and π_3* resonance states of Uracil (A″, 348 AOs) by the projected CAP/SAC-CI with smooth Voronoi potential (r_{cut}=4.0, boxpara=1.0, cc-pVDZ+[2s5p2d], N_{sol}=30, Lv3).

MOs for electron attachment in Uracil (Orbital energy with cc-pVDZ in eV)

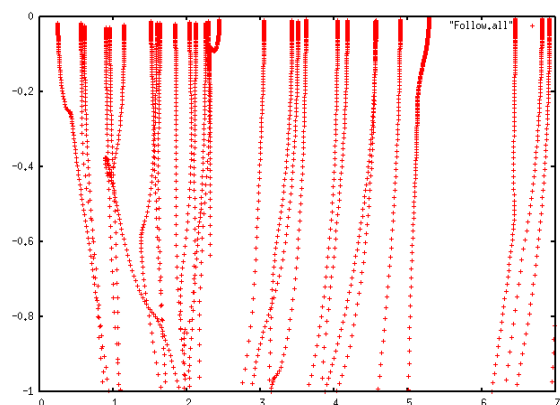| LUMO	LUMO+2	LUMO+6
(2.743)	(4.883)	(8.566)

Table 4.S1. Resonance position and width (eV) of the π^* resonance states of Uracil calculated by the projected CAP/SAC-CI with smooth Voronoi potential. Corrected and uncorrected trajectories were used.

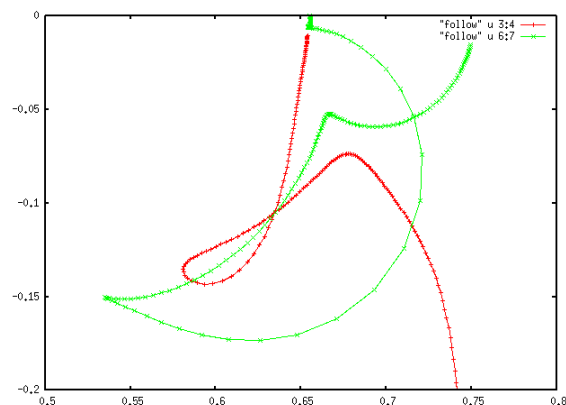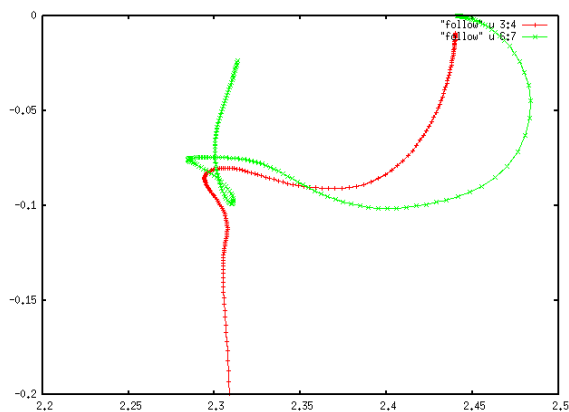| State (No.)	Expt.[a]	CAP/SAC-CI			
		corrected		uncorrected	
		Re(E)	–Im(E)	Re(E)	–Im(E)
π_1^* (2)	0.22	0.566	0.026	0.570	0.040
π_2^* (14)	1.58	2.210	0.049	2.203	0.140
π_3^* (23)	3.83	4.825	0.291	4.748	0.402

[a] Aflatooni et al. in Ref. [6].

Thymine

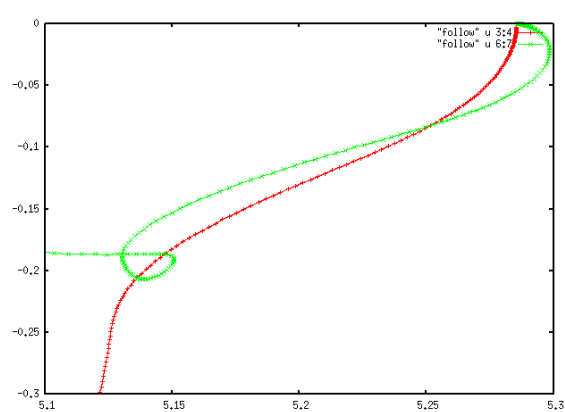(a) All uncorrected trajectories

(b) $\pi_1{}^*$ resonance
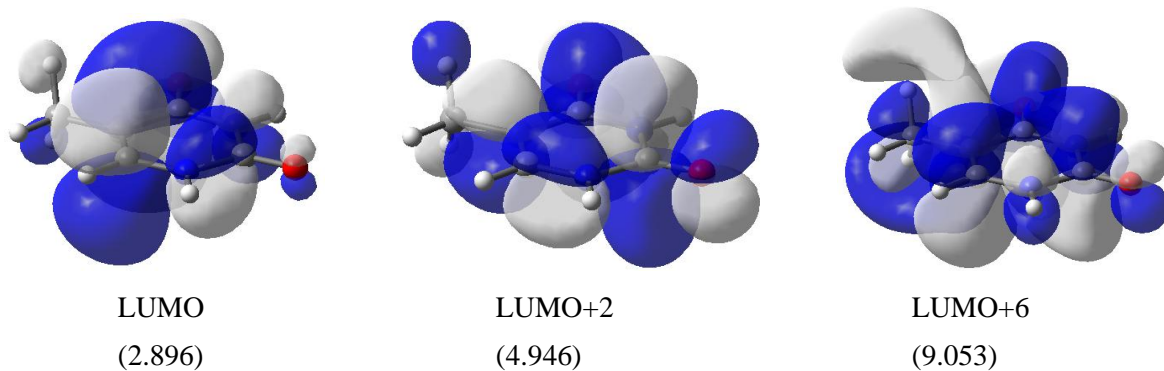
(c) $\pi_2{}^*$ resonance

(d) $\pi_3{}^*$ resonance

Figure 4.S2. (a) All uncorrected trajectories, (b-d) corrected (green) and uncorrected (red) η-trajectories for the $\pi_1{}^*$, $\pi_2{}^*$, and $\pi_3{}^*$ resonance states of Thymine (A″, 399 AOs) by the projected CAP/SAC-CI with smooth Voronoi potential (r_{cut}=4.0, boxpara=1.0, cc-pVDZ+[2s5p2d], N_{sol}=30, Lv3).

MOs for electron attachment in Thymine (Orbital energy with cc-pVDZ in eV)

LUMO	LUMO+2	LUMO+6
(2.896)	(4.946)	(9.053)

Table 4.S2. Resonance position and width (eV) of the π^* resonance states of Thymine calculated by the projected CAP/SAC-CI with smooth Voronoi potential. Corrected and uncorrected trajectories were used.

State (No.)	Expt.[a]	CAP/SAC-CI			
		corrected		uncorrected	
		Re(E)	−Im(E)	Re(E)	−Im(E)
π_1^* (4)	0.29	0.666	0.053	0.678	0.074
π_2^* (15)	1.71	2.284	0.076	2.294	0.085
π_3^* (25)	4.05	5.137	0.206	5.127	0.237

[a] Aflatooni et al. in Ref. [6].

Cytosine

(a) All uncorrected trajectories

(b) π_1^* resonance

(c) π_2^* resonance

(d) π_3^* resonance

Figure 4.S3. (a) All uncorrected trajectories, (b-d) corrected (green) and uncorrected (red) η-trajectories for the π_1^*, π_2^*, and π_3^* resonance states of Cytosine (A″, 399 AOs) by the projected CAP/SAC-CI with smooth Voronoi potential (r_{cut}=4.0, boxpara=1.0, cc-pVDZ+[2s5p2d], N_{sol}=30, Lv3).

MOs for electron attachment in Cytosine (Orbital energy with cc-pVDZ in eV)

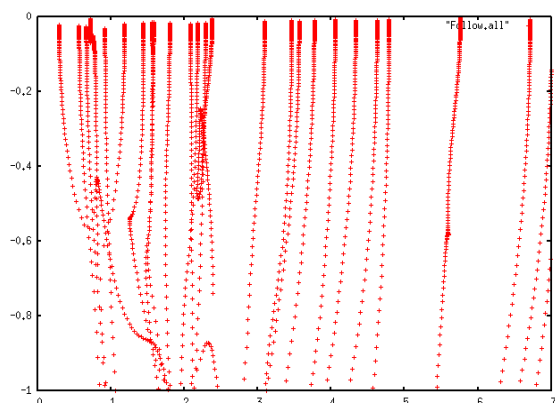| LUMO	LUMO+1	LUMO+5
(3.075)	(5.108)	(9.476)

Table 4.S3. Resonance position and width (eV) of the π^* resonance states of Cytosine calculated by the projected CAP/SAC-CI with smooth Voronoi potential. Corrected and uncorrected trajectories were used.

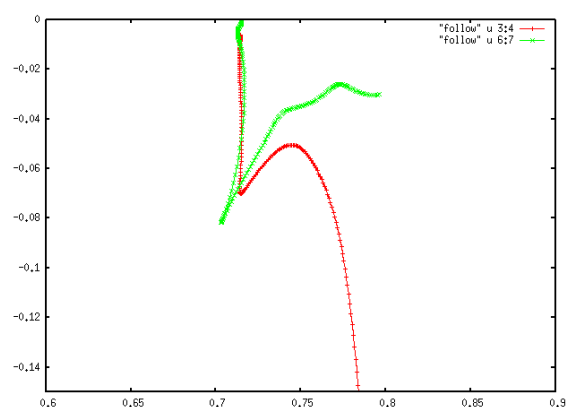| State (No.)	Expt.[a]	CAP/SAC-CI			
		corrected		uncorrected	
		Re(E)	$-$Im(E)	Re(E)	$-$Im(E)
π_1^* (4)	0.32	0.703	0.082	0.715	0.070
π_2^* (14)	1.53	2.177	0.151	2.221	0.246
π_3^* (23)	4.50	5.660	0.315	5.599	0.582

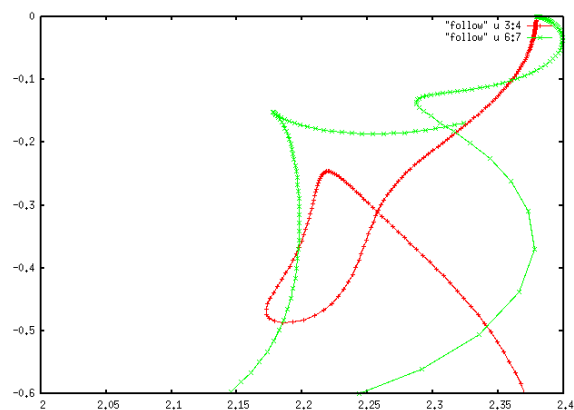[a] Aflatooni et al. in Ref. [6].

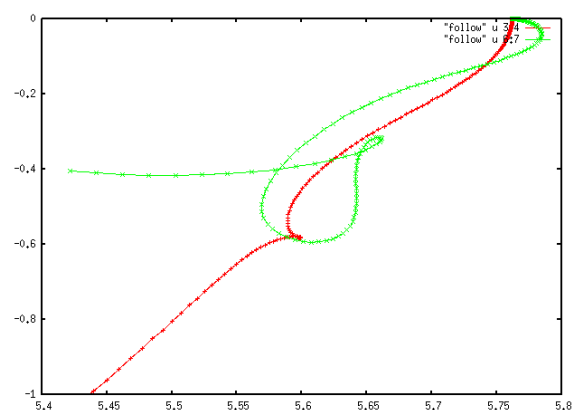**5-Methylcytosine**

(a) All uncorrected trajectories
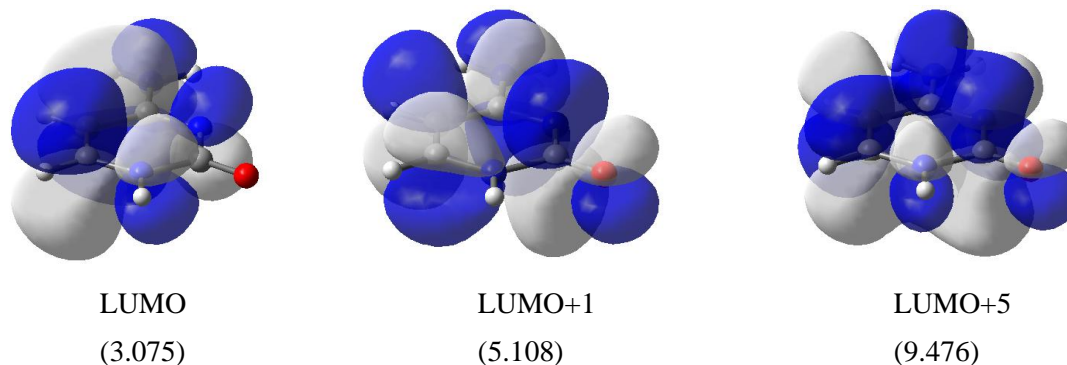
(b) π_1* resonance

(c) π_2* resonance

(d) π_3* resonance

Figure 4.S4. (a) All uncorrected trajectories, (b-d) corrected (green) and uncorrected (red) η-trajectories for the π_1*, π_2*, and π_3* resonance states of Formylcytosine (A″, 435 AOs) by the projected CAP/SAC-CI with smooth Voronoi potential (r_{cut}=4.0, boxpara=1.0, cc-pVDZ+[2s5p2d], N_{sol}=30, Lv3).

MOs for electron attachment in Methylcytosine (Orbital energy with cc-pVDZ in eV)

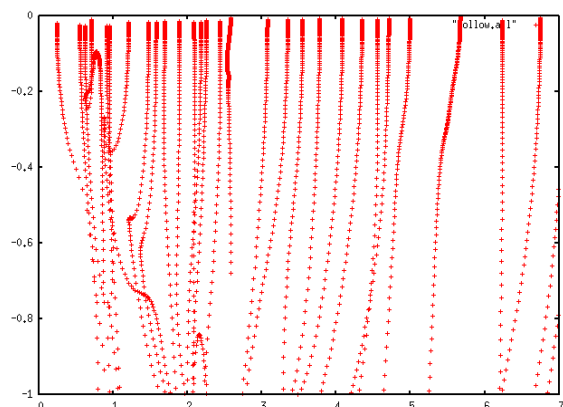| LUMO	LUMO+1	LUMO+5
(3.154)	(5.132)	(9.775)

Table 4.S4. Resonance position and width (eV) of the π^* resonance states of Methylcytosine calculated by the projected CAP/SAC-CI with smooth Voronoi potential. Corrected and uncorrected trajectories were used.

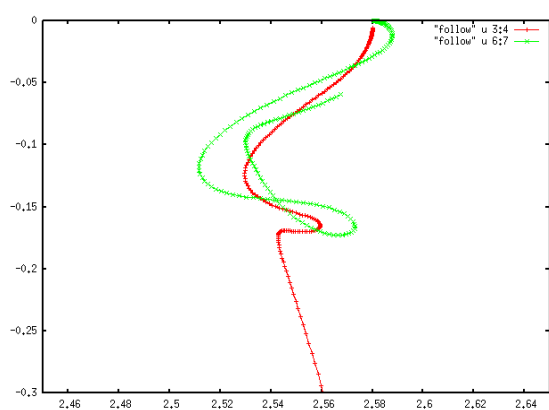| State	CAP/SAC-CI			
(No.)	corrected		uncorrected	
	Re(E)	−Im(E)	Re(E)	−Im(E)
π_1^* (4)	0.740	0.087	0.764	0.095
π_2^* (16)	2.571	0.172	2.559	0.166
π_3^* (26)	5.435	0.164	5.498	0.285

5-Formylcytosine

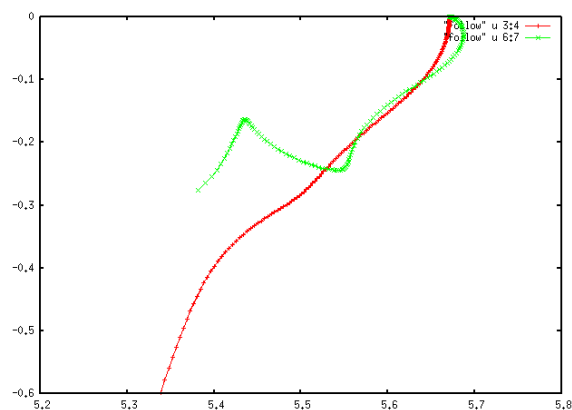(a) All uncorrected trajectories
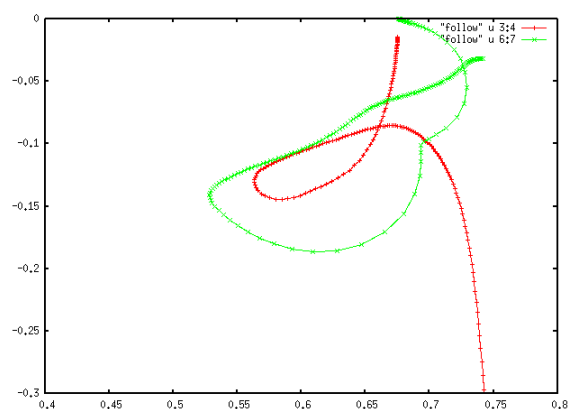
(b) π_1^* resonance
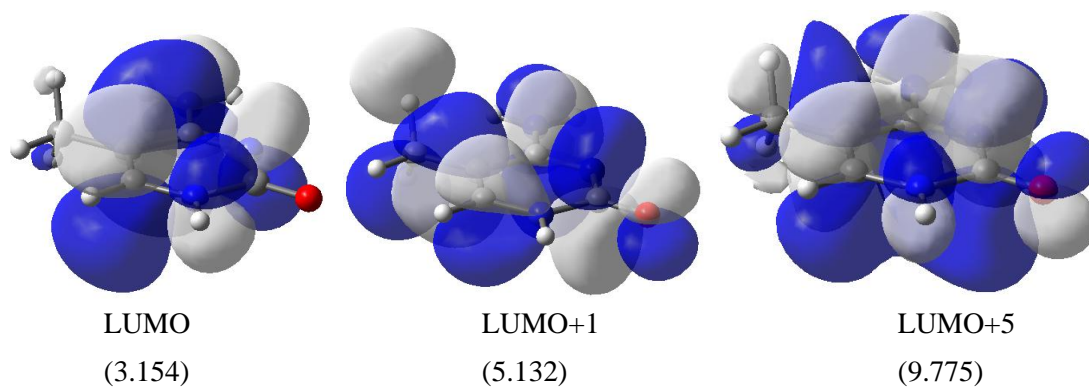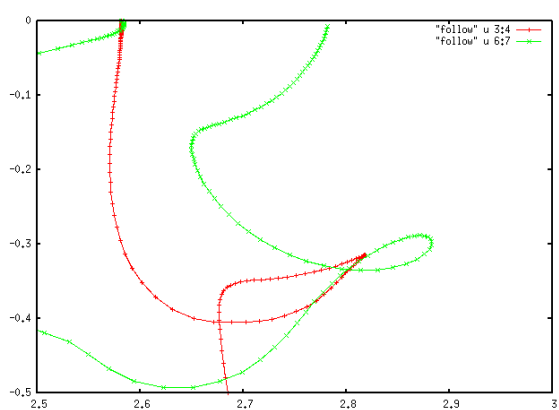

(c) π_2^* resonance

(d) π_3^* resonance

Figure 4.S5. (a) All uncorrected trajectories, (b-d) corrected (green) and uncorrected (red) η-trajectories for the π_1^*, π_2^*, and π_3^* resonance states of Formylcytosine (A″, 435 AOs) by the projected CAP/SAC-CI with smooth Voronoi potential (r_{cut}=4.0, boxpara=1.0, cc-pVDZ+[2s5p2d], N_{sol}=30, Lv3).

MOs for electron attachment in Formylcytosine (Orbital energy with cc-pVDZ in eV)

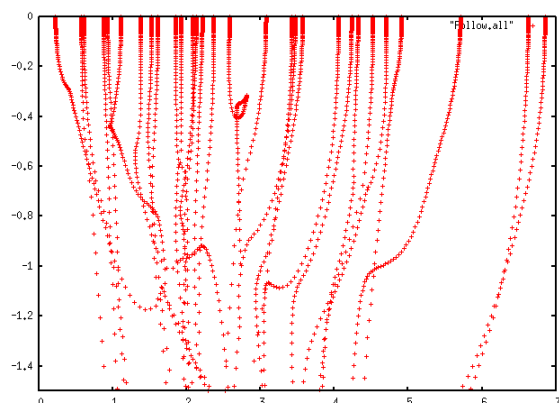| LUMO | LUMO+1 | LUMO+5 |
| (2.030) | (3.362) | (5.924) |

Table 4.S5. Resonance position and width (eV) of the π^* resonance states of Formylcytosine calculated by the projected CAP/SAC-CI with smooth Voronoi potential. Corrected and uncorrected trajectories were used.

| State | CAP/SAC-CI | | | |
| (No.) | corrected | | uncorrected | |
	Re(E)	$-$Im(E)	Re(E)	$-$Im(E)
π_1^* (5)	0.529	0.139	0.564	0.127
π_2^* (17)	2.654	0.151	2.688	0.355
π_3^* (27)	4.847	0.115	–	–

π_1^* was obtained in the different orientation of C=O group.

5-Chlorocytosine

(a) All uncorrected trajectories
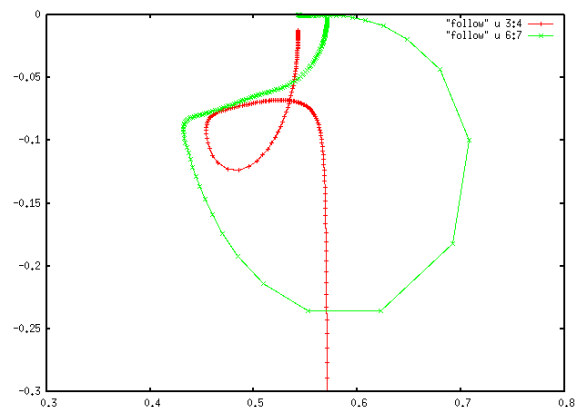
(b) π_1^* resonance
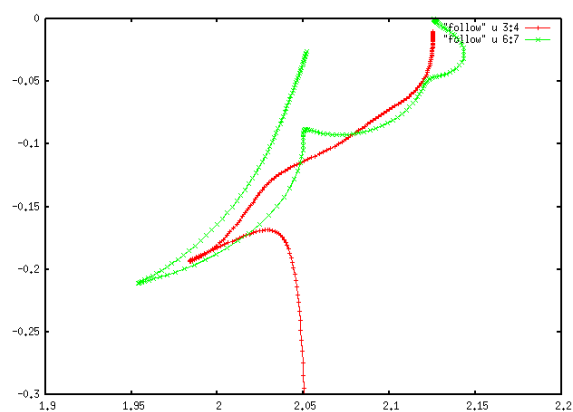
(c) π_2^* resonance

(d) π_3^* resonance

Figure 4.S6. (a) All uncorrected trajectories, (b-d) corrected (green) and uncorrected (red) η-trajectories for the π_1^*, π_2^*, and π_3^* resonance states of Formylcytosine (A$''$, 435 AOs) by the projected CAP/SAC-CI with smooth Voronoi potential (r_{cut}=4.0, boxpara=1.0, cc-pVDZ+[2s5p2d], N_{sol}=30, Lv3).

MOs for electron attachment in Chlorocytosine (Orbital energy with cc-pVDZ in eV)

LUMO	LUMO+2	LUMO+7
(2.628)	(4.764)	(9.147)

Table 4.S6. Resonance position and width (eV) of the π^* resonance states of Chlorocytosine calculated by the projected CAP/SAC-CI with smooth Voronoi potential. Corrected and uncorrected trajectories were used.

State (No.)	CAP/SAC-CI			
	corrected		uncorrected	
	Re(E)	–Im(E)	Re(E)	–Im(E)
π_1^* (2)	0.434	0.085	0.459	0.081
π_2^* (12)	2.051	0.088	1.984	0.193
π_3^* (25)	5.346	0.190	5.247	0.743

Guanine (keto)

(a) All uncorrected trajectories
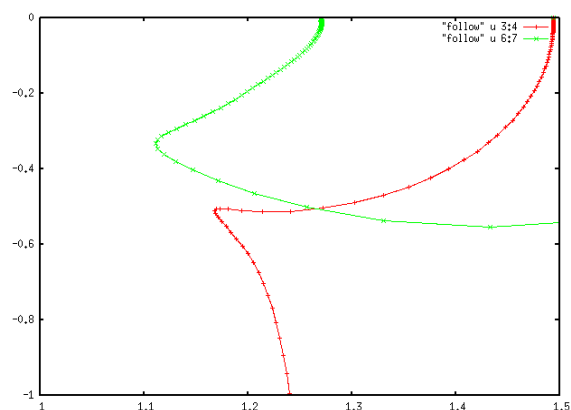
(b) π_1^* resonance
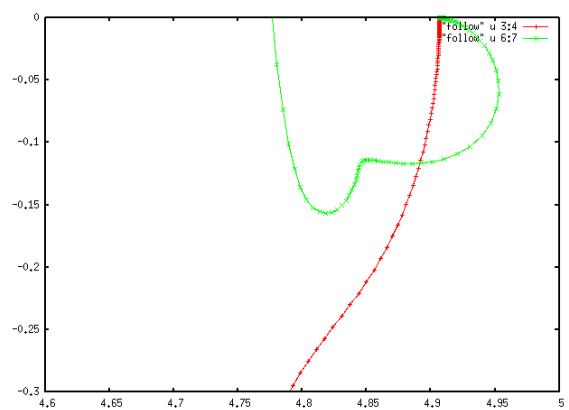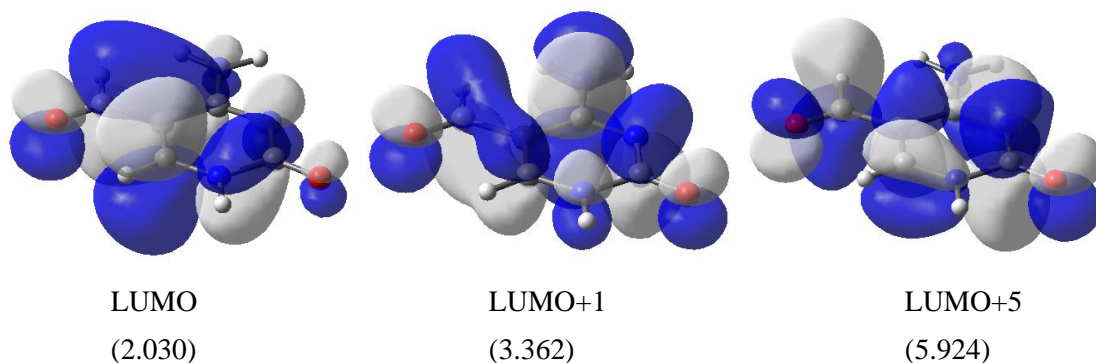

(c) π_2^* resonance
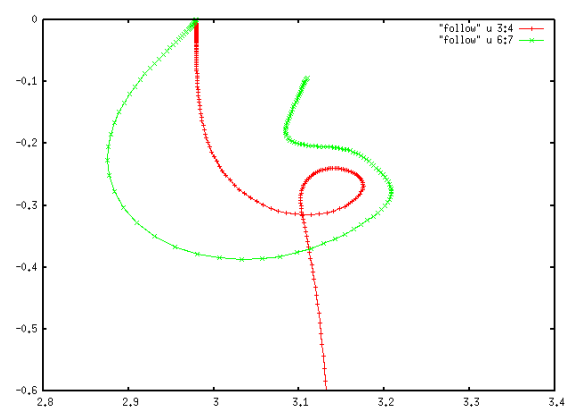
(d) π_3^* resonance

(e) π_4^* resonance

Figure 4.S7. (a) All uncorrected trajectories, (b-e) corrected (green) and uncorrected (red) η-trajectories for the π_1^*, π_2^*, π_3^* and π_4^* resonance states of Guanine (keto) (A″, 476 AOs) by the projected CAP/SAC-CI with smooth Voronoi potential (r_{cut}=4.0, boxpara=1.0, cc-pVDZ+[2s5p2d], N_{sol}=40, Lv3).

MOs for electron attachment in Guanine (keto) (Orbital energy with cc-pVDZ in eV)

LUMO+1
(4.150)

LUMO+2
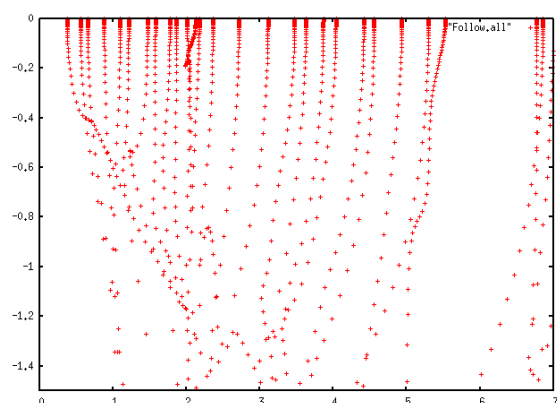(4.451)

LUMO+5
(5.991)

LUMO+9
(10.260)

Table 4.S7. Resonance position and width (eV) of the π^* resonance states of Guanine (keto) calculated by the projected CAP/SAC-CI with smooth Voronoi potential. Corrected and uncorrected trajectories were used.

State	Expt.[a]	CAP/SAC-CI			
(No.)		corrected		uncorrected	
		Re(E)	−Im(E)	Re(E)	−Im(E)
π_1^* (6)	0.46	1.114	0.320	1.169	0.507
π_2^* (9)	1.37	1.663	0.168	1.654	0.161
π_3^* (18)	2.36	3.208	0.274	3.172	0.256
π_4^* (30)	–	6.495	0.461	–	–

[a] Aflatooni et al. in Ref. [6].

Guanine (enol)

(a) All uncorrected trajectories
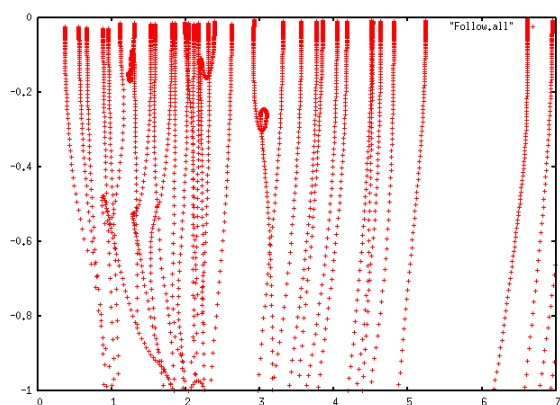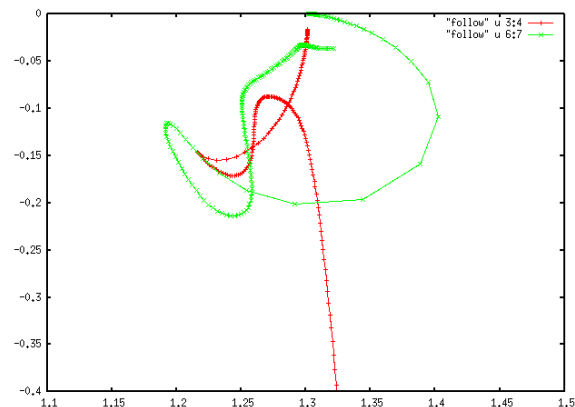
(b) π_1^* resonance
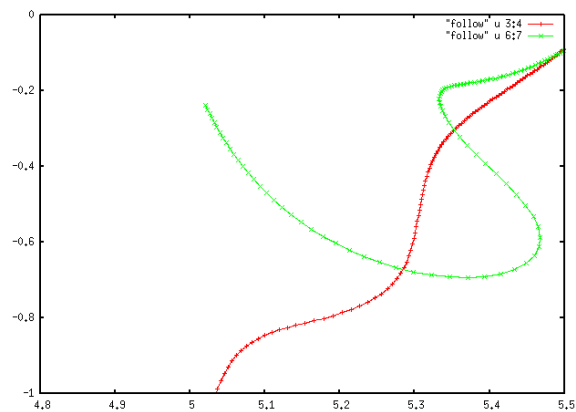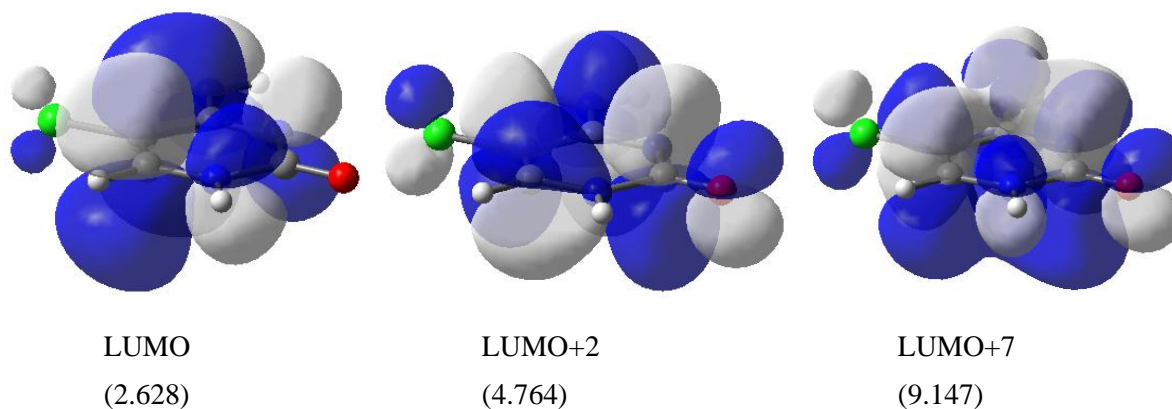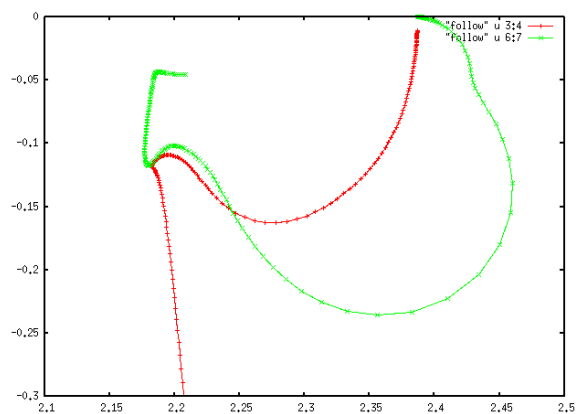

(c) π_2^* resonance
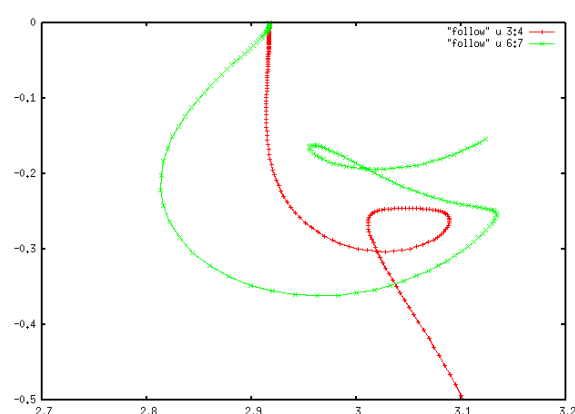
(d) π_3^* resonance
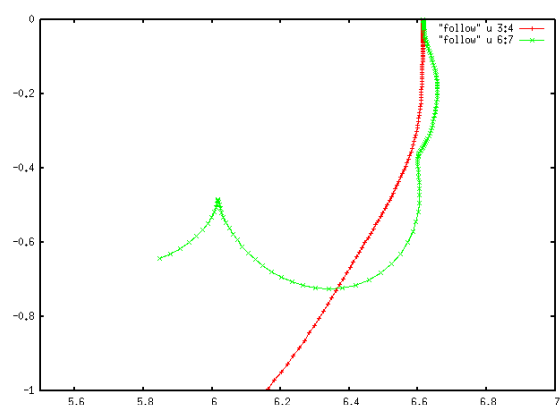
(e) π_4^* resonance

Figure 4.S8. (a) All uncorrected trajectories, (b-d) corrected (green) and uncorrected (red) η-trajectories for the π_1^*, π_2^*, π_3^* and π_4^* resonance states of Guanine (enol) (A″, 476 AOs) by the projected CAP/SAC-CI with smooth Voronoi potential (r_{cut}=4.0, boxpara=1.0, cc-pVDZ+[2s5p2d], N_{sol}=40, Lv3).

MOs for electron attachment in Guanine (enol) (Orbital energy with cc-pVDZ in eV)

LUMO
(3.715)

LUMO+1
(4.774)
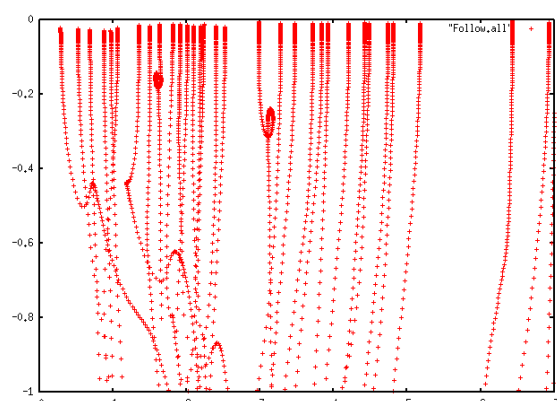
LUMO+5
(5.981)

LUMO+9
(10.623)
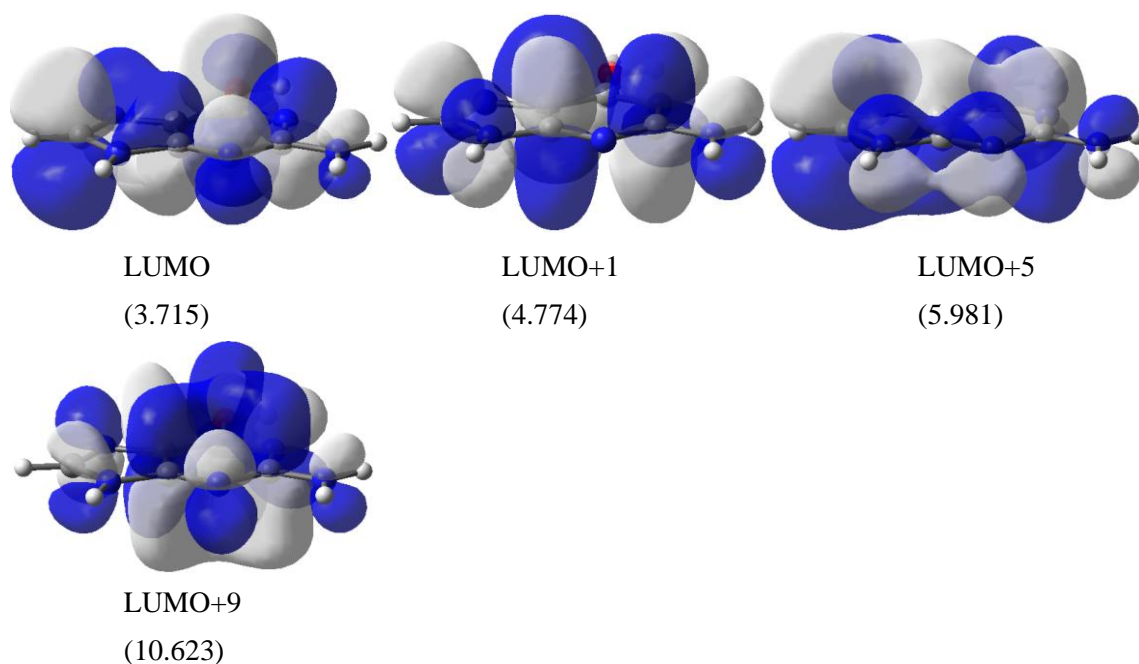
Table 4.S8. Resonance position and width (eV) of the π^* resonance states of Guanine (enol) calculated by the projected CAP/SAC-CI with smooth Voronoi potential. Corrected and uncorrected trajectories were used.

State (No.)	Expt.[a]	CAP/SAC-CI			
		corrected		uncorrected	
		$\mathrm{Re}(E)$	$-\mathrm{Im}(E)$	$\mathrm{Re}(E)$	$-\mathrm{Im}(E)$
π_1^* (7)	0.46	1.256	0.075	1.269	0.088
π_2^* (17)	1.37	2.186	0.044	2.182	0.119
π_3^* (19)	2.36	3.134	0.252	3.087	0.255
π_4^* (31)	–	6.605	0.358	–	–

[a] Aflatooni et al. in Ref. [6].
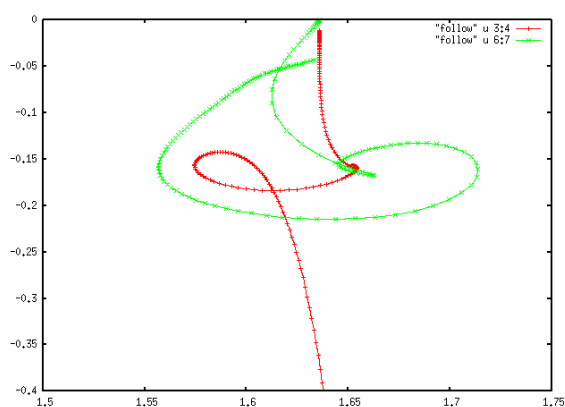
Adenine

(a) All uncorrected trajectories
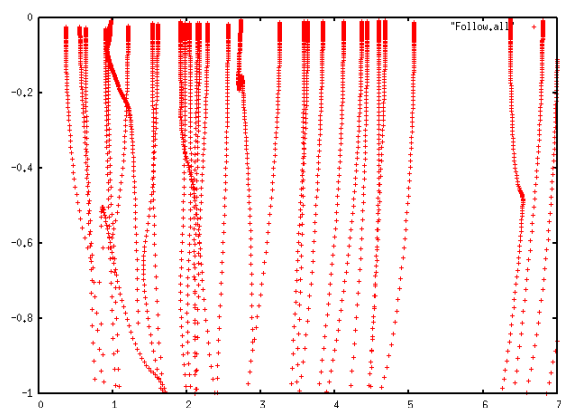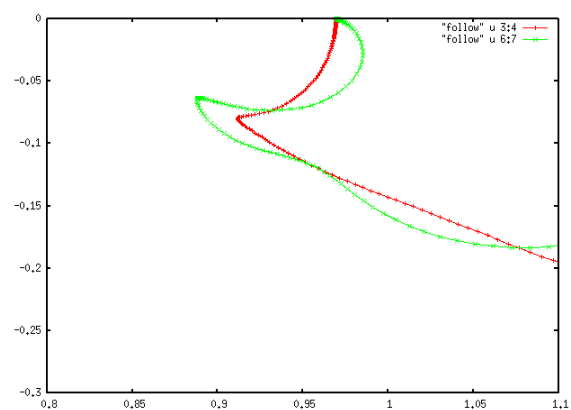
(b) π_1^* resonance
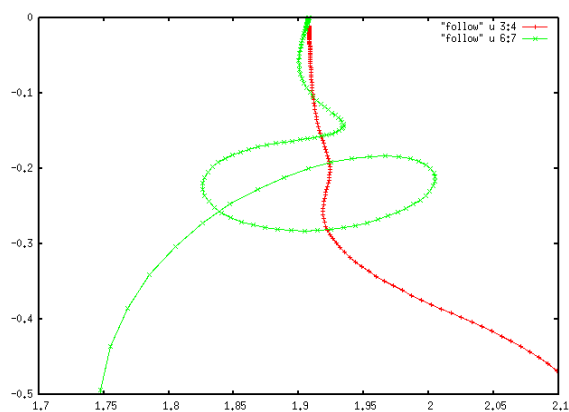
(c) π_2^* resonance
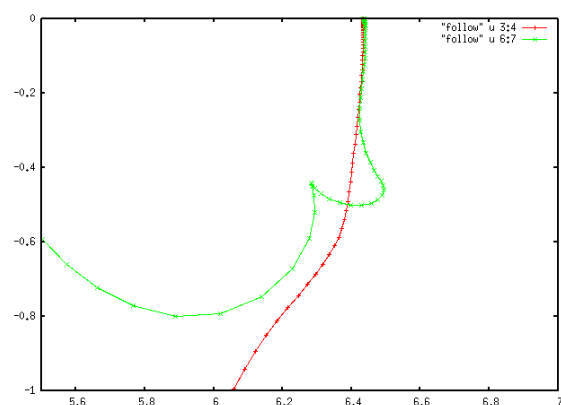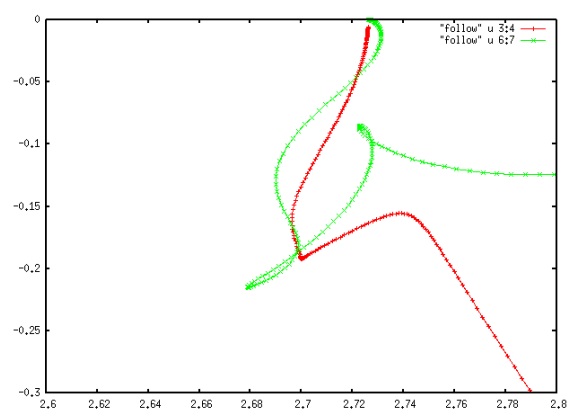

(d) π_3^* resonance
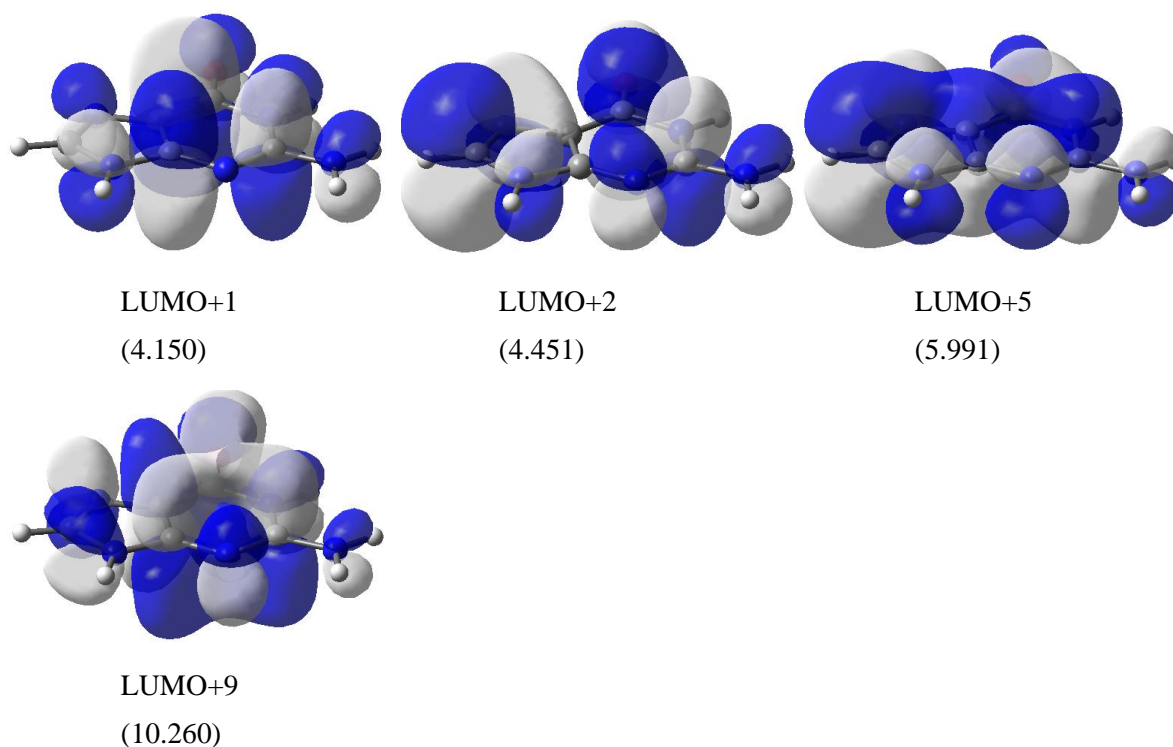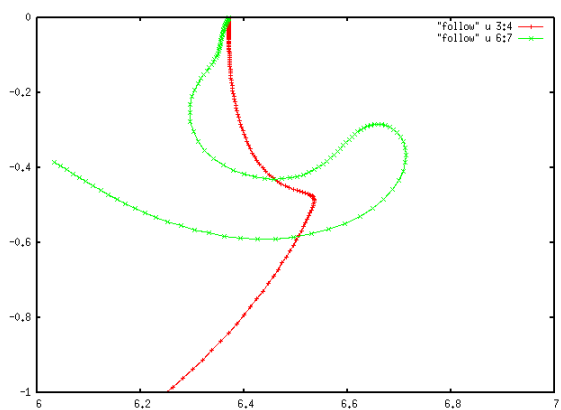

(e) π_4^* resonance

Figure 4.S9. (a) All uncorrected trajectories, (b-e) corrected (green) and uncorrected (red) η-trajectories for the π_1^*, π_2^*, π_3^* and π_4^* resonance states of Adenine (A″, 476 AOs) by the projected CAP/SAC-CI with smooth Voronoi potential (r_{cut}=4.0, boxpara=1.0, cc-pVDZ+[2s5p2d], N_{sol}=40, Lv3).

MOs for electron attachment in Adenine (Orbital energy with cc-pVDZ in eV)

LUMO	LUMO+1	LUMO+5
(3.547)	(4.403)	(5.723)

LUMO+9

(10.480)
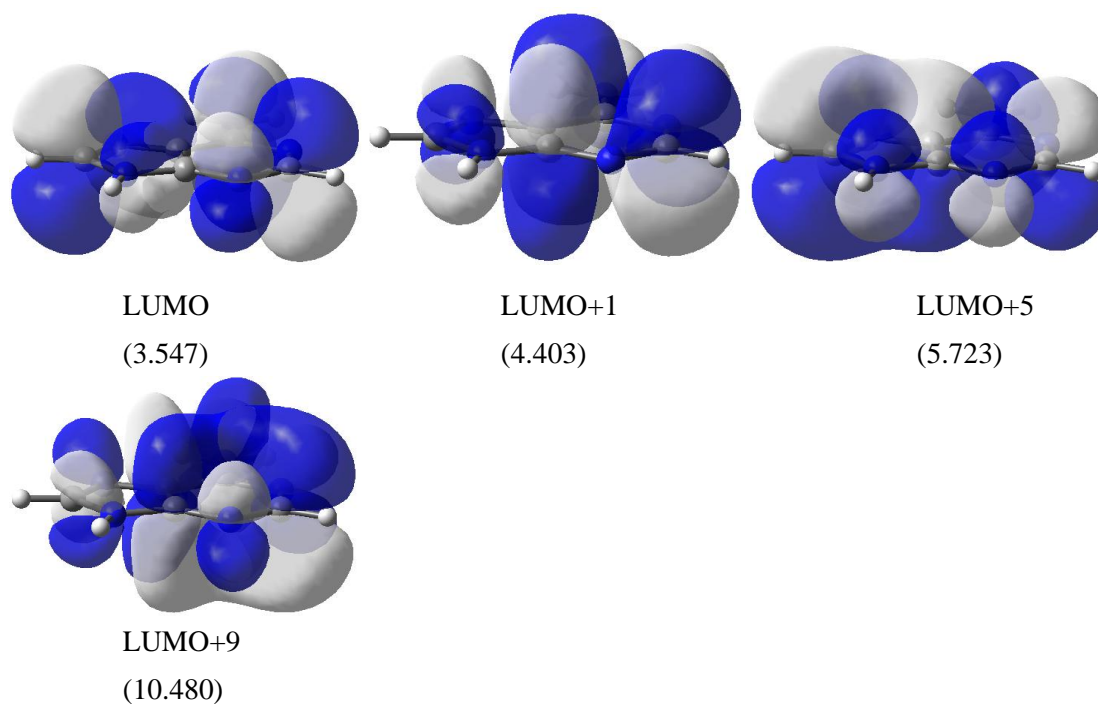
Table 4.S9. Resonance position and width (eV) of the π^* resonance states of Adenine calculated by the projected CAP/SAC-CI with smooth Voronoi potential. Corrected and uncorrected trajectories were used.

State	Expt.[a]	CAP/SAC-CI			
(No.)		corrected		uncorrected	
		Re(E)	$-$Im(E)	Re(E)	$-$Im(E)
π_1^* (6)	0.54	0.889	0.064	0.912	0.080
π_2^* (10)	1.36	1.934	0.143	1.924	0.201
π_3^* (17)	2.17	2.723	0.086	2.740	0.156
π_4^* (28)	–	6.652	0.285	6.534	0.478

[a] Aflatooni et al. in Ref. [6].

Chapter 5

Low-lying π* Resonances Associated with Cyano Groups: A CAP/SAC-CI Study

The author applied the complex absorbing potential (CAP)/symmetry-adapted cluster-configuration interaction (SAC-CI) method to low-lying π* resonance states of molecules containing one or two cyano (CN) groups. Benchmark calculations are carried out comparing the non-variational and approximate variational approach of SAC-CI and studying the selection threshold of operators. Experimental resonance positions from electron transmission spectroscopy (ETS) are reproduced provided the anticipated deviations due to vibronic effects are taken into account. Moreover, the calculated positions and widths agree well with those obtained in previous electron scattering calculations for HCN, CH_3CN and their isonitriles. Based on our results, the author suggests a reassignment of the experimental ETS of fumaronitrile and malononitrile. Our present results demonstrate again that the CAP/SAC-CI method reliably predicts low-lying π* resonances, and regarding the total numbers of molecules and resonances investigated, it is fair to say that it is presently the most extensively used high-level method in the temporary anion field.

5.1. Introduction

The cyano group (C≡N) has electron withdrawing properties like halogens, however, in contrast to halogens this property is caused by its π conjugation, which makes for very different electronic properties. Two or more conjugated CN groups in a molecule can give rise to the existence of a strongly bound anion. Molecules like this show electronic properties which can be utilized as acceptors in organic conductors; examples are tetracyanoethylene (TCNE) and tetracyanoquinodimethane (TCNQ). On the other hand, a CN-containing molecule will also possess unoccupied π* orbitals whose occupation does not lead to stable but rather to metastable or so-called temporary anions. Temporary anions, or in general resonance states, are characterized by an energy, E_r, above the neutral molecule and by a width, Γ, which is inversely related to the lifetime of the state, $\tau = \hbar/\Gamma$. Temporary anion states may always be expected if there is only one CN group, if several CN groups are unconjugated, and for conjugated CN groups from higher lying π* orbitals. In other words, π* resonances will always exist, regardless of whether a nitrile or isonitrile forms a stable anion states or not, and–depending on circumstances–the metastable states will play their role in electron-capture, in electron-induced reactions, or resonance-assisted electron hopping process.

For a series of CN-group containing molecules, Burrow and Jordan et al. reported comprehensive electron transmission spectroscopy (ETS) data as well as assignments based on molecular orbital (MO) calculations (Hartree-Fock (HF)/3-21G) [1]. Specifically, resonance states of HCN, CH_3CN, malononitrile, $CH_2(CN)_2$, acrylonitrile (CH_2=CHCN), fumaronitrile (trans-dicyanoethylene), TCNE, benzonitrile, and TCNQ were characterized, and emphasis was placed on through—bond interactions between cyano groups. Moreover, the shape resonances of HCN and CH_3CN molecules have been intensively investigated by electron scattering calculations using the R-matrix method [2,3]. In these studies, higher-lying resonance states as well as temporary states of isocyanide isomers (HNC and CH_3NC) were also investigated. In the R-matrix calculations complete-active space-configuration interaction (CAS-CI) wavefunctions were used for HCN and HNC [2] and in the CI for the respective anions only one electron was allowed outside the CAS space. For CH_3CN and CH_3NC a HF ground state was used [3] and the CI for the respective anions was constructed from all 2p1h configurations, which is in the scattering literature referred to as static-exchange plus polarization (SEP) approximation. Note, however, that from an electron correlation

point of view, these anion wavefunctions describe only a small part of the dynamic correlation. If a balanced description including dynamic correlation is desired in a CI context, one needs to perform a singles-and-doubles CI for the closed-shell neutral and a multi-reference-CI for the anion based on all singles and doubles on *all* 1p configurations [4-6], that is, the anion configuration space consists of all 1p, 2p1h, and 3p2h configurations, a configuration space far beyond SEP. In contrast, SAC-CI and the equivalent EOM-CC reach the same level of correlation by taking explicitly into account the physical 1p and 2p1h configurations only; the unphysical 3p2h configurations are taken implicitly into account [6]. The potential energy surfaces of the resonance states and dissociation channels of HCN and HNC were also investigated [7]. However, to the best of our knowledge, there have been no systematic theoretical studies of the energies and lifetimes of π^* resonances associated with CN-groups with electronic structure methods, which treat dynamic electron correlation beyond second-order perturbation theory, and for the larger molecules, malononitrile, acrylonitrile and fumaronitrile no theory beyond the MO assignments of Burrow and Jordan seems to exist, that is, these lifetimes have so far been unknown.

There are several theoretical approaches for computing the energy and lifetime of resonance states of molecular anions; well-known methods include outright electron scattering methods [8-10], the CAP approach [4,11,12], the Hazi-Taylor stabilization method [4,13] and extrapolation methods in the form of the analytic continuation of the coupling constant method and its variants [14,15], and the method of complex basis functions [16-18]. Here a CAP is employed, and the author focuses on the CAP method. Each theoretical method aiming at computing resonances must somehow separate the resonance state from its embedding continuum or, in a finite basis set calculation, discretized continuum. A CAP performs this task by rotating the continuum into the complex plane where the resonance can be found as an isolated eigenvalue, while at the same time changing the boundary condition for resonance states from outgoing-wave to bound state (square integrable) [11]. As the resonance is normally not the lowest state in a calculation, and several discretized continuum states are energetically below it, a multi-root electronic structure method is necessary. This requirement naturally limits the applicable electronic structure theories to, for example, HF in the sense of Koopmans's theorem, configuration interaction, Green's function, or equation-of-motion type approaches. The CAP method has been incorporated with multi-reference configuration interaction calculations [4,19-22], Green's function methods [23,24], and coupled cluster [25-30] as well as related orbital theories [31,32]. Applications of these methods have been performed for a number metastable systems ranging from electron attachment

(for recent examples see [33-35]) and ionization, to interatomic/intermolecular Coulombic decay [36].

Here the CAP is used in combination with the symmetry-adapted cluster-configuration interaction (SAC-CI) theory [37,38] (CAP/SAC-CI) [25]. For applying the method to larger molecules in high-throughput calculations, the present CAP/SAC-CI method employs a projection scheme, that is, the CAP Hamiltonian is projected into a set of real SAC-CI vectors [25]. In a first pilot application [25], a rectangular soft-box potential [23], which was frequently used as a CAP in the past, was adopted. More recently, the collaborators of the author introduced two types of soft-box Voronoi potentials as CAPs [39,40], which have advantages in that they have the same space symmetry as the investigated molecule and wrap by construction around any complex molecular structures such as side chains of molecules or distantly placed monomers of clusters.

In a series of works, the collaborators of the author have demonstrated that the projected CAP/SAC-CI method with a soft-box smooth Voronoi potential is a highly useful protocol to investigated π^* resonances of molecules [25,26,34,39,40]. The method gave reliable results of both resonance position and widths of compounds with simple double-bonds, five- and six-membered ring heteroaromatic compounds, as well as standard and rare DNA and RNA bases. Note that these studies included not only the lowest, but typically π^* resonances up to five or six eV. Generally, the calculated resonance positions are in excellent agreement with the ETS values and reproduce the trend of substitution effects. Moreover, the calculated resonance widths also agree well with those from electron scattering calculations using the R-matrix method and wavefunctions beyond the static exchange level whenever they are available [41-43].

In this work, the author applies the projected CAP/SAC-CI method to temporary anions originating from the occupation of low-lying π^* orbitals in a series of CN-molecules, namely, HCN, HNC, CH_3CN, CH_3NC, acrylonitrile (CH_2=CHCN), fumaronitrile (NCCH=CHCN), and malononitrile (NC-CH_2-CN) as shown in Figure 5.1. Beyond the study of these systems, two methodological issues are investigated. First, in the SAC-CI calculations, non-variational (NV) and approximate variational (V) schemes are compared, and, second, benchmark calculations regarding the perturbation selection threshold for linear operators in the SAC-CI step were also systematically carried out. In the following, the author briefly outlines the projected CAP/SAC-CI theory and the specific computational details, and then discuss our results and compare them to ETS data as well as to electron scattering calculations when available.

116
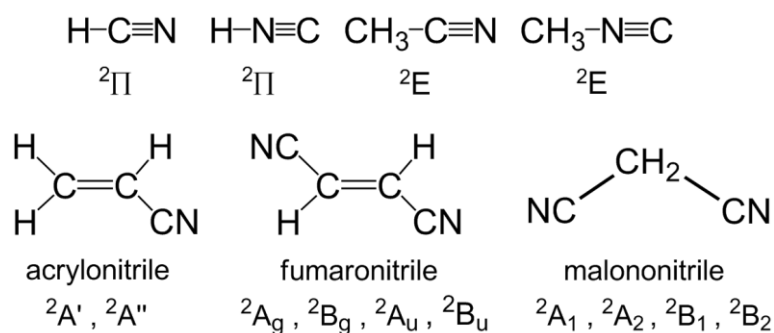
Figure 5.1. Nitriles and isonitriles studied in the present work. Below the molecules the electronic states of the investigated resonances are listed.

5.2. Theory

In order to establish some notation, the CAP method in general and the projected CAP/SAC-CI method specifically are briefly summarized. A CAP calculation provides the complex Siegert energy of a resonance [44,45],

$$E_{\mathrm{res}} = E_{\mathrm{r}} - i\,\Gamma/2, \tag{1}$$

where E_{r} and Γ, are the resonance position and width, respectively. To locate this resonance, a CAP, $-iW$, is added to the physical Hamiltonian, H, yielding a non-Hermitian, complex-symmetric Hamiltonian

$$H(\eta) = H - i\eta W, \tag{2}$$

where η is a strength parameter [46]. In this work, a soft-box smooth Voronoi CAP is used, which wraps around the molecule like a van der Waals cavity [40]. The resonance energy, E_{res}, is obtained from one of the η-trajectories of the eigenvalues of $H(\eta)$. The eigenvalue representing the resonance typically shows a pronounced stabilization (cusp, kink, or other kind of slowing-down behavior) where its η-velocity shows a minimum [46]. In addition to the trajectories themselves, one can also correct by a first-order scheme for artifacts caused by the CAP [11,12], and the author examined both the uncorrected trajectories, $E(\eta)$, and the corrected trajectories, $E(\eta) - dE(\eta)/d\ln\eta$, however, only the corrected resonance energies are reported in the main text of the paper, while the uncorrected values are reported in the Supporting Information. Note that the minimum of the "speed" of the uncorrected trajectories corresponds to the minimum of the absolute value of the derivative of the complex eigenvalue with respect to $\ln\eta$, whereas the speed of the corrected trajectories corresponds to the minimum of

the curvature of the uncorrected trajectories [23].

In the context of temporary anions, the author adopted the projected CAP/SAC-CI method [25], which has advantages for large systems due to its high throughput character. The projected CAP/SAC-CI starts from the standard electron-attachment (EA) SAC-CI method [38]. The wavefunction of an (N+1)-electron system is represented by

$$\left| \Psi_\mu^{\text{SAC-CI}} \right\rangle = R_\mu^{(N+1)} \left| \Psi_g^{\text{SAC}} \right\rangle, \tag{3}$$

where $\left| \Psi_g^{\text{SAC}} \right\rangle = \exp(\sum_I C_I S_I^\dagger) \left| \Phi_0 \right\rangle$ is the N-electron ground state SAC wavefunction and $R_\mu^{(N+1)}$ is a linear combination of the electron-attachment operators. The $S_I^\dagger$ operators are the unphysical excitation operators applied to the closed-shell Hartree-Fock $\left| \Phi_0 \right\rangle$. For temporary anions of closed-shell systems, that is shape-resonances, electron-attachment can be well described by one-electron operators and therefore, one can use the SAC-CI SD-R method [38], in which the excitation operators are limited up to singles and doubles. The higher-order operators, for example, linear 3p2h operators, would be necessary for describing Feshbach resonances.

The SAC-CI equation can be written as an equation-of-motion formula [47,48]

$$\left[H, R_\mu^{(N+1)} \right] \left| \Psi_g^{SAC} \right\rangle = \Delta E R_\mu^{(N+1)} \left| \Psi_g^{SAC} \right\rangle \tag{4}$$

where ΔE is an electron-attachment energy, in the present case $\Delta E = E_\mu^{\text{SAC-CI}} - E_g^{\text{SAC}}$. Projecting this equation to the space of $\left\langle \Phi_0 \right| R_K e^{-S}$, where $\{ R_K \}$ are the set of electron-attachment operators, one obtains the working equations,

$$\left\langle \Phi_0 \right| R_K e^{-S} \left[H, R_\mu^{(N+1)} \right] e^S \left| \Phi_0 \right\rangle = \Delta E \left\langle \Phi_0 \right| R_K R_\mu^{(N+1)} \left| \Phi_0 \right\rangle. \tag{5}$$

This is the SAC-CI NV (non-variational) equation for the electron-attached states. In addition, the author also adopted the SAC-CI-V (variational) approximation, where the SAC-CI vectors were obtained from an approximate, symmetrized SAC-CI matrix (SAC-CI-V). The SAC-CI-V is usually a good approximation to the non-symmetric SAC-CI-NV approach as examined in the previous work [25]. In addition, in a projected method [25,26] the CAP Hamiltonian as defined in Eq. (2) is expanded within a small subset of SAC-CI eigenvectors analogous to the projected CAP/CI method [21].

In the CAP approach, the crucial factor is, of course, the CAP. For simple system

like linear molecules or any other molecule that fits well into a rectangular box, the soft-box potential [46] works well. However, for molecules with three or fivefold axes and for less symmetrical systems such as molecules with side chains or molecular clusters it is less straightforward to choose a box. To overcome this problem, the collaborators of the author introduced two types of soft-box Voronoi potentials [39,40], that is, the radial dependence is still a cut off quadratic just as in the soft-box case, however, the angular dependence follows a Voronoi surface around the molecule similar to a van der Waals surface. In this work, the author specifically uses the smooth Voronoi-CAP, that avoids discontinuities at the boundaries between Voronoi cells [40]. The Voronoi-CAP has by construction the spatial symmetry of the molecular system, and, more importantly, can treat large molecules with asymmetric side chains and even molecular clusters without leaving any "dead space" between the sidechains or monomers, that is, space, which is both, poorly described by the atom centered basis set and not in the absorbing region of the CAP. Last, Voronoi CAPs use only one cutoff parameter, that is, the distance where the CAP is switched on [40]. A disadvantage is that the integrals of Voronoi CAPs must be computed numerically. A similar CAP was also adopted in the field ionization problem [49,50]. For details, readers are referred to the original articles [39,40].

5.3. Computational details

In CAP calculations, a sufficiently large number of diffuse functions needs to be included for obtaining a satisfactory stabilization of the η-trajectory of the resonance state. In the present calculations, Dunning's cc-pVTZ valence set [51] was used and augmented with a [2s5p2d] set of diffuse functions on carbon and nitrogen. The exponents of these diffuse functions have been chosen fairly close, so that an outgoing wave can be represented, yet not too close to avoid near-linear-dependency. Our [2s5p2d] set is a well-tested set fulfilling these criteria. The associated ratios for the diffuse functions are 1.5 for the 5p sets on C and N atoms, and 2 for both the s and d functions. For each atom the scaling procedure starts with the exponent of the outermost orbital in the respective valence cc-pVTZ basis set. With this basis set, the total number of basis functions ranged from 128 for HCN and HNC, over 213 for CH_3CN and CH_3NC, and 270 for acrylonitrile, to 370 for fumaronitrile, and finally 313 for malonnonitrile. Resonance energies were calculated as vertical transitions at the geometry of the neutral molecule, which was optimized with the B3LYP[52]/cc-pVTZ

[51] method.

The electron-attachment (EA) SAC-CI SD-R calculations were performed with the direct algorithm [53,54], where all the product terms are included. To reduce the computational cost, the author employed the perturbation selection procedure for both R and S double excitation/electron-attachment operators [55]. In the present work, the projected CAP/SAC-CI calculations were carried out in both NV and V scheme. The benchmark calculations with respect to energy threshold for selecting operators were also done; namely, "LevelThree" (Lv3) to "LevelFive" (Lv5) accuracy with the energy thresholds of $\lambda_g = 1 \times 10^{-6}(\text{Lv3}) - 1 \times 10^{-7}(\text{Lv5})$ and $\lambda_e = 1 \times 10^{-7}(\text{Lv3}) - 1 \times 10^{-8}(\text{Lv5})$ [54]. In the case of fumaronitrile and malonitrile, Lv3 accuracy was adopted. The SAC-CI dimensions for each molecules are summarized in Table 5.1. Recently, the collaborators of the author also performed benchmarks for the standard SAC-CI SD-R calculations regarding the level of operator selection [54].

Table 5.1

SAC/SAC-CI dimensions for HCN, CH₃CN, and acrylonitrile with cc-pVTZ + diffuse [2s5p2d]

	HCN		CH₃CN		Acrylonitrile		
	SAC	SAC-CI	SAC	SAC-CI	SAC	SAC-CI	
	$\Sigma(A_1)$	$\Pi(B_1)$	$A_1(A')$	$E(A'')$	A'	A'	A''
Lv3	19357	12204	66908	54812	126679	66454	109272
Lv4	23338	13710	98562	69595	214976	96013	141407
Lv5	31532	16125	195330	104279	523521	181300	213385
Full	49688	18331	660235	155627	1676202	342920	302494

The results depend on the selection of the CAP potential. The dependence of the cutoff parameter of the smooth Voronoi potential on the resonance energy and width was intensively examined for the double bond and heteroaromatic molecules [26,40]. When using the corrected trajectory, the results for 6 molecules and 10 resonance states were converged within about 0.01 eV for both resonance position and width comparing the values with the cutoff parameter of 3.0 and 4.0 Bohr, except for a few specific states as shown in Ref. [26]. The similar trends were observed for N_2 and H_2CO and molecular cluster of N_2 and waters [40]. Based on these calculations, in the present work, the author adopted a cutoff parameter, which is the distance between any nucleus

of the molecule and the onset of the CAP, of 4.0 Bohr, a value that was also used for the calculations of DNA and RNA bases [34].

The SAC/EA-SAC-CI and projected CAP/SAC-CI calculations were carried out using the Gaussian09 suite of programs, Revision B.01 with some modifications for the calculations of resonance states [56].

5.4. Results

5.4.1. Hydrogen Cyanide and Isocyanide

HCN is isoelectronic with N_2 and its $^2\Pi$ resonance state has been thoroughly studied [1,2,57]. The results of the projected CAP/SAC-CI from NV and V schemes with different selection thresholds are summarized in Table 5.2. Let us reiterate that the NV scheme is more accurate than the approximated V calculations. However, regarding perturbation selection, this molecule is not the best of all examples, because for this small molecule the SAC/SAC-CI dimensions of Lv3-Lv5 calculations are not significantly different (Table 5.1), and therefore all these levels provided nearly converged results. NV calculations gave 2.51-2.53 eV for the resonance position and 1.09-1.10 eV for the width, which are compared to the experimental value of 2.28 eV [1]. A small part of the deviation of 0.23-0.25 eV from the ETS value can be attributed to one and many particle basis set effects, while the largest part is probably due to vibrational effects [25]. The cc-pVTZ basis set with diffuse [2s5p2d] functions can be assumed to give nearly converged results with respect to the one particle basis sets: Previously, the effect of higher-order basis set estimated with the cc-pVQZ was found to be less than 0.03 eV for the isoelectonic molecule of H_2CO [25]. However, it is of course unclear how well the many particle basis set is converged, that would require by orders of magnitude more demanding calculations. The approximate V calculation gave a nearly identical resonance position of 2.51-2.52 eV with the width being 1.12-1.16 eV. However, in comparison with all other resonance states considered here, HCN is—for some reason—the worst case scenario regarding the stabilization of its η-trajectories, possibly due to the large resonance width. Therefore, the small changes between the different levels should not be over-interpreted, but one may think of all CAP/SAC-CI calculations for HCN to essentially agreeing with one another.

Table 5.2
Resonance position and width (eV) of the $^2\Pi$ resonance state of HCN. In the projected CAP/SAC-CI calculations a smooth Voronoi potential was used, and corrected

resonance energies are reported.

	Level	NV		V	
		E_r	Γ	E_r	Γ
CAP/SAC-CI	Lv3	2.51	1.10	2.52	1.12
	Lv4	2.51	1.09	2.51	1.14
	Lv5	2.52	1.10	2.52	1.16
	Full	2.53	1.09	2.52	1.15
Expt.[a]		2.28			
R-matrix (2007)[b]	6-31G*	3.14	1.59		
	6-311G	2.84	1.49		
	6-31G+NO[c]	2.72	1.22		
R-matrix (1985)[d]		2.56-2.80	1.78-2.40		

[a] Ref. [1],

[b] Ref. [2], CAS-CI for the target states, close-coupling expansion = at most one electron outside the CAS space

[c] orbitals obtained using separate treatment of virtual and continuum state [2]

[d] Ref. [57]

Previously, the *R*-matrix calculations using the CAS-CI method for valence electronic structure, have been performed and the resonance position and width were calculated in the range 2.72 – 3.14 eV and 1.22 – 1.59 eV depending on the basis set, which have unfortunately at best double-ζ plus polarization or triple-ζ without polarization quality [2]. The agreement with the present results in both position and width is astonishingly good considering the vastly different character of the two approaches: in the *R*-matrix and CAP/SAC-CI calculations neither the molecular geometries, nor the one-particle basis sets, nor the electron-correlation method, nor the way the continuum is handled are consistent. Another electron scattering calculation based upon the closed-coupling method gave 2.56-2.80 and 1.78-2.40 eV for the resonance position and width, respectively [57,58]: the resonance width seems to be overestimated there as pointed out in reference [2].

The results of hydrogen isocyanide (HNC) are summarized in Table 5.3 with those of the *R*-matrix calculations [2]. An experimental value is—unfortunately—unavailable. The ground state of neutral HNC was calculated at 0.62 eV above neutral HCN by B3LYP/cc-pVTZ compared to the more accurate value 0.65 eV obtained by van Mourik et al. [59]. The resonance position was found slightly higher than that of HCN at 2.77

eV.

In comparison with the *R*-matrix results [2], our calculations show a different trend regarding the order of the resonance positions of HCN and HNC. Whereas the *R*-matrix calculations in 6-31G+NO scheme using separate treatment of virtual and continuum state, predict the HCN π^* resonance position to be roughly 0.3 eV higher in energy, the CAP/SAC-CI calculation predict it to be 0.25 eV lower. Note, however, that this trend is basis-set dependent: using 6-311G, the *R*-matrix calculations gave a higher resonance position in HCN than that of HNC as listed in Tables 5.1 and 5.2. Thus, a new experiment comparing the trend of E_r for HCN *vs* HNC would be valuable to shed light on this issue. On the other hand, the resonance width calculated as 0.51 eV is close to that of *R*-matrix calculation of 0.67 eV. Again the effect of perturbation selection of the operator in SAC-CI is trivial; namely, both the resonance position and width deviate from the full calculation by only 0.01-0.03 eV in the CAP/SAC-CI NV calculations.

Table 5.3

Resonance position and width (eV) of the $^2\Pi$ resonance states of HNC. In the projected CAP/SAC-CI calculations a smooth Voronoi potential was used, and corrected resonance energies are reported.

	Level	NV		V	
		E_r	Γ	E_r	Γ
CAP/SAC-CI	Lv3	2.76	0.51	2.72	0.51
	Lv4	2.74	0.53	2.72	0.51
	Lv5	2.75	0.52	2.73	0.51
	Full	2.77	0.51	2.74	0.51
R-matrix (2007) [a]	6-31G*	3.03	1.10		
	6-311G	2.90	1.06		
	6-31G+NO[b]	2.43	0.67		

[a] Ref. [2], CAS-CI for the target states, close-coupling expansion = at most one electron outside the CAS space

[b] orbitals obtained using separate treatment of virtual and continuum state [2]

5.4.2. Acetonitrile and Isonitrile

Acetonitrile, or methylcyanide, is a derivative of HCN where a methyl group replaces the H atom. Either due to the inductive effect or due to hyper-conjugation of a

methyl group, one would expect the resonance state to be destabilized compared to that of HCN as is generally found in other systems, for example, HCHO *vs* CH_3CHO. In the present calculations, however, the resonance position and width for CH_3CN were found to be 3.32 and 0.34 eV, respectively, by the CAP/SAC-CI-NV, that is, E_r was as expected higher, but Γ was against expectations lower. Clearly, methyl substitution can be "stabilizing" in the sense of increasing the lifetime of a π^* resonance.

The difference between NV and V schemes is as small as 0.04 eV for the resonance position and the width is nearly the same (Table 5.4). The uncorrected trajectory is also very clear with the resonance energy and width as 3.37 and 0.37 eV, respectively, by the NV calculations (Supporting Information). These values are compared to the experimental value of the resonance position, 2.84 eV [1]. The SAC and SAC-CI dimensions are 30% and 67% in Lv5 compared to the full calculations (Table 5.1). Considering the accuracy of the resonance position, Lv3-Lv5 gave almost the converged results.

Table 5.4

Resonance position and width (eV) of the ^2E resonance states of CH_3CN. In the projected CAP/SAC-CI calculations a smooth Voronoi potential was used, and corrected resonance energies are reported.

	Level	NV		V	
		E_r	Γ	E_r	Γ
CAP/SAC-CI	Lv3	3.30	0.35	3.26	0.35
	Lv4	3.29	0.35	3.25	0.34
	Lv5	3.30	0.34	3.26	0.34
	Full	3.32	0.34	3.28	0.34
Expt.[a]		2.84			
R-matrix (2015)[b]		2.38	0.39		

[a] Ref. [1]

[b] Ref. [3], Hartree-Fock target state, cc-pVTZ basis, SEP = 2p1h CI

The *R*-matrix method gave the resonance position of 2.38 eV and the width 0.39 eV [3]. The relative stability of the resonance position between HCN and CH_3CN was reproduced by the CAP/SAC-CI calculations: The π^*-resonance state of CH_3CN was calculated to be destabilized by about 0.8 eV (expt. 0.6 eV) with respect to that of HCN, while the *R*-matrix calculations predict a stabilization by 0.35 eV. On the other hand, the

R-matrix calculations were able to predict two higher lying A_1 resonances at ~6.3 and ~9.0 eV [3]. The present CAP calculations are in the first place projected (thirty states were used for CH_3CN) and second have single and double substitutions in the excitation operators. Thus, the method is most suitable for low-lying shape-type resonances that can be described by so-called one-particle configurations. Higher energy states, which will have less one-particle character will be less accurately described.

The results of CH_3NC are listed in Table 5.5 together with those of the *R*-matrix calculations [3]. The ground state of this molecule was located at 1.02 eV above that of CH_3CN. The resonance position and width were calculated as 3.09 and 1.00 eV, respectively, by the CAP/SAC-CI. While neutral CH_3NC is less stable than CH_3NC, the electron attachment energy of CH_3NC is predicted to be lower than that of CH_3CN.

The trends between the resonances of the four molecules, HCN, HNC, CH_3NC, and CH_3NC are not simple, and the author cannot offer a straightforward explanation. While methyl substitution tends to increase resonance positions, and both cyanides and isocyanides do follow this rule, note that there are exceptions even from this rule (e.g. the third resonance of cytosine/methyl-cytosine). Moreover, the trends regarding position and width are exactly reversed upon methyl substitution. The only conserved property after methyl substitution is that the resonance with the somewhat lower position has a considerably larger width, which may seem at first counterintuitive, but there are again many known examples (say, the d-wave π^* resonances of C_2H_4 and N_2 which have positions of 1.8 and 2.3 eV and widths of 0.7 and 0.4 eV). The only thing being clear is that resonances of all four molecules, HCN, HNC, CH_3CN, and CH_3NC, will essentially be dominated by a mixture of p and d-wave scattering, and that difference in the widths may simply indicate somewhat more d-character in the narrower resonances. There is no easy answer as to how exactly this happens, because loosely speaking one would need to know—at the many-body level—how the height and width of the barrier the excess electron is trapped behind is effected by difference between nitriles and isonitriles as well as by hyper-conjugation with the methyl group.

The *R*-matrix calculations give broadly a similar, but in detail a different trend. However, the *R*-matrix calculations are unsuitable for a direct comparison regarding methyl substitution, as the target wavefunction the CI expansions of the anions, and the one particle basis set are not identical. Presently, the CAP/SAC-CI results are the only consistent calculations for all four molecules.

Last, the effect of the perturbation selection of the operators was again small within

0.05 and 0.01 eV for the resonance position and width, respectively. The approximate SAC-CI-V calculation gave a slightly lower resonance position by 0.04 eV, while the resonance widths for both SAC-CI NV and V are almost identical.

Table 5.5
Resonance position and width (eV) of the ^2E resonance states of CH_3NC. In the projected CAP/SAC-CI calculations a smooth Voronoi potential was used, and corrected resonance energies are reported.

	Level	NV		V	
		E_r	Γ	E_r	Γ
CAP/SAC-CI	Lv3	3.04	1.01	3.01	1.00
	Lv4	3.05	1.00	3.01	1.00
	Lv5	3.06	0.99	3.02	0.99
	Full	3.09	1.00	3.05	1.00
R-matrix (2015)[a]		2.70	0.89		

[a] Ref. [3], Hartree-Fock target state, cc-pVTZ basis, SEP = 2p1h CI

5.4.3. Acrylonitrile

Acrylonitrile has a π-conjugation of a C=C double bond and CN group, and should accordingly possess three π* resonance states. In the ETS experiments, four resonance states were observed at 0.11, 2.8, 4.2 and 5.2 eV, and these have been assigned as a″(π*), a′(π*), a″(π*) and σ* (or $\pi^{-1}\pi^{*2}$) states, respectively [1]. In the present CAP/SAC-CI calculations, the three π* resonances will be characterized. The CAP/SAC-CI NV and V results for these resonances are summarized in Table 5.6. The in-plane $^2A'$ state was calculated at 3.17 eV with a width of 0.48 eV, for which the ETS value was reported as 2.8 eV [1]. Although this state was in a sense a high-lying state, because it is dominated by the 23th real SAC-CI state in A′ symmetry, the stabilization of its η-trajectory was clear for both its corrected and its uncorrected trajectory.

The first $^2A''$(π*) state was found at 0.48 eV, and it shows a narrow width of 0.06 eV. This agrees well with the ETS, because this is the only state for which the vibrational structure of the ETS signal could be resolved confirming the low width. The observed vibrational envelope itself stretches from 0.11 eV to at least 0.7 eV, and in contrast to all other experimental values the 0.11 eV reported for this π* state does not refer to a band center but to a band origin easily explaining the unusually high overestimation of almost

126

0.4 eV. The second $^2A''(\pi^*)$ resonance state corresponding to the 4.2 eV signal observed in the ETS was found at 4.29 eV with the broad width of 0.93 eV. As this resonance is exceedingly broad, convergence with respect to perturbation selection of the operators is not smooth for both resonance position and width, but, in particular so for the width. Also the correction for the width is large. It is clear that very broad temporary anion resonances with widths in the order of 1 eV and broader represent a challenge for the present method, and that HCN and the third resonance of acrylonitrile will be interesting benchmark systems for the future.

Table 5.6

Resonance position and width (eV) of the π^* resonance states of acrylonitrile calculated by the projected CAP/SAC-CI with a smooth Voronoi potential. Corrected trajectories were used.

		$^2A''$		$^2A'$		$^2A''$	
		E_r	Γ	E_r	Γ	E_r	Γ
CAP/SAC-CI	Level						
V							
	Lv3	0.38	0.06	3.22	0.63	4.32	0.95
	Lv4	0.39	0.06	3.17	0.56	4.39	0.41
	Lv5	0.42	0.06	3.11	0.48	4.17	0.81
NV							
	Lv3	0.43	0.06	3.26	0.64	–	–
	Lv4	0.44	0.06	3.21	0.56	–	–
	Lv5	0.48	0.06	3.17	0.48	4.29	0.93
Expt. [a]		0.11	–	2.8	–	4.2	–

[a] Ref. [1]

5.4.4. Fumaronitrile

Fumaronitrile (*trans*-NC-CH=CH-CN; c.f. Fig. 1) is one of the simplest molecules, in which two CN groups interact via a C=C double bond. In this molecule, both in-plane (A_g, B_u) and out-of-plane (A_u, B_g) π^* resonances exist: in the ETS, however, one pair of states was observed as almost degenerate at fairly low energy, while at higher energy a second pair could be resolved. The results of the CAP/SAC-CI NV and V calculations in Lv3 accuracy are summarized in Table 5.7. The corresponding unoccupied MOs related to the resonance states are shown in Figure 5.2. Note that one stable bound state

anion (^2B_g state), which results from electron-attachment to an out-of-plane π* MO, exist below the neutral ground state. Its vertical electron affinity was found to be 1.01 eV (SAC-CI). The experimental adiabatic electron affinity was reported as 1.21 eV [60]. For this molecule, the η-trajectories for the ^2A_g resonance in the NV formalism does not show sufficiently clear stabilization behavior, so the author discuss for this state results based on SAC-CI-V calculations.

Resonance states of ^2A_g and ^2B_u symmetry were identified at 2.35 and 2.56 eV, respectively. Experimentally, these states were observed as a single signal at 1.80 eV. These states have similar resonance widths of 0.39 and 0.49 eV and the broad signal observed in ETS can be explained in terms of a combination of the substantial difference of the resonance positions and vibrational broadening. Turning to the higher-energy states, the ^2A_u resonance state was obtained at the resonance position of 4.11 eV with a width of 0.37 eV, while the ^2B_g state was found at 4.16 eV with the large width of 0.94 eV. These positions are so close, that they will clearly show up as a single signal in an ETS. In the actual ETS measurements, two higher states at 3.5 and 5.3 eV were found. In the light of the typical trends of CAP/SAC-CI results for smaller nitriles and many other molecules, it makes sense to assign the first ETS signal to the ^2A_u and ^2B_g resonances, while the second signal could be due to a σ* or Feshbach resonance, similar to the acrylonitrile case. It is noted that the authors of Ref. [1] pointed out that the ETS feature at 5.3 eV is very weak reminiscent of σ* or Feshbach resonances, but assigned it nevertheless to the ^2B_g π* resonance.

Table 5.7
Resonance position and width (eV) of the π* resonance states of fumaronitrile calculated by the projected CAP/SAC-CI with a smooth Voronoi potential. In SAC-CI, Lv3 accuracy was adopted and corrected trajectories were used.

State	Expt.[a]	CAP/SAC-CI			
		NV		V	
		E_r	Γ	E_r	Γ
^2A_g	1.8	2.52	0.88	2.35	0.39
^2B_u	1.8	2.63	0.49	2.56	0.49
^2A_u	3.5	4.21	0.36	4.11	0.37
^2B_g	5.3[b]	4.26	0.95	4.16	0.94

[a] Ref. [1], [b] In the text the author suggests to assign the ^2B_g state to the 3.5 eV feature.

From these results, the ETS structure at 1.8 eV is assigned to an in-plane π*

resonance and the feature at 3.5 eV is due to both out-of-plane π^* resonances. These states are lower than those of acrylonitrile, for which the corresponding resonances are at 2.8 and 4.2 eV and the explanation is simply the extension of π system by another CN group. The very low structure (A″) predicted at ~0.4 eV in acrylonitrile corresponds to the bound B_g state in fumaronitrile.
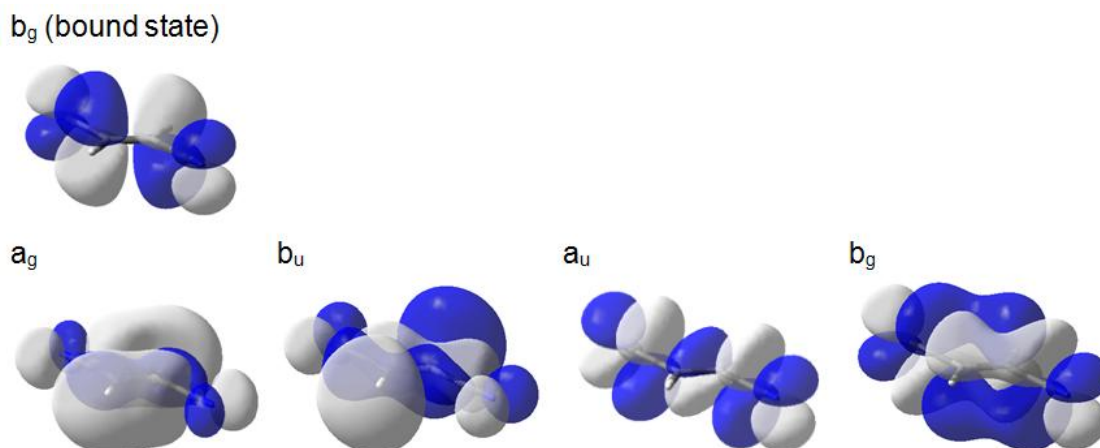
Figure 5.2. Schematic MOs for electron-attachment to fumaronitrile, one bound state and four resonances (isovalue=0.02).

5.4.5. Malononitrile

Finally, the author applied our method to malononitrile ($CH_2(CN)_2$; c.f. Fig. 1), in which two CN groups interact via a methylene group (CH_2). The symmetry of the π^* orbitals is as follows: electron attachment to the in-plane π^* orbitals leads to $^2A_1$ and $^2B_2$ states, while attachment to the out-of-plane π^* orbitals leads to $^2A_2$ and $^2B_1$ (Figure 5.3). In the ETS experiments only two features were observed at 1.50 and 2.55 eV: The $^2A_1$ resonance was attributed to the first ETS signal, while all three, $^2A_2$, $^2B_1$ and $^2B_2$, were attributed to the second feature. Results of the CAP/SAC-CI NV and V calculations in Lv3 accuracy are summarized in Table 5.8. The present results suggest again different assignments from Ref. [1] as shown in Table 5.8; the $^2A_1$ and $^2B_1$ states are found at 2.14 and 2.20 eV, respectively, and can therefore be assigned to the first signal observed at 1.50 eV, while the $^2A_2$ and $^2B_2$ states are assigned to the second position at 2.55 eV. For both pairs of states, $^2A_1$ / $^2B_1$ and $^2A_2$ / $^2B_2$, the energy splitting of the respective resonance positions is very small (0.06-0.07 eV), which would easily explain an overlapping measurement of these state pairs.

Regarding malononitrile as an example for through-bond interaction of π* orbitals, one would compare the out-of-plane and in-plane, in-phase and out-of-phase combinations, respectively. For the out-of-plane resonances, the energy splitting between the in-phase (B_1) and out-of-phase (A_2) combinations is in our calculations ~0.7 eV; for the in-plane resonances the corresponding value is ~0.9 eV (experimentally the two pairs are not resolved, so both values are identical: ~1.0 eV). Since the splittings are so similar, malononitrile seems at best an unconvincing example. Note, however, that this interpretation is very different from the one established in the literature [1] due to our reassignment of the ETS. Last, a brief comment of methodologic issues: again, the difference between the CAP/SAC-CI NV and V resonance position was around 0.05-0.06 eV, while the differences of the resonance width are very small as 0.01 eV.

Table 5.8
Resonance position and width (eV) of the π* resonance states of malononitrile calculated by the projected CAP/SAC-CI with a smooth Voronoi potential. In SAC-CI, Lv3 accuracy was adopted and corrected trajectories were used.

| State	Expt.[a]	CAP/SAC-CI			
		NV		V	
		E_r	Γ	E_r	Γ
$^2A_1$	1.50	2.14	0.31	2.08	0.30
$^2B_1$	2.55[b]	2.20	0.48	2.14	0.48
$^2A_2$	2.55	2.94	0.21	2.88	0.20
$^2B_2$	2.55	3.01	0.69	2.96	0.69

[a] Ref. [1], [b] In the text the author suggests to assign the $^2B_1$ state to the 1.50 eV feature.
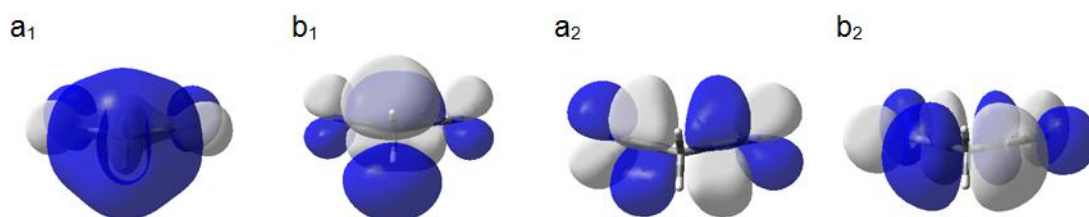
Figure 5.3. MOs for the electron-attachment resonances in malononitile (isovalue=0.02).

5.5. Summary

The author has investigated low-lying π^* resonance states of the following nitriles and isonitriles: HCN, HNC, CH_3CN, CH_3NC, acrylonitrile, fumaronitrile, and malononitrile using the projected CAP/SAC-CI method, where the CAP itself was a smooth Voronoi potential. The cc-pVTZ valence basis set augmented with a [2s5p2d] set of diffuse functions on C and N is used for all calculations. The calculated resonance positions show an excellent correlation with the experimental ETS values (see Fig. 4) and always overestimate the resonance position, most probably due to the anticipated deviations expected from vibrational effects. Exactly the same trend and a similar correlation have been observed before, however, the numbers as such cannot be directly compared with our earlier work, because it was based on a different one-particle basis set. With the triple-ζ set used here, the correlation shown in Fig. 4 reveals that raw computed results (uncorrected for zero-point energies, no Franck-Condon analysis, etc.) should give an overestimate of the observed resonance position of about 0.45 eV. However, the trend equation should be taken with a grain of salt, because in the first place it is based on a fairly small data set, and more importantly, on a data set where several states that have clear energy differences in the computations are assigned to a single ETS feature, and are therefore fit to the same value in the regression analysis. Nevertheless, the trend is sufficiently clear to support a change of assignments for the ETS of fumaronitrile and malononitrile.
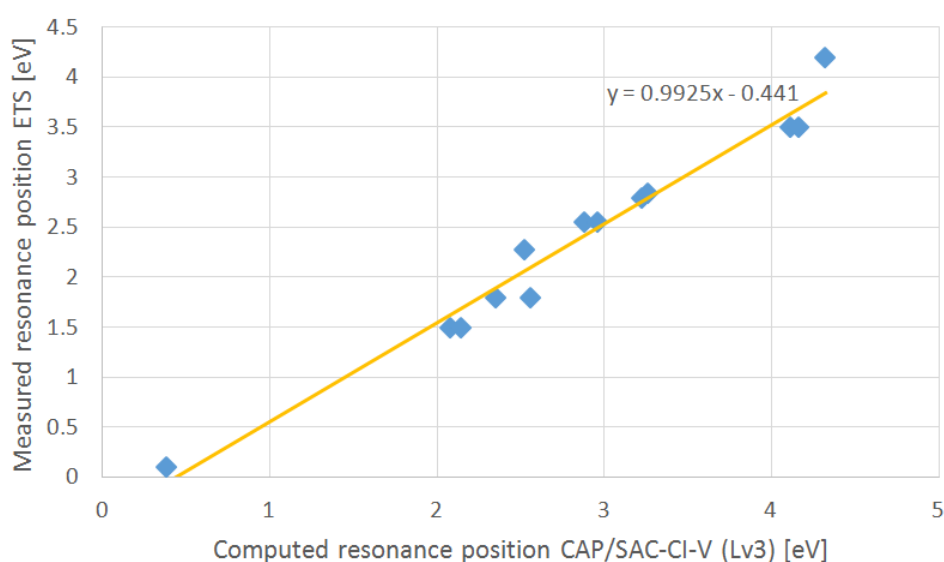
Figure 5.4. Correlation between CAP/SAC-CI calculations and ETS measurements.

On the methodological side two variants of the SAC-CI method, the NV and the approximate V approach were compared for this set of small molecules and the difference of the resonance position between these two schemes is usually very small—less than 0.06 eV. The same is true for the resonance width. The effect of the perturbation selection in approximate SAC-CI calculations was also systematically examined for these resonance states. The dependence on the energy threshold is again of little significant, less than 0.05 eV, though the deviations become larger in the resonance width, for example, more than 0.1 eV in the case of acrylonitrile. Therefore, the calculations with Lv5 accuracy or beyond would be necessary for getting accurate results for resonance widths.

The comparison of the results with the previous electron scattering calculations was also encouraging. For HCN, HNC, CH_3CN, and CH_3NC, the overall trends of the calculated positions and widths agree well with that of recent R-matrix calculations, yet, CAP/SAC-CI and the R-matrix method differ in their predictions regarding trends between nitriles and isonitriles. An extension of the experimental data set to isonitriles would be most welcome.

References

[1]   P. D. Burrow, A. E. Howard, A. R. Johnston, K. D. Jordan, J. Phys. Chem. 96 (1992) 7570-7578.

[2]   H. N. Varambhia, J. Tennyson, J. Phys. B: At. Mol. Opt. Phys. 40 (2007) 1211-1223.

[3]   M. M. Fujimoto, E. V. R. de Lima, J. Tennyson, Eur. Phys. J. D 69 (2015) 153.

[4]   T. Sommerfeld, U. V. Riss, H.-D. Meyer, L. S. Cederbaum, B. Engels, H. U. Suter, J. Phys. B. 31 (1998) 4107-4122.

[5]   F. Mertins, J. Schirmer, Phys. Rev. A 53 (1996) 2140.

[6]   F. Mertins, J. Schirmer, Phys. Rev. A 53 (1996) 2153.

[7]   S. T. Chourou, A. E. Orel, Phys. Rev. A 80 (2009) 032709.

[8]   C. W. McCurdy, V. McKoy, J. Chem. Phys. 61 (1974) 2820-2826.

[9]   R. R. Lucchese, V. KcKoy, Phys. Rev. A 26 (1982) 1992-1996.

[10]   J. Tennyson, C. J. Noble, J. Phys. B: At. Mol. Opt. Phys. 19 (1986) 4025-4033.

[11]   U. V. Riss, H.-D. Meyer, J. Phys. B 26 (1993) 4503-4536.

[12]   R. Santra, L. S. Cederbaum, Phys. Reports 368 (2002) 1-117.

[13]   T. Sommerfeld, R. J. Weber, J. Phys. Chem. A 115 (2011) 6675-6682.

[14]   J. Horacek, P. Mach, J. Urban, Phys. Rev. A 82 (2010) 032713.

[15] J. Horacek, I. Paidarova, R. Curik, J. Chem. Phys. 143 (2015) 184102.

[16] C. W. McCurdy, R. N. Rescigno, Phys. Rev. Lett. 41 (1978) 1364-1368.

[17] A. F. White, M. Head-Gordon, C. W. McCurdy, J. Chem. Phys. 142 (2015) 054103.

[18] A. F. White, C. W. McCurdy, M. Head-Gordon, J. Chem. Phys. 143 (2015) 074103.

[19] J. S.-Y. Chao, M. F. Falcetta, K. D. Jordan, J. Chem. Phys. 93 (1990) 1125-1135.

[20] T. Sommerfeld, F. Tarantelli, H.-D. Meyer, L. S. Cederbaum, J. Chem. Phys. 112 (2000) 6635-6642.

[21] T. Sommerfeld, Phys. Rev. Lett. 85 (2000) 956-959.

[22] T. Sommerfeld, R. Santra, Intern. J. Quantum Chem. 82 (2001) 218-226.

[23] R. Santra, L. S. Cederbaum, J. Chem. Phys. 117 (2002) 5511-5521.

[24] S. Feuerbacher, T. Sommerfeld, R. Santra, L. S. Cederbaum, J. Chem. Phys. 118 (2003) 6188-6199.

[25] M. Ehara, T. Sommerfeld, Chem. Phys. Lett. 537 (2012) 107-112.

[26] M. Ehara, R. Fukuda, T. Sommerfeld, J. Comput. Chem. 37 (2016) 242-249.

[27] A. Ghosh, N. Vaval, S. Pal, J. Chem. Phys. 136 (2012) 234110.

[28] A. Ghosh, A. Karne, S. Pal, Phys. Chem. Chem. Phys. 15 (2013) 17915-17921.

[29] T. C. Jagau, D. Zuev, K. B. Bravaya, E. Epifanovsky, A. I. Krylov, J. Phys. Chem. Lett. 5 (2014) 310-315.

[30] D. Zuev, T. C. Jagau, K. B. Bravaya, E. Epifanovsky, Y. H. Shao, E. Sundstrom, M. Head-Gordon, A. I. Krylov, J. Chem. Phys. 141 (2014) 024102.

[31] Y. Sajeev, S. Pal, Mol. Phys. 103 (2005) 2267-2275.

[32] Y. Sajeev, R. Santra, S. Pal, J. Chem. Phys. 122 (2005) 234320.

[33] T. C. Jagau, A. I. Krylov, J. Phys. Chem. Lett. 5 (2014) 3078-3085.

[34] Y. Kanazawa, M. Ehara, T. Sommerfeld, J. Phys. Chem. A 120 (2016) 1545-1553.

[35] T. C. Jagau, A. I. Krylov, J. Chem. Phys. 144 (2016) 054113.

[36] Y. Sajeev, A. Ghosh, N. Vaval, S. Pal, Int. Rev. Phys. Chem. 33 (2014) 397-425.

[37] H. Nakatsuji, Chem. Phys. Lett. 59 (1978) 362-364.

[38] H. Nakatsuji, Chem. Phys. Lett. 67 (1979) 329-333.

[39] T. Sommerfeld, M. Ehara, J. Chem. Phys. 142 (2015) 034105.

[40] T. Sommerfeld, M. Ehara, J. Chem. Theory Comput. 11 (2015) 4627-4633.

[41] C. Winstead, V. McKoy, J. Chem. Phys. 125 (2006) 174304.

[42] A. Dora, J. Tennyson, L. Bryjko, T. van Mourik, J. Chem. Phys. 130 (2009) 164307.

[43] Z. Mašin, J. D. Gorfinkiel, J. Chem. Phys. 135 (2011) 144308.

[44] G. Gamow, Z. Phys. 51 (1928) 204.

[45] A. J. F. Siegert, Phys. Rev. 56 (1939) 750.

[46] R. Santra, L. S. Cederbaum, H.-D. Meyer, Chem. Phys. Lett. 303 (1999) 413-419.

[47] K. Hirao, J. Chem. Phys. 79 (1983) 5000-5010.

[48] H. Nakatsuji, M. Ehara, J. Chem. Phys. 101 (1994) 7658-7671.

[49] P. Krause, J. A. Sonk, H. B. Schlegel, J. Chem. Phys. 140 (2014) 174113.

[50] P. Krause, H. B. Schlegel, J. Phys. Chem. A 119 (2015) 10212-10220.

[51] T. H. Dunning, Jr, J. Chem. Phys. 90 (1989) 1007-1023.

[52] A. D. Becke, J. Chem. Phys. 98 (1993) 5648−5652.

[53] R. Fukuda, H. Nakatsuji, J. Chem. Phys. 128 (2008) 094105.

[54] R. Fukuda, M. Ehara, J. Comput. Chem. 35 (2014) 2163-2176.

[55] H. Nakatsuji, Chem. Phys. 75 (1983) 425-441.

[56] M. J. Frisch, G. W. Trucks, H. B. Schlegel, G. E. Scuseria, M. A. Robb, J. R. Cheeseman, G. Scalmani, V. Barone, B. Mennucci, G. A. Petersson, H. Nakatsuji, M. Caricato, X. Li, H. P. Hratchian, A. F. Izmaylov, J. Bloino, G. Zheng, J. L. Sonnenberg, M. Hada, M. Ehara, K. Toyota, R. Fukuda, J. Hasegawa, M. Ishida, T. Nakajima, Y. Honda, O. Kitao, H. Nakai, T. Vreven, J. A. Montgomery, Jr., J. E. Peralta, F. Ogliaro, M. Bearpark, J. J. Heyd, E. Brothers, K. N. Kudin, V. N. Staroverov, T. Keith, R. Kobayashi, J. Normand, K. Raghavachari, A. Rendell, J. C. Burant, S. S. Iyengar, J. Tomasi, M. Cossi, N. Rega, J. M. Millam, M. Klene, J. E. Knox, J. B. Cross, V. Bakken, C. Adamo, J. Jaramillo, R. Gomperts, R. E. Stratmann, O. Yazyev, A. J. Austin, R. Cammi, C. Pomelli, J. W. Ochterski, R. L. Martin, K. Morokuma, V. G. Zakrzewski, G. A. Voth, P. Salvador, J. J. Dannenberg, S. Dapprich, A. D. Daniels, O. Farkas, J. B. Foresman, J. V. Ortiz, J. Cioslowski, D. J. Fox, GAUSSIAN09 Rev. B.01., Gaussian Inc., Wallingford CT, 2010.

[57] A. Jain, D. W. Norcross, Phys. Rev. A 32 (1985) 134-143.

[58] A. Jain, D. W. Norcross, J. Chem. Phys. 84 (1986) 739-744.

[59] T. van Mourik, G. J. Harris, O. L. Polyansky, J. Tennyson, A. G. Csaszar, P. J. Kowles, J. Chem. Phys. 115 (2001) 3706-18.

[60] D. Khuseynov, A. R. Dixon, D. J. Dokuchitz, A. Sanov, J. Phys. Chem. A 118 (2014) 4510-4518.

HCN
AO: cc-pVTZ + diffuse [2s5p2d] with scaling factor 1.5 (5p) and 2.0 (2s,2d)
SAC-CI: $(A_1, A_2, B_1, B_2) = (0, 0, 10, 0)$

Table 5.S1. Resonance position and width (eV) of the π^* resonance states of HCN calculated by the projected CAP/SAC-CI with smooth Voronoi potential. Corrected and uncorrected trajectories were used.

Level	Expt.[a]	CAP/SAC-CI			
		corrected		uncorrected	
		E_r	Γ	E_r	Γ
V Lv3	2.28	2.52	1.12	2.31	1.35
V Lv4		2.51	1.14	2.31	1.35
V Lv5		2.52	1.16	2.32	1.36
V Full		2.52	1.15	2.32	1.37
NV Lv3	2.28	2.51	1.10	2.35	1.37
NV Lv4		2.51	1.09	2.35	1.36
NV Lv5		2.52	1.10	2.35	1.36
NV Full		2.53	1.09	2.36	1.37

[a] Ref. [1]

Table. SAC/SAC-CI dimensions for HCN with cc-pVTZ+[2s5p2d]

Level	SAC	SAC-CI
Lv3	19357	12204
Lv4	23338	13710
Lv5	31532	16125
Full	49688	18331

HNC
AO: cc-pVTZ + diffuse [2s5p2d] with scaling factor 1.5 (5p) and 2.0 (2s,2d)
SAC-CI: $(A_1, A_2, B_1, B_2) = (0, 0, 10, 0)$

Table 5.S2. Resonance position and width (eV) of the π^* resonance states of HCN calculated by the projected CAP/SAC-CI with smooth Voronoi potential. Corrected and uncorrected trajectories were used.

Level	CAP/SAC-CI			
	corrected		uncorrected	
	E_r	Γ	E_r	Γ
V Lv3	2.72	0.51	2.79	0.61
V Lv4	2.72	0.51	2.79	0.62
V Lv5	2.73	0.51	2.80	0.62
V full	2.74	0.51	2.81	0.62
NV Lv3	2.76	0.51	2.83	0.62
NV Lv4	2.74	0.53	2.82	0.62
NV Lv5	2.75	0.52	2.83	0.62
NV full	2.77	0.51	2.84	0.62

Table. SAC/SAC-CI dimensions for HNC with cc-pVTZ+[2s5p2d]

Level	SAC	SAC-CI
Lv3	19698	12291
Lv4	23916	13786
Lv5	32195	16149
Full	49689	18331

CH₃CN
AO: cc-pVTZ + [2s5p2d] with scaling factor 1.5 (5p) and 2.0 (2s,2d)
SAC-CI: (A′, A″)=(0, 15)

Table 5.S3. Resonance position and width (eV) of the π^* resonance states of CH₃CN calculated by the projected CAP/SAC-CI with smooth Voronoi potential. Corrected and uncorrected trajectories were used.

Level	Expt.[a]	CAP/SAC-CI			
		corrected		uncorrected	
		E_r	Γ	E_r	Γ
V Lv3	2.84	3.26	0.35	3.30	0.39
V Lv4		3.25	0.34	3.30	0.38
V Lv5		3.26	0.34	3.30	0.37
V Full		3.28	0.34	3.32	0.37
NV Lv3	2.84	3.30	0.35	3.34	0.39
NV Lv4		3.29	0.35	3.34	0.39
NV Lv5		3.30	0.34	3.34	0.38
NV Full		3.32	0.34	3.37	0.37

[a] Ref. [1]

Table. SAC/SAC-CI dimensions for CH₃CN with cc-pVTZ+[2s5p2d]

Level	SAC	SAC-CI
Lv3	66908	54812
Lv4	98562	69595
Lv5	195330	104279
Full	660235	155627

CH₃NC
AO: cc-pVTZ + [2s5p2d] with scaling factor 1.5 (5p) and 2.0 (2s,2d)
SAC-CI: (A′, A′′)= (0, 15)

Table 5.S4. Resonance position and width (eV) of the π^* resonance states of CH₃NC calculated by the projected CAP/SAC-CI with smooth Voronoi potential. Corrected and uncorrected trajectories were used.

Level	CAP/SAC-CI			
	corrected		uncorrected	
	E_r	Γ	E_r	Γ
V Lv3	3.01	1.00	3.25	1.28
V Lv4	3.01	1.00	3.25	1.26
V Lv5	3.02	0.99	3.26	1.24
V full	3.05	1.00	3.29	1.25
NV Lv3	3.04	1.01	3.29	1.28
NV Lv4	3.05	1.00	3.29	1.27
NV Lv5	3.06	0.99	3.30	1.25
NV full	3.09	1.00	3.34	1.25

Table. SAC/SAC-CI dimensions for CH₃NC with cc-pVTZ+[2s5p2d]

Level	SAC	SAC-CI
Lv3	69529	54091
Lv4	104776	69782
Lv5	213199	106906
Full	653373	154241

Acrylonitrile, CH$_2$=CHCN
AO: cc-pVTZ + [2s5p2d] with scaling factor 1.5 (5p) and 2.0 (2s,2d)
SAC-CI: (A′, A″)= (25,20)

Table 5.S5. Resonance position and width (eV) of the π* resonance states of acrylonitrile calculated by the projected CAP/SAC-CI with smooth Voronoi potential. Corrected and uncorrected trajectories were used.

Level	Expt.[a]	CAP/SAC-CI			
		corrected		uncorrected	
		E_r	Γ	E_r	Γ
A′					
V Lv3	2.80	3.22	0.63	3.14	0.81
V Lv4		3.17	0.56	3.11	0.72
V Lv5		3.11	0.48	3.07	0.61
NV Lv3	2.80	3.26	0.64	3.17	0.82
NV Lv4		3.21	0.56	3.15	0.73
NV Lv5		3.17	0.48	3.12	0.62
A″					
V Lv3	0.11	0.38	0.06	0.40	0.07
V Lv4		0.39	0.06	0.40	0.07
V Lv5		0.42	0.06	0.43	0.07
NV Lv3	0.11	0.43	0.06	0.44	0.07
NV Lv4		0.44	0.06	0.45	0.07
NV Lv5		0.48	0.06	0.49	0.07
A″					
V Lv3	4.2	4.32	0.95	4.40	1.54
V Lv4		4.39	0.41	4.41	1.21
V Lv5		4.17	0.81	4.31	1.36
NV Lv3	4.2	NA	NA	4.64	1.67
NV Lv4		NA	NA	4.44	1.25
NV Lv5		4.29	0.93	4.50	1.25

[a] Ref. [1]

Table. SAC/SAC-CI dimensions for acrylonitrile with cc-pVTZ+[2s5p2d]

Level	SAC	SAC-CI	
		A′	A″
Lv3	126679	66454	109272
Lv4	214976	96013	141407
Lv5	523521	181300	213385
Full	1676202	342920	302494

Fumaronitrile, *trans*-NC-CH=CH-CN
AO: cc-pVTZ + [2s5p2d] with scaling factor 1.5 (5p) and 2.0 (2s,2d)
SAC-CI: LevelThree (A_g, B_g, A_u, B_u)=(20, 14, 20, 20)

Table 5.S6. Resonance position and width (eV) of the π^* resonance states of fumaronitrile calculated by the projected CAP/SAC-CI with smooth Voronoi potential. Corrected and uncorrected trajectories were used.

State	Expt.[a]	CAP/SAC-CI			
		corrected		uncorrected	
		E_r	Γ	E_r	Γ
NV					
A_g	1.8	2.52	0.88	2.63	2.01
B_u	1.8	2.63	0.49	2.62	0.63
A_u	3.5	4.21	0.36	4.17	0.44
B_g	3.5[b]	4.26	0.95	4.13	1.48
V					
A_g	1.8	2.35	0.39	2.38	0.49
B_u	1.8	2.56	0.49	2.56	0.62
A_u	3.5	4.11	0.37	4.07	0.43
B_g	3.5[b]	4.16	0.94	4.11	1.38

[a] Ref. [1], [b] In the text we suggest to assign the ^2B_g state to the 3.5 eV feature.

b$_g$ (bound state)

a$_g$ b$_u$ a$_u$ b$_g$
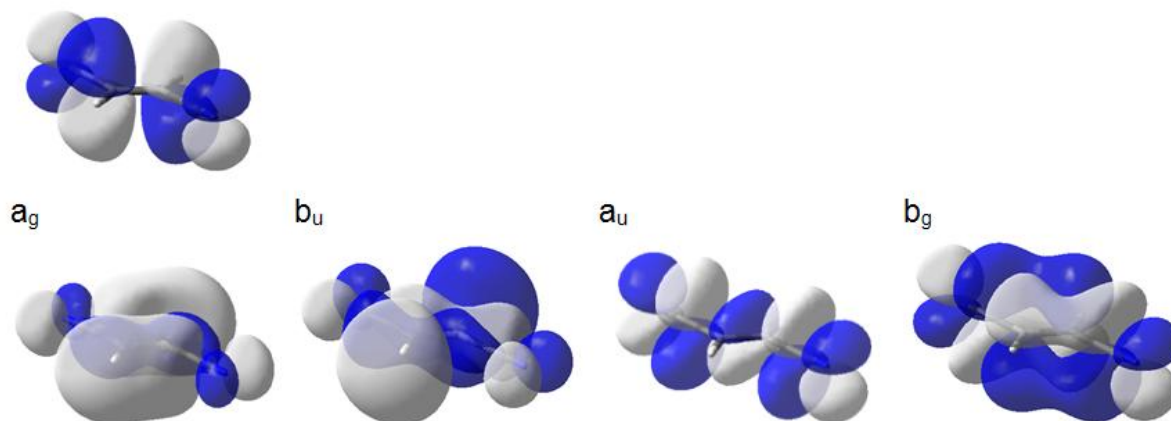
Figure. Schematic MOs for electron-attachment to fumaronitrile, one bound state and four resonances (isovalue=0.02)

Malononitrile, CH$_2$(CN)$_2$
AO: cc-pVTZ + [2s5p2d] with scaling factor 1.5 (5p) and 2.0 (2s,2d)
SAC-CI: LevelThree (20, 10, 15, 20)

Table 5.S7. Resonance position and width (eV) of the π* resonance states of malononitrile calculated by the projected CAP/SAC-CI with smooth Voronoi potential. Corrected and uncorrected trajectories were used.

State	Expt.[a]	CAP/SAC-CI			
		corrected		uncorrected	
		E_r	Γ	E_r	Γ
NV					
A$_1$	1.50	2.14	0.31	2.16	0.29
B$_1$	2.55[b]	2.20	0.48	2.22	0.55
A$_2$	2.55	2.94	0.21	2.96	0.29
B$_2$	2.55	3.01	0.69	2.95	0.85
V					
A$_1$	1.50	2.08	0.30	2.10	0.29
B$_1$	2.55[b]	2.14	0.48	2.16	0.55
A$_2$	2.55	2.88	0.20	2.90	0.28
B$_2$	2.55	2.96	0.69	2.89	0.85

[a] Ref. [1], [b] In the text we suggest to assign the ^{2}B$_1$ state to the 1.50 eV feature.
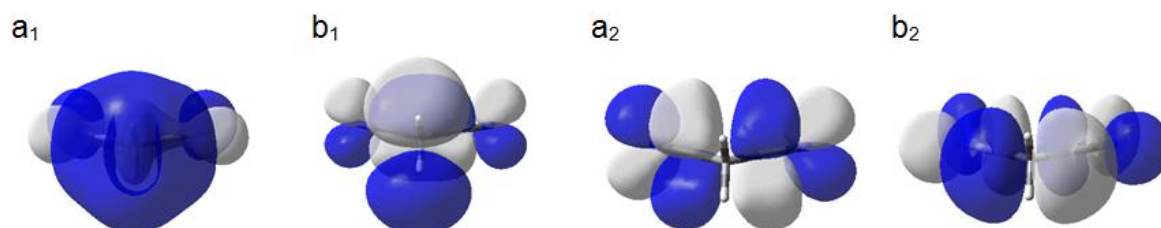
Figure. MOs for the electron-attachment resonances in malononitrile (isovalue=0.02)

η-trajectory

HCN

HNC
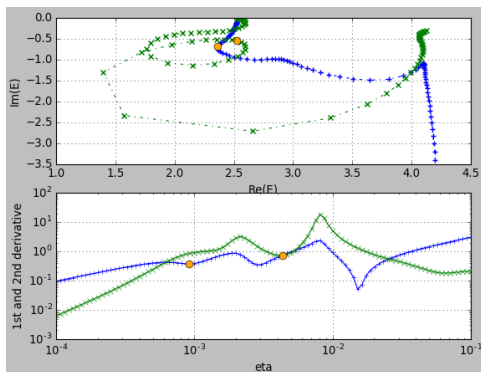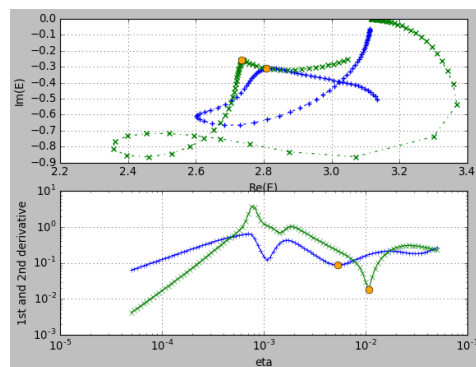
CH₃CN
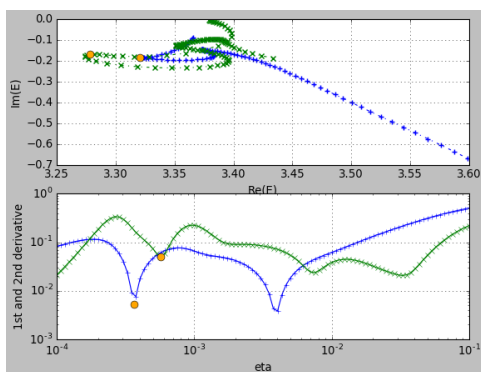
CH₃NC
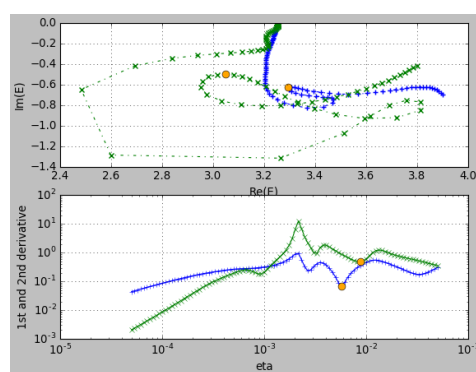
Acrylonitrile

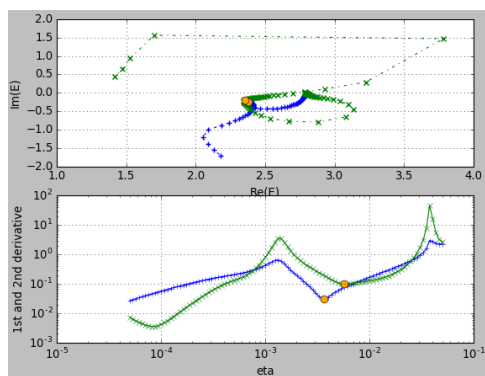### A′
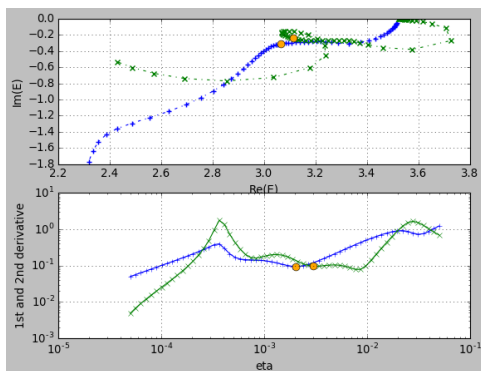
A″
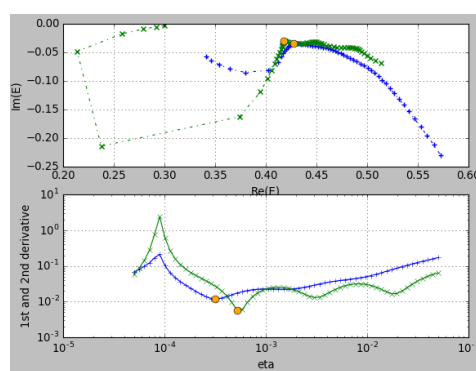
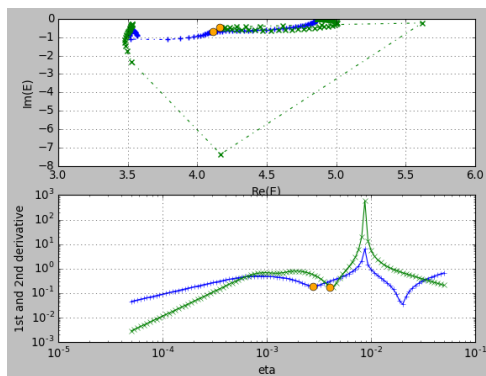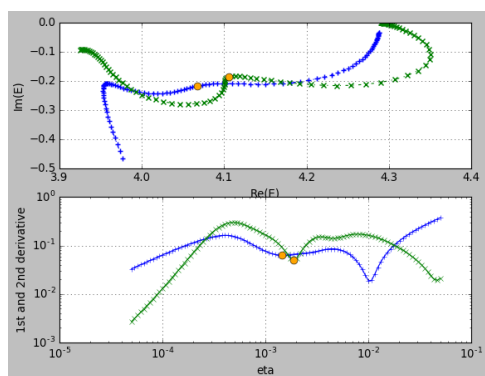### A″
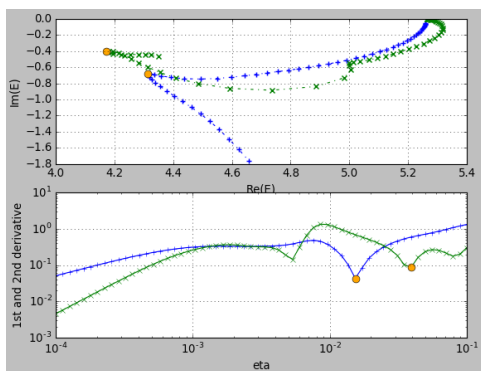
Fumaronitrile

A_g

B_g

A_u

B_u
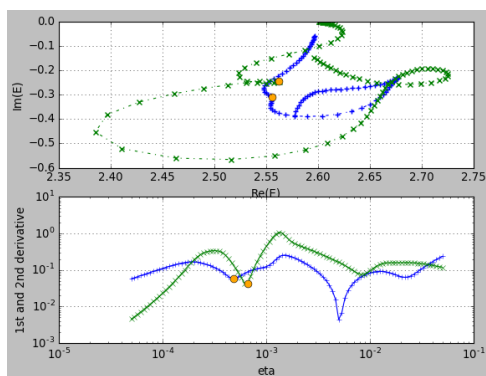
Malononitrile

A_1

A_2

B_1

B_2
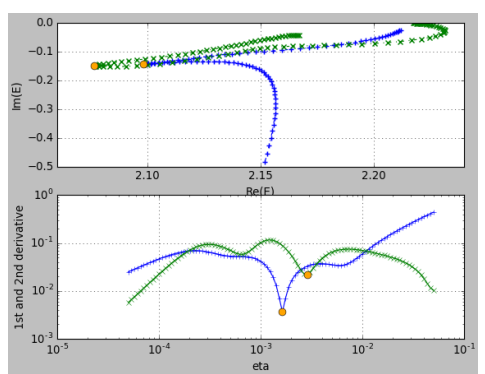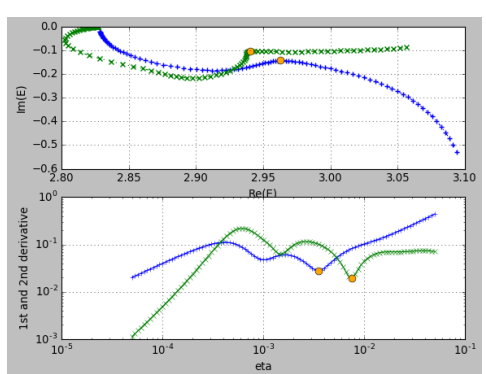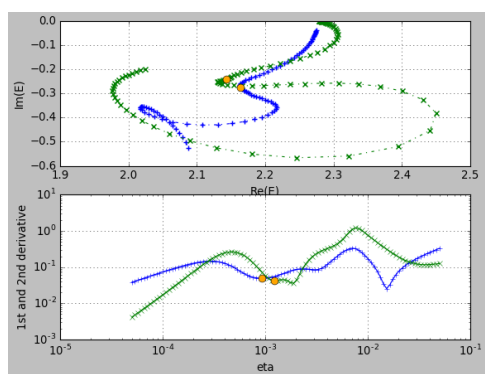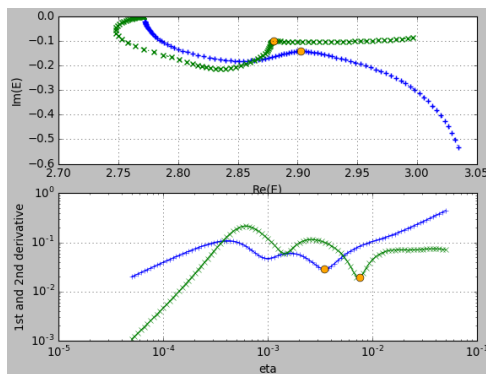

142

Chapter 6

General Conclusion

Recently, in the field of physical chemistry and functional molecular science, fundamental researches focusing on the photoelectronic processes and electron transfers of molecular systems with complicated geometrical and electronic structures have been performed. In these researches, the theoretical analysis on the geometries and electronic structures plays an important role where the theories and computational methodologies that describe the complicated electronic structures in high accuracy and efficiency are required. For example, it is not so straightforward to describe the electronic states whose σ-electrons delocalized over entire molecular systems and the quasi-stable states that decay electronically to more stable states. In this thesis, the author mainly worked on two research subjects focusing on these electronic states. More precisely, the author worked on the theoretical analysis of the characteristic photophysical properties of *n*-peralkylated oligosilanes due to σ-conjugation and the electronic resonance states of DNA and RNA nucleobases.

In chapter 1, the author briefly described the introduction of the structure dependence of the photophysical properties of silicon compounds and the electronic resonance states of DNA and RNA bases. The author also briefly explained the electronic structure theories adopted in this thesis.

In chapter 2, the theoretical study on the photophysical properties of *n*-peralkylated hexasilane was summarized. *n*-Peralkylated silicon compounds show characteristic photophysical properties because of their σ-electron delocalization. Their photophysical properties depend on the Si chain length and its conformation. Previously, theoretical analysis on tetrasilane which has minimum unit of structural isomer has been performed. In this work, the author investigated the photophysical properties of *n*-peralkylated hexasilane which has three SiSiSiSi dihedral angles. In experiment, three conformationally controlled *n*-peralkylated hexasilanes were synthesized and their photophysical properties of these compounds were analyzed by the UV-Vis, MCD and LD spectroscopies. Based on the X-ray structural analysis, some of the local-minimum structures of these *n*-peralkylated hexasilanes and the relationship between the conformation and electronic excited states were investigated. Also, the variation of the orbital energies and oscillator strengths along the three dihedral angles were analyzed and the relationship between the conformation and electronic excited states was clarified. In the variation of specific dihedral angle, avoided crossing occurs between the σσ* and σπ* states and the excitation energy to the electronic state which show

strong absorption drastically change and the shape of the absorption peak drastically change.
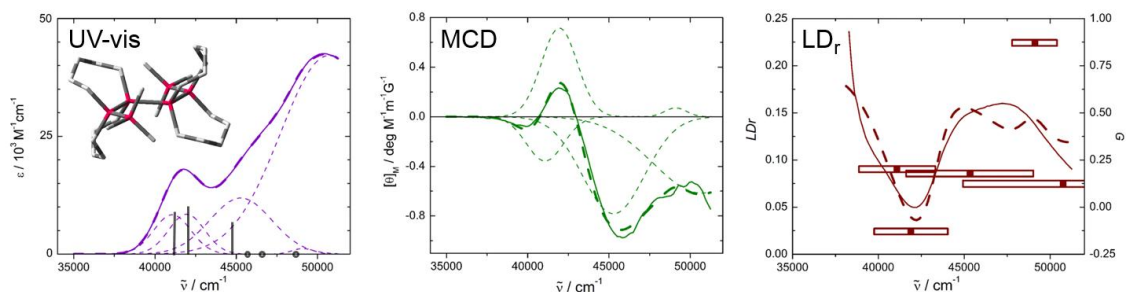
Figure 6.1. Conformationally controlled peralkylated hexasilanes and their absorption spectra.

In chapter 3, the structure relaxation in the excited state and the photoemission properties of the *n*-peralkylated oligosilanes, $Me(SiMe_2)_nMe$, (n=4-8) have been investigated. Characteristic difference of the emission spectra was observed depending on the Si chain length. When the Si chain length is relatively long (n=7, 8), sharp emission peak with small Stokes shift was observed while the broad peaks with large Stokes shift was measured for the oligosilanes with short Si chain (n=4-6); comparison is made in Figure 6.2. Focusing on these points, the author studied the geometries in the excited state of *n*-peralkylated oligosilanes of $Me(SiMe_2)_nMe$, (n=4-8) and absorption and emission spectra by using the DFT calculations and analyzed the relationship between the emission spectra and the Si chain length. In the case of *n*-peralkylated oligosilanes with short Si chain (n=4-6), the excitation is relatively localized, namely, one Si-Si bond is elongated by more than 0.2 Å with other Si-Si bonds unchanged so much. On the other hand, in the case of oligosilanes with long Si chain (n=7, 8), several Si-Si bonds are elongated by 0.06 Å and the excitation is delocalized over the entire molecule. Because of the different nature of the excited state, different emission spectra are observed. Furthermore, the bridged peralkylated pentasilane whose structure is restricted so that the Si-Si bond lengths and dihedral angle do not change was synthesized. The calculated emission spectra of this structure restricted pentasilane showed small Stokes shift, which reproduced the experimental results. These results clarified the origin of the relationship between the excited structure relaxation and emission spectra depending on the Si chain length. The present physical insight

145

regarding the excited state structure relaxation provided important guideline to control the photophysical properties of n-peralkylated oligosilanes.
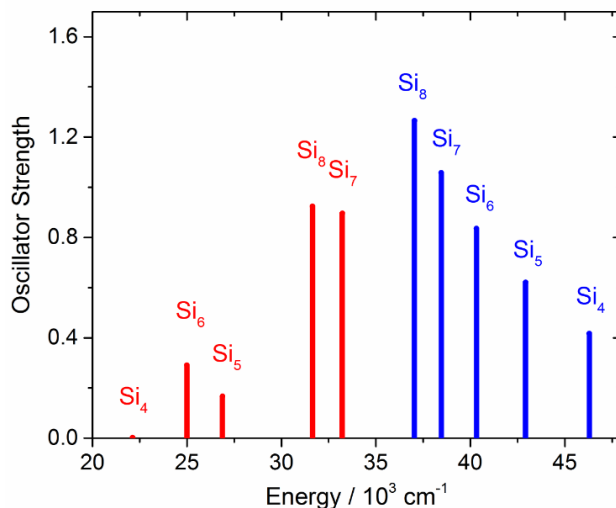
Figure 6.2. Calculated absorption peak (blue) and emission peak (red) of n-Si$_n$Me$_{2n+2}$ (n=4-8)

In chapter 4, the author worked on the theoretical analysis of the electronic resonance states of the DNA and RNA nucleobases. Among several physical processes that have been proposed for the origin of DNA damage, low-energy electron attachment has been considered. In the molecular spectroscopy, it was found that electron attachment induces the decomposition of the DNA and RNA nucleobases. The initial stage of this process is recognized as the resonance state generated by electron attachment, however, the theoretical analysis of the energy level and lifetime of the resonance states has been still difficult. In this work, complex absorbing potential (CAP) method that is combined with the accurate electron correlation method, symmetry-adapted-cluster configuration interaction (SAC-CI) method was utilized to calculate the resonance states of nucleobases and their derivatives. Generally, the box potential has been used for the CAP. Although this potential is useful in the applications to diatomic molecules and linear molecules, it is not suitable for molecules or molecular clusters with complex molecular/cluster shape like nucleobases. There is also a significant parameter dependence in this potential. For solving this problem, new potential, namely, Voronoi surface at each atom with the overlap region smoothed was introduced. Using this smooth Voronoi potential, the CAP method can be applied to the molecular systems or clusters with complex structure and the resonance energy and

width can be calculated in a stable manner. In this work, the author investigated the π^* resonance states of DNA and RNA nucleobases by using the CAP/SAC-CI method with smooth Voronoi potential. The author succeeded to calculate not only the lowest state, but also three to four resonance states of nucleobases and their derivatives and the calculated values showed good agreement with the experimental values observed by electron transmission spectroscopy as shown in Figure 6.3. In particular, the CAP/SAC-CI method provided very accurate values for the third resonance states compared with those by experiment and other methodologies previously reported. Furthermore, the author succeeded to calculate the fourth resonance states of guanine and adenine for the first time. Based on these calculations, the author demonstrated that the present method is useful to investigate the electronic resonance states of medium-size molecules.
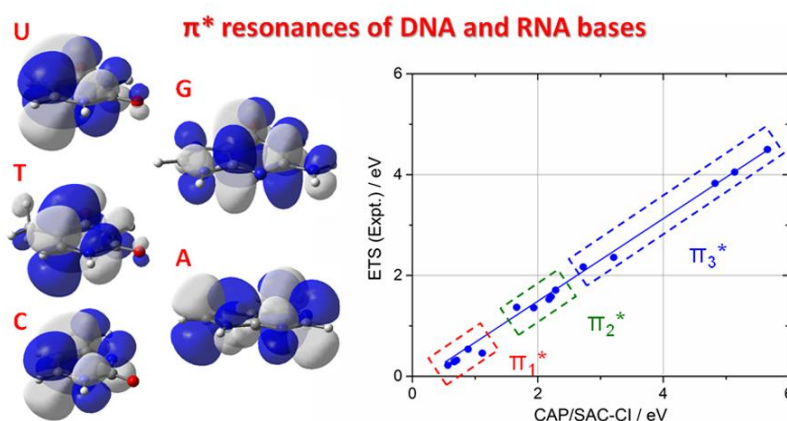
Figure 6.3. Comparison of the resonance energy calculated by CAP/SAC-CI method with experimental values.

In chapter 5, the author performed benchmark calculations of the CAP/SAC-CI method with respect to the resonance states of molecules with nitryl or isonitryl group(s). The accuracy of the CAP/SAC-CI method and the generality were systematically examined with respect to the computational conditions like energy threshold of perturbation selection of operators, variational/non-variational approach, and basis sets etc. For HCN and HNC, theoretical studies using electron-scattering methods and experimental works using electron transmission spectroscopy have been

reported. In this work, the author demonstrated that the CAP/SAC-CI method gave accurate results for both resonance energy and width. The author also showed that two cyano groups interact with each other in-plane and out-of-plane ortibals and generates resonance states as shown in Figure 6.4.
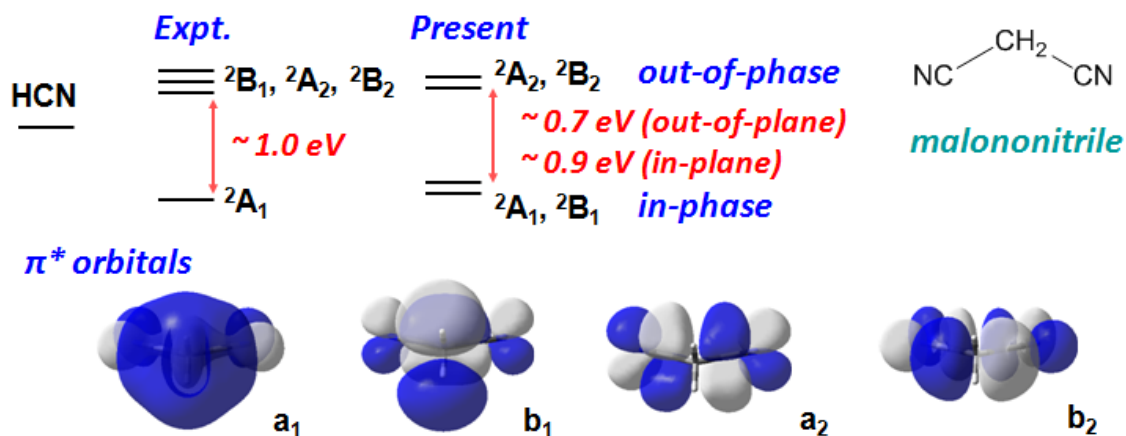
Figure 6.4. Interaction of the resonances of two cyano groups.

In this thesis, the author worked on the complex electronic states for two research subjects: one is the photophysical properties of peralkylated oligosilanes which has σ-delocalization and the other is the electronic resonance states of DNA and RNA nucleobases. The obtained new physical insight will be useful for the further fundamental physical chemistry related to these research subjects.

List of publications

Chapter 2

1. <u>**Yuki Kanazawa**</u>, Hayato Tsuji, Masahiro Ehara, Ryoichi Fukuda, Deborah L. Casher, Kohei Tamao, Hiroshi Nakatsuji, Josef Michl,

"Electronic Transitions in Conformationally Controlled Peralkylated Hexasilanes",

ChemPhysChem, 19, pp3010–3022, 2016.

Chapter 4

2. <u>**Yuki Kanazawa**</u>, Masahiro Ehara, Thomas Sommerfeld,

"Low-Lying π^* Resonances of Standard and Rare DNA and RNA Bases Studied by the Projected CAP/SAC–CI Method",

J. Phys. Chem. A, 120 (9), pp1545–1553, 2016.

Chapter 5

3. Masahiro Ehara, <u>**Yuki Kanazawa**</u>, Thomas Sommerfeld,

"Low-Lying π^* resonances associated with cyano groups: A CAP/SAC-CI study",

Chem. Phys., 482, pp169–177, 2017.

Acknowledgements

In this part, I would like to express my gratitude. The present study has not been achieved only by my competence, but through efforts made by many people.

First of all, I would like to thank Prof. Masahiro Ehara for achieving these studies summarized here. He kindly taught me how to proceed the works in this thesis. I would like to be grateful to all colleagues in Research Center for Computational Science.

Second, in each study, I would like to thank my collaborators. In the work of the excited states of peralkylated hexasilanes, I would like to thank Prof. H. Tsuji, Prof. R. Fukuda, Dr. D. L. Casher, Prof. K. Tamao, Prof. H. Nakatsuji, and Prof. J. Michl for excellent collaboration. In the study of resonance states, I am deeply grateful to Prof. T. Sommerfeld for the CAP methods. Furthermore, I am grateful to the Research Center for Computational Science in Okazaki, Japan. The calculations were performed by using this institution.

At last, financial support from the Institute for Molecular Science is gratefully acknowledged. Because I had this support, I have been able to concentrate on my study.